Contribution to the concept of micro factory : design of a flexible electromagnetic conveyor system

Neha Arora

Par **Neha ARORA**

Contribution to the concept of micro factory: design of a flexible electromagnetic conveyor system

Thèse présentée
pour l'obtention du grade
de Docteur de l'UTC

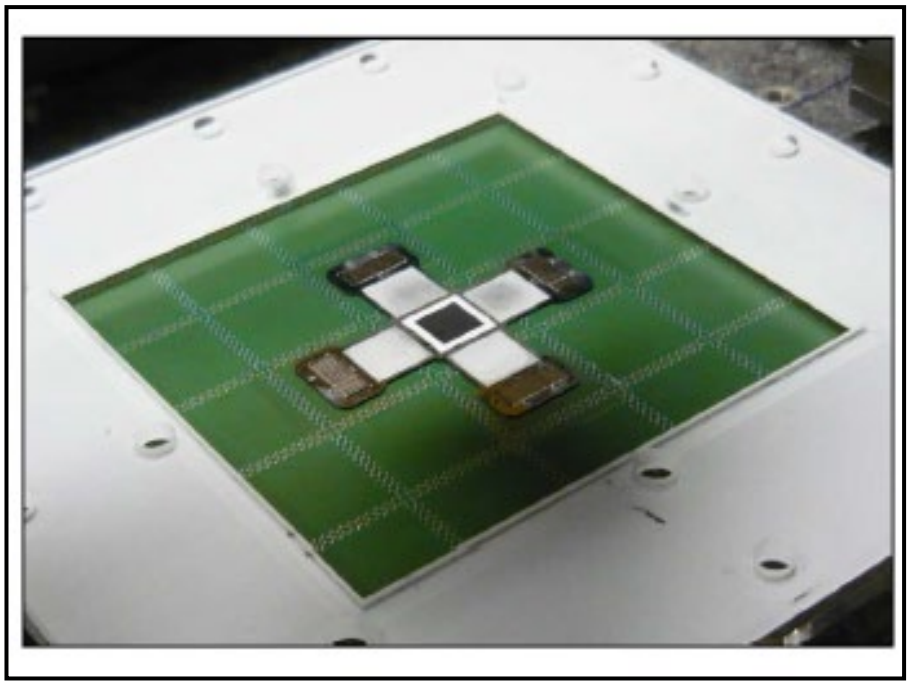

Soutenue le 30 mars 2017
Spécialité : Mécatronique, Photonique et Systèmes : Unité de recherche en Mécanique - Laboratoire Roberval (FRE UTC - CNRS 2012)
D2347

Contribution to the concept of micro factory: design of a flexible electromagnetic conveyor system

Thesis presented to obtain the grade of Doctor from the
Université de Technologie de Compiègne, France

From the faculty of Mechanical Engineering department of the Université de Technologie de Compiègne in Compiègne, France

Spécialité : Mécatronique, Photonique et Systèmes

Dissertation written by

Neha Arora

Defended on 30 March 2017

Jury Members :

Dr. Adrien Badel	Reviewer	Laboratoire SYMME, Annecy le vieux
Dr. Michaël Gauthier	Reviewer	Laboratoire FEMTO-ST, Besançon
Prof. Dr. Stephan Regnier	President	Laboratoire ISIR, Paris
Prof. Dr. Vincent Lafranchi	Examiner	Laboratoire LEC, UTC
Prof. Dr. Christine Prelle	PhD director	Laboratoire Roberval, UTC
Dr. Laurent Petit	PhD director	Laboratoire Roberval, UTC

TABLE OF CONTENTS

Acknowledgement

The study was conducted in the Roberval Laboratory, UMR 7337, UTC/CNRS, Université de Technologie de Compiègne (UTC), under the direction of Ms. Christine Prelle, Professor and Mr. Laurent Petit, Associate professor in the department of advanced mechnics (Génie des Système Mécanique) at UTC. I owe particular thanks to both the directors of my thesis for all their advice, support and confidence they have shown till the end. Without their guidance and persistent help on both professional and personal levels, this dissertation would not have been possible.

I would like to extend my thanks to Prof. Dr. Frédéric Lamarque, M. Muneeb Ullah Khan, M. Phillip Pouille, M. Erwan Dupont, M. Jeremy Terrien and all the staff members for their contribution and support in various discussions. I would like to thank all from the department of Advanced Mechanics, professors, teachers and administrative staff, with whom I took great pleasure in sharing all these years.

I would also like to thank all my friends and colleagues Zeina el Rawashdeh, Muneeb Ullah Khan, Pengfei Huyan, Yingfan Hou, Jing Xu, Xingxing Liu, Zineb Yanha, Balaji Raghavan, Ravi Matti for their moral support and making my stay at UTC filled with fun and enjoyment.

Finally, I would also like to thank my parents for their support and encouragement. To conclude, I express my gratitude towards my husband, Kiran, for his motivation and patience during writing of this manuscript.

And last but not the least, lots of love to my son, Laksh.

Abstract

The concept of micro and desktop factory is highly in demand in micro manipulation and assembly domains. This concept refers to downscaling of production equipments to the size in proportion of the micro parts they are dealing with. It leads to the reduction of energy consumption, cost and production time and at the same time; it allows the development of highly flexible, reconfigurable and modular systems. Based on these developments, this thesis focuses on the development of a highly flexible and reconfigurable conveyance system for the transportation of micro objects that is crucial for a micro factory stage.

The objective of the thesis is to design, model and prototype a flexible conveyor system for the conveyance of micro objects. The system may need to be integrated in a micro-factory which requires high flexibility, reconfigurability and low power consumption. These criteria are considered in the design and concept of the conveyor system. The conveyor is based on a planar electromagnetic actuator that has been developed in the Laboratoire Roberval. It consists of a movable silicon cross shaped pallet with four Permanent Magnets Arrays (PMAs) arranged at its edges and a pair of fixed Planar Electric Drive Coils (PEDCs) underneath each PMA. To generate the motion of the mechanical structure, Lorentz force between the mobile PMA and the fixed PEDCs is used. Finality of this work is to design a smart and flexible conveyance surface composed of a matrix of several similar cells that can be controlled independently to form a flexible conveying path for the silicon cross shaped structure carrying the object to be transported.

An analytical electromagnetic modeling has been developed to design the conveyor. This model computes the electromagnetic forces exerted on the PMAs and displacement of the movable pallet in function of the control signals. The conveyor design is on a square matrix design. Each cell of the matrix is composed of two overlapped pairs of PEDCs arranged orthogonally with respect to each other which enable planar motions of the silicon pallet. This matrix design has the advantage to only locally supply the coils in the neighborhood of the movable pallet then energy is saved. The matrix design configuration allows the independent controlling of several mobile pallets. This technology allows obtaining complex trajectories of several mobile pallets to perform various manufacturing tasks on the same surface without manual intervention. The matrix design ensures low energy consumption, flexibility, reconfigurability and robustness of the system.

To validate the concept, an experimental prototype of 5 × 5 matrix square design of dimensions 130 mm × 130 mm has been developed using a four layer PCB. The first and

second layers of the PCB comprise the orthogonal layers of PEDCs and the fourth layer is used for the external power connections. The influence of the distance between the first and second layer has been studied in order to ensure uniform motion in both directions. The prototype has been manufactured and experimentally tested. Experimental tests of the conveyor surface have been completed and validate the ability of the motion along *x*- and *y*- axes and diagonal motions. Long displacements strokes have been successfully obtained along *x*- and *y*- axis. Using image processing, the displacements of the mobile pallet have been successfully computed.

Experimental tests have shown the possibility of wide area of planar displacements. Numerous experimental tests that include control in open loop, performance characterization as straightness error of movement, position repeatability error, movable load etc. have been carried out in order to qualify the performance of the conveyor system.

High precision is an important requirement in the SEC platform especially when precise positioning of the pallet is required. In order to improve the precision of the SEC platform, a closed loop control could be implemented. For that, a compact and non-contact sensor can be used in order to not disturb the silicon pallet motion. A solution based on an optical sensor and a microfabricated mirror that has been developed at the Roberval laboratory of the Université de Technologie de Compiègne is selected.

The problematic of the previous study is to measure continuous displacement from the two FOP signals. As mentioned earlier, the useful measurement is the linear parts of the signals which should be filtered to achieve an online continuous displacement measurement. For that, a precise and robust signal processing algorithm is required that allows switching between the two signals. In this work, the proposed algorithm has been developed to ensure the continuous measurement of a long-range displacement by considering various parameters including velocity, frequency, shape and form of the experimental signals. Experimental signals are used to test and validate the principle of signal processing algorithm. In the end, performance and robustness of the algorithm is discussed with the results obtained using experimental signals.

Keywords: micro conveyor, smart surface, flexible conveyor, micro factory conveyor, electromagnetic actuator, fiber optics, optical sensor, fiber optic displacement sensor, high resolution displacement sensor, long range displacement sensor

List of Figures

Chapter 1: State of art

This chapter reviews the state of art of the micro-factory concept and then focuses on micro-conveyance systems. It starts with the discussion and the definition of micro and desktop factories. Brief overview of current activities (both academic and commercial) around this trend is then discussed. Different elements such as micro machine tools, micro assembly units, micro conveyors etc. that are involved in this concept are presented. After that, the state of art particularly focuses on planar conveyance systems that could be integrated into micro-factories. At the end a short review on the existing measurement techniques for long range that could be applied to measure displacement of planar conveyance systems is proposed. Finally, an overview of the background and objectives of this work are presented.

1.1 Concept of micro and desktop factory

With the increasing trend of products miniaturization, the production machinery remaining at conventional size is often inappropriate for such products. Hence, the terms desktop and micro factory have been originated that refer to downscaling of production systems to match the size of the micro parts they are producing or manipulating and that can be placed on a desktop or manually moved without any lifting aids. In this context, the first development has been reported from the research conducted in Japan in 1990's where small machines (micro lathe, micro mill, micro drill ...) were developed in order to produce micro parts and machines where "micro" does not necessarily refer to the size of parts or their features, or the actual size or resolution of the equipment. Instead, micro refers to a general objective of downscaling production equipment to the same scale with the products they are manufacturing [OKAZ 2004].

These micro machines were developed with the ideas of "desk top", "palm-top", and mobile factories. Energy saving and economizing were some of the primary goals in this research. Since then various researches have been carried out in this context around the globe. Several advantages are speculated in previous works ranging from low energy consumption and reduced need of resources leading to low capital investment, to the increase in reconfigurability and flexibly which reduces production time specifically in case of complex and highly customized objects.

The idea behind the concept of micro factories is to make small parts with a small machine. The smaller the machine, far fewer resources will be needed to make machines themselves

and far less energy will be required to run them. Thus, high speed low cost machines are required. To achieve high speed of production, the distance and mass has to be minimized that is only possible in the microfactory system. Energy consumption is also then minimized [ANIM 2005].

Definition

A micro factory can be defined as a small manufacturing system to produce small parts with small machines scaled down to the level of the parts it is producing or manipulating in order to achieve higher output in less time and low cost, and reduced consumption of both resources and energy.

1.2 Characteristics

The main characteristics of the microfactories that are needed to meet the requirements of the micro world are discussed here

Flexibility

Flexibility is required to easily reconfigure a manufacturing system in response to process requirements and product demands. It can be done by enabling rapid change of production that allows the system to orient and displace in parallel several objects using automatic control. Thus, flexible systems are faster which in turn cut the cost and save energy.

Modularity

Modular micro factories can be easily rearranged according to the production requirement in a short time. Different modules, each having specific production task, can be installed in the same production unit. It allows performing various micro manipulation/manufacturing tasks at the same time for different applications. It can be done just by changing the combination of product modules. Thus, modularity leads to much faster production.

Reconfigurability

Micro factories have to be reconfigurable that means it should be able to adapt to product and volume variants. Also, it is easy to produce customized products using the same production unit. This is possible through rearrangement or changing of system's components. This is made easier by implementing the concept of modularity.

Energy saving and economically cost effective production

Economizing and energy saving are the basic aspects of any microfactory system. It consumes less amount of energy due to less space, short transfer distances, small machinery and avoid all the wastage of raw materials which leads to running cost. All the above factors make microfactory concept a highly cost effective approach for micro manufacturing. This makes them environment friendly because it saves energy, materials and resources. Due to its small size it creates less pollution, noise and vibrations for the workers and factories' neighbours. It facilitates easier control of waste and pollution.

Faster, more precise and accurate systems

Due to constant variation in customer demands and technology, faster and more precise systems are in high demand that can meet the requirements of the micro world. With flexible, modular and reconfigurable design, the possibility of faster response time than current production unit in case of any change in the process or product is high.

On the other hand, micro-factories have to operate with very small components, so the manual intervention is very difficult. Thus, they work with high precisions in the scale of micrometers.

Micro level scale

The scale factor is a very important issue in the micro world. The downsized production systems are essential for manufacturing small scale products. It can only be achieved by working with specific machines that are able to work with micro components with high precision. For that, a specific information and organization system is required to control and manage the small scale components on the microfactory. This is essential to acquire specific characteristics adapted to the micro scale requirements.

1.3 History of microfactory concept

As mentioned earlier in this chapter, the term micro and desktop factory has been originated from the research conducted in Japan in the 1990's at the Micromachine Center (MMC), a research organization and the Mechanical Engineering Laboratory (MEL). The research started with the idea of miniaturizing the machines necessary to produce micro parts [OKAZ 2004]. The entire project lasted from 1991-2001. While a desktop factory, palm top machine tools, a microfactory and onsite production facility were planned, the main goal was saving energy and economizing.

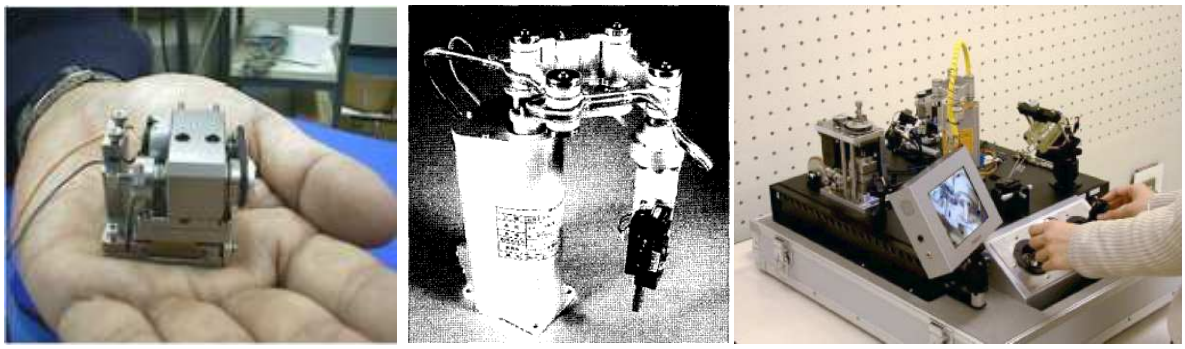

(a) (b) (c)

Figure 1.1 Downsized machine tools (a) Microlathe [LU 1998] (b) Micro transfer arm [MAEK 2001] (c) Portable microfactory [OKAZ 2004]

The first attempt was a microlathe (Figure 1.1(a)) smaller than a human palm that leads to further studies on how to downsize machine tools [LU 1998]. And then two more downsized machine tools were developed a micro milling machine and a micro press. These machines were then assembled on a desktop, together with a micro transfer arm (Figure 1.1(b)) [MAEK 2001] and a micro manipulator. After successful experiments, the components of the desktop machining microfactory were then integrated into a single portable box of 625 × 490 × 380 mm and weighing 34 kg in dimensions (Figure 1.1(c)). The machines were manually controlled using two joysticks and visual aid for the operator. Power consumption during operation was 60W which was way less than the conventional manufacturing systems. In this way, the first prototype of a portable industrial plant was developed [OKAZ 2004]. The microfactory concept was then introduced internationally and developments in this context became a driving force for further research in this field.

Afterwards, the research work began in several laboratories around the world including the USA and few European countries. The Franhofer Institute for Manufacturing Engineering and Automation in Germany has developed a unique "Mini-Factory" system with modular

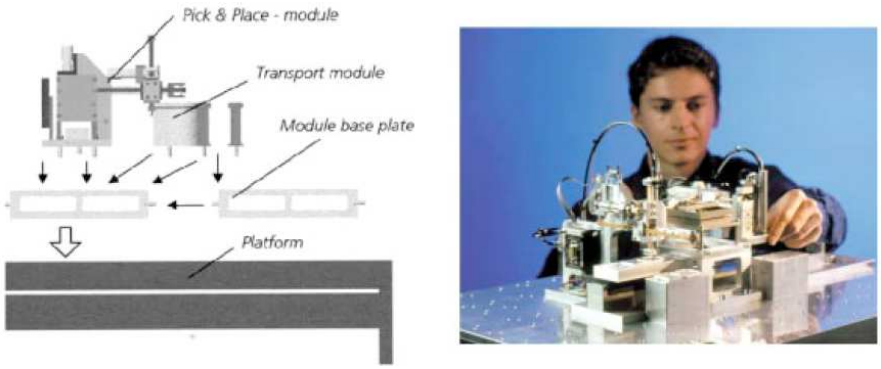

Figure 1.2 Mini factory system [GAUG 2002]

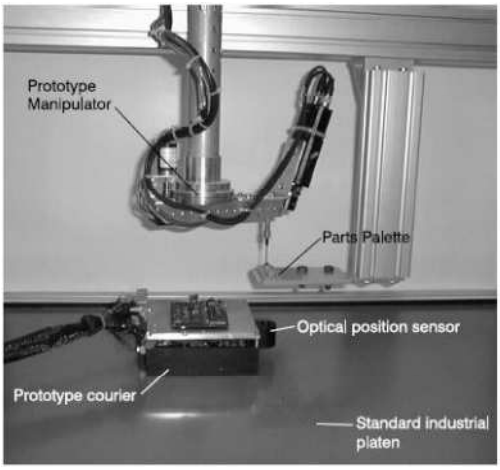

Figure 1.3 Prototype microfactory hardware[GOWD 1999]

construction, including base platform, actuators, transfer units and control units (Figure 1.2) [GAUG 2002]. The system was extended into an Advanced Modular Microproduction System, aiming at a marketable, highly flexible production system.

In the USA, another development on microfactory at the Robotics Institute of Carnegie Mellon University in Pittsburgh has been reported [GOWD 1999]. Reconfiguration and a high precision of the system were the main aspects of the system design. The prototype is a 4 DOF high precision assembly system (Figure 1.3). The Architecture for Agile Assembly (AAA) has been developed which is a comprehensive, integrated framework that is designed to ease the transition between programming stage used for design phase to the stage where the simulated results are used to minimize the deployment and integration time of the physical machines. An integrated interface tool which can be used throughout the life-cycle of a developing AAA factory, from its design to its operation has been created.

Today, with the increasing trend of miniaturization, the concept of "microfactory" has become quite a range among the laboratories and enterprises working on micro manufacturing in almost every field such as biomedical, communication, electronics etc. At first, they started with the machining of mechanical parts, then fabrication of MEMS devices was the focus and recently the concept has been extended to the production of semi conductor devices. These changing targets have proved that downsized compact manufacturing systems can be eco-efficient for production in some industries [MISH 2011]. With the possibility of additional features such as modular and reconfigurable manufacturing system designs, it is easier to configure the micro factories according to the product requirement.

With the frequently changing customer requirements, increasing number of product variants, small batch sizes, short lifecycle times of products and fast emergence of new technical

solutions, the new manufacturing systems should be able to adapt with these changing requirements. These changes are well adapted by the development of reconfigurable manufacturing systems. Reconfiguration allows adding, removing or modifying specific process capabilities, controls, software or machine structure to adjust production capacity in response to changing market demands or technologies [SETC 2004].

1.4 Different components and categories involved in a microfactory

Micro factory usually is an integration of several components, each performing a specific function for the micro production [DESC 2004]. In this work, a microfactory is described into three main parts; a 'Platform of Production of Microproduct' on which the "trade stations" are laid out which are referred to the manufacturing or production stations for a specialized manufacturing or manipulation task such as assembly station, forming station, laser machining station etc. (Figure 1.4). The next is the 'Organisation System' which controls the specific task of each station for the transformation of the microproduct. These trade stations must be configured on the platform in order to fulfil the tasks they are supposed to be performing. And the microfactory must be able to manage flows of the microproducts and micro components allowing its operation and its provisioning.

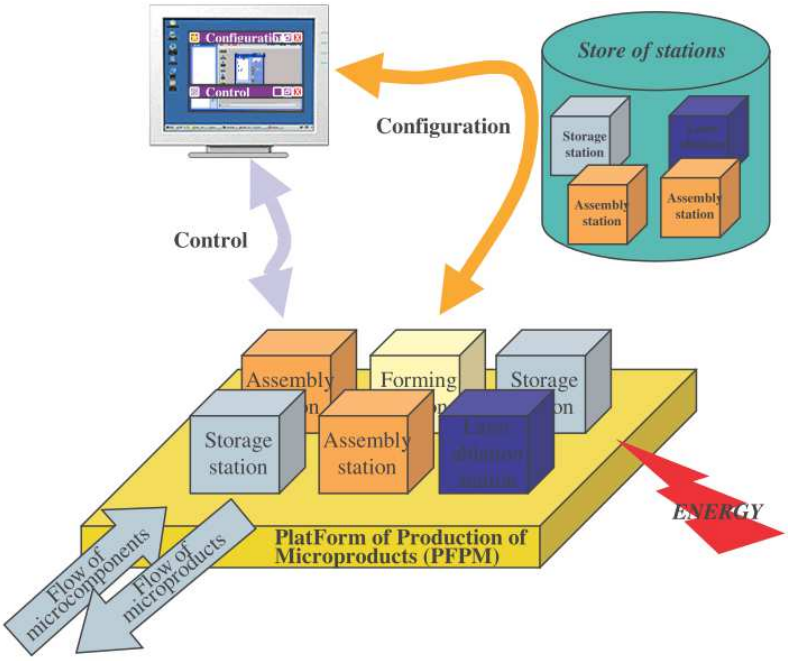

Figure 1.4 Presentation of the microfactory structure[DESC 2004]

According to the Micro and Desktop Factory Roadmap presented by a research team of Tampere University of Technology (TUT), different concepts in the desktop and micro factory systems are classified into different categories based on the applications [TUOK 2012]. The classifications with some examples are described in the subsections below.

1.4.1 **Miniaturized machining units.**

In China at Tsinghua University, downsizing of machine tools led to the development of a micro Electro Discharge Machine (EDM) for drilling spray holes of diesel injector nozzles with high emission standard. The developed equipment has been implemented and shows the holes' space accuracy being better than ±0.1° and the holes' size accuracy being controlled within ±2 µm for the hole diameter range from Ø140 µm to Ø300 µm (Figure 1.6 (a)) [TONG 2013].

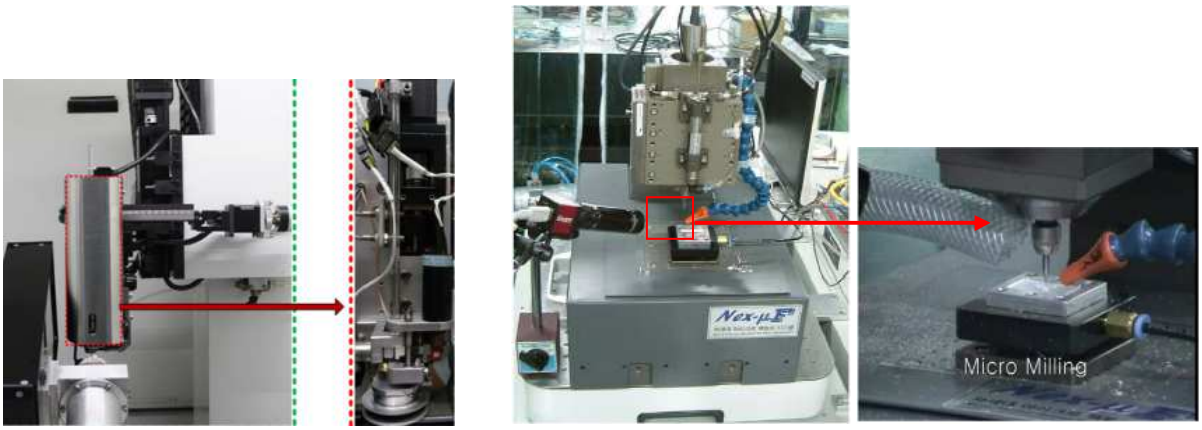

(a) **(b)**

Figure 1.5 (a)The miniature vertical milling machine [RO 2008] (b) micro-EDM equipment [TONG 2013]

A development on miniature vertical milling machine with air bearing guide systems and spindle to be used for the machining of micro-, meso- parts has been reported in Korea at Korea Institute of Machinery and Materials [RO 2008]. It is a 3- axis milling machine designed to achieve high accuracy within the working volume 35 mm × 35 mm × 33 mm (Figure 1.6 (b)).The designed machine was built with numerical control system and integrated in a Microfactory system. Micro metal forming have also become an attractive option for the mass production of micro products in the industries. The experience of miniaturization gained with the concept of micro factory have also been entered in the micro forming equipments [QIN 2006]. Machines, forming-tools and handling of micro-metal-parts are, for example, critical elements that significantly determine the industrial applications of micro-forming.

1.4.2 **Miniaturized robotic and assembly cells**

In this subsection, robotic cells and assembly cells of microfactory are described. In literature, miniaturized robotic and assembly systems have been developed for different micro manipulation and assembly tasks. These include for example; pick and place mechanism using small transfer arms, grippers and manipulators and, complex assembly of micro parts. It requires high precision manipulators, motion planning and control. Some of the developments in this category are presented here.

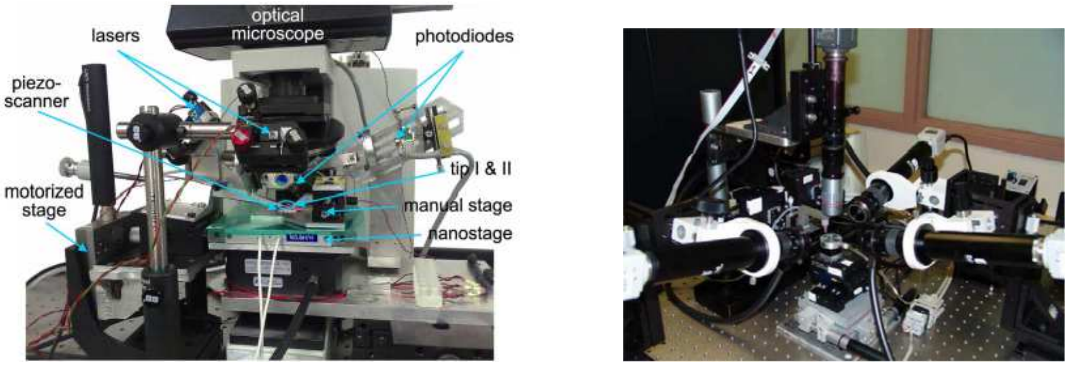

(a) **(b)**

Figure 1.6 (a) Flexible robotic system for pick-and-place manipulation [XIE 2011] (b) Microassembly system at Texas Microfactory [DAS 2012]

A mini assembly cell has been designed for a commercially available 8 mm diameter miniature planetary gearhead. This system has achieved assembling planetary gear units independently. This has been designed for the TOMI (Towards Mini and Micro Assembly Factories) microfactory in Tampere University of Technology in Finland [UUSI 2004].

A research work on flexible robotic system based on atomic force microscopy for multiscale applications manipulation and assembly from nanoscale to microscale has been developed in France. The project is supported by the French Research Agency (ANR) [XIE 2011]. The experiments proved feasibility of the system in three different configurations; 3-D microsphere manipulation, 3-D nanowire manipulation, and parallel nanomanipulation of nanoparticles (Figure 1.6 (a)).

Another flexible micro assembly system equipped with an automated tool changer has been developed at FEMTO-ST Institute in Besancon, France [CLEV 2008]. The system consists of some dedicated tools that can be used to achieve specific tasks. A microgripper that is integrated in four degrees of freedom system and a tool changer which is able to exchange

automatically the tip part of the microgripper. A compliant table has also been developed to limit the forces applied during the micromanipulation tasks. This system is mainly useful for insertion tasks.

With an objective of low cost, automated and very high precision assembly at the micro and nanoscales, an assembly and packaging system for manufacturing of complex micro-nano devices has been developed for Texas Microfactory. In this work, assemblies of complex microsystems such as microspectometer and the microrobot Arripede has been demonstrated (Figure 1.6 (b)) [DAS 2012].

1.5 Layout of Microfactories

Using these miniature components that have been developed, based on different applications, different layouts of microfactories have been developed. In this work, two different layouts, as a set of small size equipment and modular factory are discussed.

1.5.1 Microfactory as a Set of small size production equipment

Microfactory usually consists of miniaturized machining units to produce components, a small manipulator, transfer arm or conveyor system to transport the components and a small size assembly unit or a micro manipulator to assemble components [TUOK 2012]. The primary goal of the researches has been miniaturization of the machines. As a result, versatile microfactory architectures and systems have been developed.

An automated microfactory was developed at University of Illinois Urbana-Chanpaign

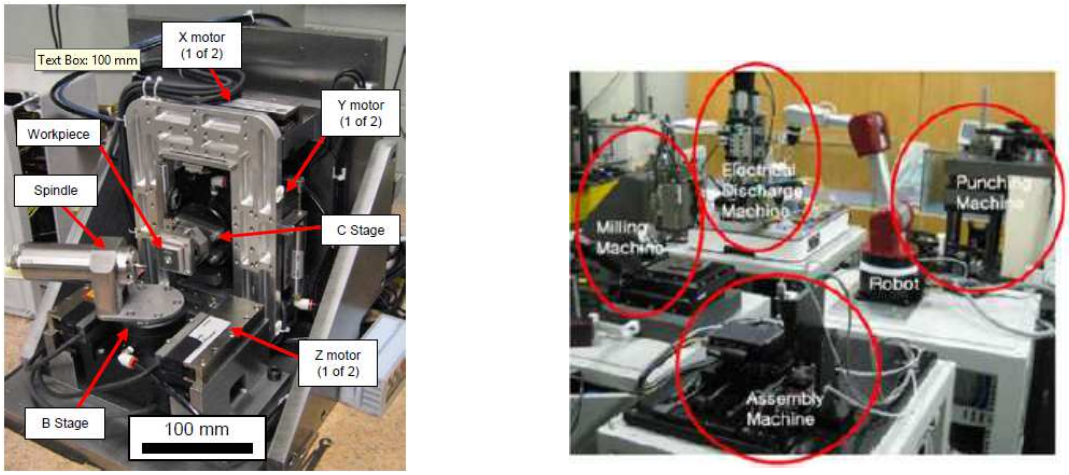

(a) **(b)**

Figure 1.7 Microfactoris (b) Automated Illinois Microfactory [HONE 2006a; HONE 2006b] (a) Mosaic [PARK 2007]

(UIUC) in USA in 2006. The system was based on a 900 × 900 mm^2 pneumatic vibration table shown in Figure 1.7(a) [HONE 2006a; HONE 2006b]. The system consists of milling/drilling machines as well as a metrology station. Specific pallets were developed to transfer the parts. The machines were operated by a computer. In Korea, the first microfactory was developed at Korean Institute of Machinery and Materials (KIMM) in 2006. The system consists of a micro milling machine and a punching robot (Figure 1.7 (b)). It was used to manufacture a micro pump [PARK 2007]

1.5.2 **Modular and Desktop Factory**

Currently, the primary focus is on the development of modular microfactory platforms. These platforms provide reconfiguration in a short time, without much complexity and without buying new machines and equipments. This type of systems facilitates modularity and reconfigurability, parallel processing, and flexible rearrangement. All these parameters are essential specifically for the production of highly customized micro objects. Modular designs came into light by the development of first modular desktop-size microfactory "Advanced Modular Microassembly System (AMMS)", developed by Frauenhofer IPA in Germany in 2001 [GAUG 2004]. The plug and produce system is based on 600 × 400 mm^2 planar motor table. Products and /or components are placed on moving carriers, which move with a friction-free air bearing on the planar table.

Afterwards, Tampere University of Technology (TUT) came with the modular microfactory concept for various applications. The TUT-microfactory is a modular construction kit type concept with easy and rapid reconfigurability for different manufacturing processes of hand held size or smaller products (Figure 1.8 (a)). The system structure is designed with an idea

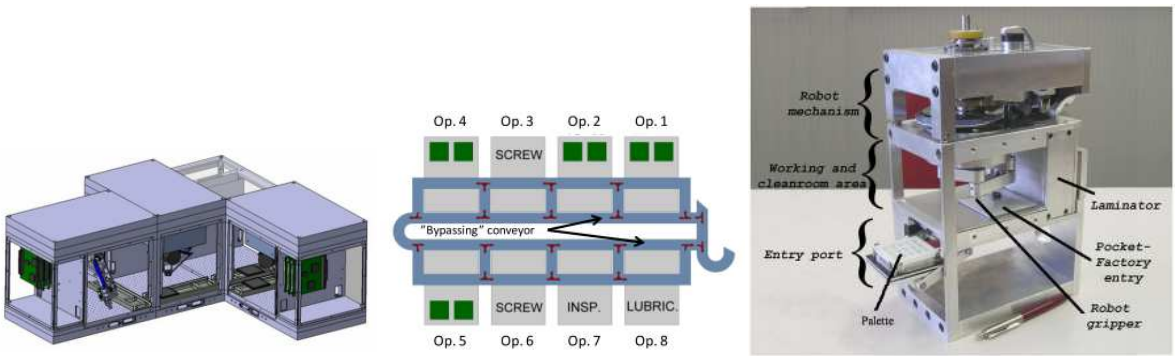

(a) **(b)** **(c)**

Figure 1.8 (a) Example of an integrated micro assembly factory (b) Microfactory system for an integrated assembly process chain [JARV 2010] (c) Pocket factory [VERE 2005]

that a base module can work as an independent unit including all needed auxiliary systems. The outer dimensions of one module are 300×200×220 mm [JARV 2010]. A modular microfactory for high volume assembly of watch mechanism has been developed (Figure 1.8 (b)). This system is based on clusters of TUT-microfactory modules and each cluster performs a chain of assembly process and consists of multiple microfactory modules. Belt conveyors have been proposed that pass through the micro factory process modules for a single chain of assembly process. Later, they have introduced a modular microfactory system for gas sensor assembly [SILT 2011]. It consists of two TUT microfactory cells, which are connected together with standard cell interface. The dimension of single TUT microfactory base module is in this case 200 × 300 × 230 mm^3, upon which number of process modules are stacked.

The first microfactory concept with the integrated clean room called the Microbox Pocket Factory has been developed in Switzerland at Laboratoire de Systèmes Robotiques (EPFL) [VERE 2005]. The size of the included miniaturized clean rooms is typically 1dm3 for each module. These are able to clean at 100 parts/h. The microfactory is also equipped with an entry port enabling clean transfer to unit, a 4DOF robot for assembly tasks, sensors for process control and a filtration system

In the last few years, another development has also been seen in Sabanci University in Istanbul, Turkey. They have developed a desktop microfactory for High Precision Assembly and Machining. It consists of several functional modules such as two parallel kinematic robots for manipulation and assembly, galvanometer laser beam scanning system for

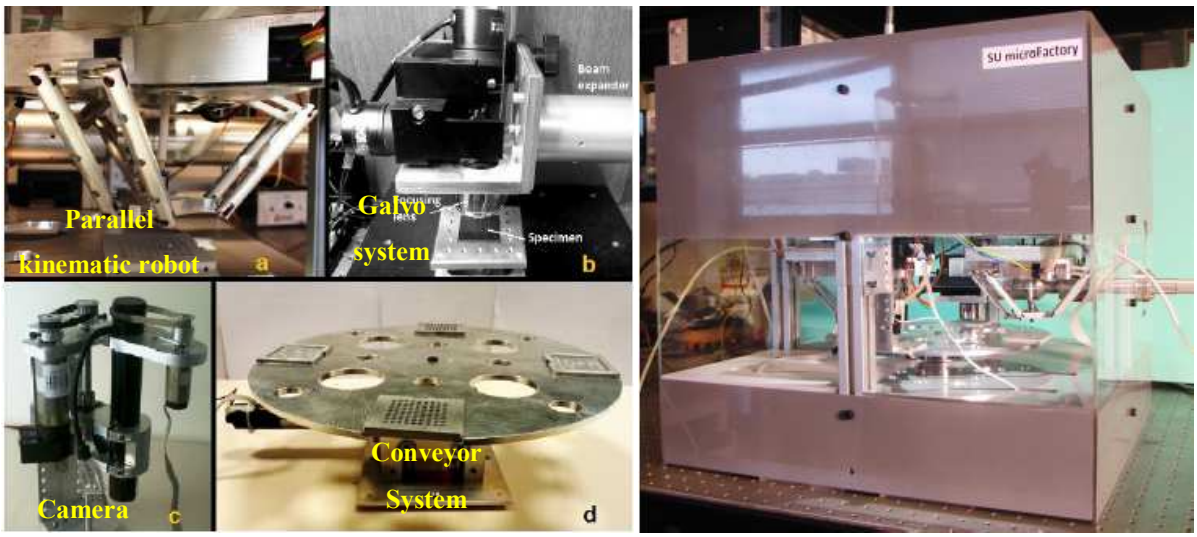

(a) **(b)**

Figure 1.9 Desktop factory for high precision assembly and machining (a) Microfactory modules (b) Desktop factory [ZHAK 2014]

micromachining, camera system for inspection and a rotational conveyor system for sample part delivery (Figure 1.9 (a)) [ZHAK 2014]. The overall mechanical structure of the proposed microfactory facilitates modularity and reconfigurability, parallel processing, flexible rearrangement of the layout, and ease of assembly and disassembly of the whole structure.

In the above examples of microfactories, it has been observed that a micro module to transfer the objects from one module to the other one is essential. Micro conveyor is one such module whose main function is to carry the micro objects and transfer them to the desired location within the micro factory. In the next section, some developments in this context are described.

1.6 Micro conveyor systems

In order to obtain greater reconfigurability and flexibility, an automated transportation system is an essential requirement for a microfactory system. A micro conveyor is a micro module that is used for transportation in micro factories. Its main function is to transfer the micro objects (manufactured parts or raw materials) between different micro modules within the micro factory. This is even true due to the scale of the device in microfactory which makes manual intervention difficult or rather impossible.

The micro-conveyor can also contain a pallet that can carry the micro-components to transfer from one position to another. The pallet trajectory can be defined by the conveyor geometry. In this case, manual intervention is then needed to change the part trajectory by modifying the conveyor geometry. It can also just be a plane surface where different kind of shaped micro-components can be carried, though, in this case, limited by the fact that the micro-component must have at least one side that is planar.

Currently, the primary focus is on the development of modular microfactory platforms. These platforms provide indeed reconfiguration in a short time which is essential for the production of highly customized micro objects. The reconfiguration time is short because it can be realized only using the control without the need of manual intervention. Hence, the design of a specific conveyance system with high reconfigurability and flexibility is crucial for the conveyance of micro objects within the microfactory.

In most of the cases but not all, micro-factories are organized in plane architecture with the different modules. The micro conveyors are then based on planar micro-actuators. Depending on the applications, several actuation technologies are being involved that are required to produce displacement. Actuation technology decides the surface and shape of micro conveyor

and defines path on which it moves or if guided through. Furthermore, based on different actuation techniques, numerous multi dimensional micro conveyors have also been developed in the past. Following are the some of the actuation technologies that are used for actuation in positioning systems and conveyors.

- Pneumatic actuation technology
- Thermal actuation technology
- Electrostatic actuation technology
- Piezoelectric actuation technology
- Electromagnetic actuation technology

In further subsections, principles of some of the actuation techniques that are widely used in micro conveyors systems are discussed and their applications are given..

1.6.1 **Pneumatic actuation principle**

In pneumatic actuation based positioning systems, the pressure of the compressed gas, such as air, nitrogen, etc., is injected via small inlets (called nozzles) utilized in order to move and levitate the object at the same time (Figure 1.10(a)). In this method, the object is moved using air flow which is induced by injecting strong air jets. For that, several nozzles fabricated into a flat mechanical structure are used that generates an air flow. Pneumatic valves are used to control the inlets of the nozzles and a strategy is used to operate these valves to achieve the motion direction.

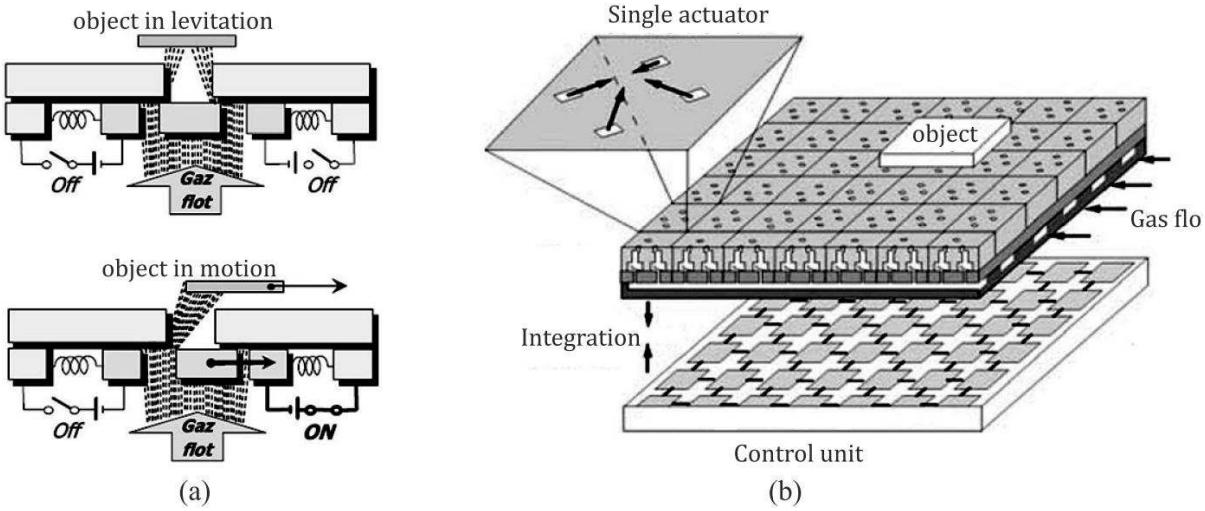

Figure 1.10 Distributed conveyance system (a) Levitation and motion state of an object (b) Actuator assembly design[CHAP 2004]

One of such distributed conveyance system to move light objects have been developed [CHAP 2004]. The conveyor has 35 mm × 35 mm conveyance area with 560 MEMS actuators. The principle of working of a single nozzle is shown in Figure 1.10 (a). The nozzle inlet is controlled using a beam electrode. The float moves towards right, when the right side electrode beam is "ON". It leads to the gas to flow from left side of the float through a nozzle which creates a rightward thrust in the object. The conveyor design is shown in Figure 1.10 (b). Each cell of the conveyor is 1 × 1 mm^2 and the size of each nozzle is 165 × 590 μm^2. The conveyor system use nitrogen gas at 17 kPa and can carry upto 4 mg weight. Though it is based on digital actuation, the levitation position and motion speed can be set by controlling the pressure of the inlet gas.

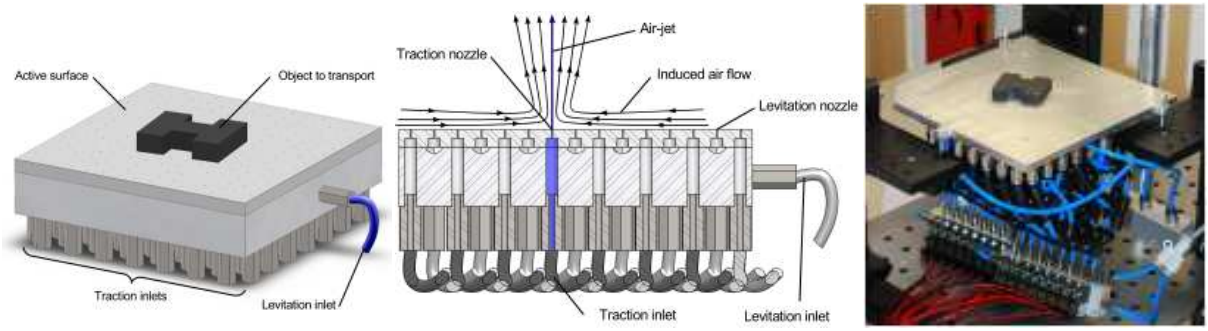

(a) **(b)** **(c)**

Figure 1.11 Pneumatic conveyor system [DELE 2010](a) Global View (b) Cross section view (c) Experimental prototype

Another development has been reported by FEMTO-ST institute in Besancon, France. They have proposed a contactless conveyor for handling clean and delicate products using induces air flows [DELE 2010]. This conveyor system is based on the aerodynamic traction principle and is able to convey without any contact flat objects like silicon wafer, glass sheets or foodstuff on a air hockey table thanks to a new traction principle. The object is moved indirectly by an air flow which is induced by some strong vertical air jets. These strong jets come from some specific orifices of the air-hockey table. The induced air flow surface is a 120 × 120 mm^2 square surface. The object is maintained in constant levitation with the help air cushion by the airflow that comes through the lateral common air inlet. The pneumatic conveyor system is presented in Figure 1.11. The model of the surface has been established for one meter long active surface. The maximum velocity of the object with one meter long active surface was given 83.50 mm/s with 2 valves open and 166.98 mm/s with 4 valves open.

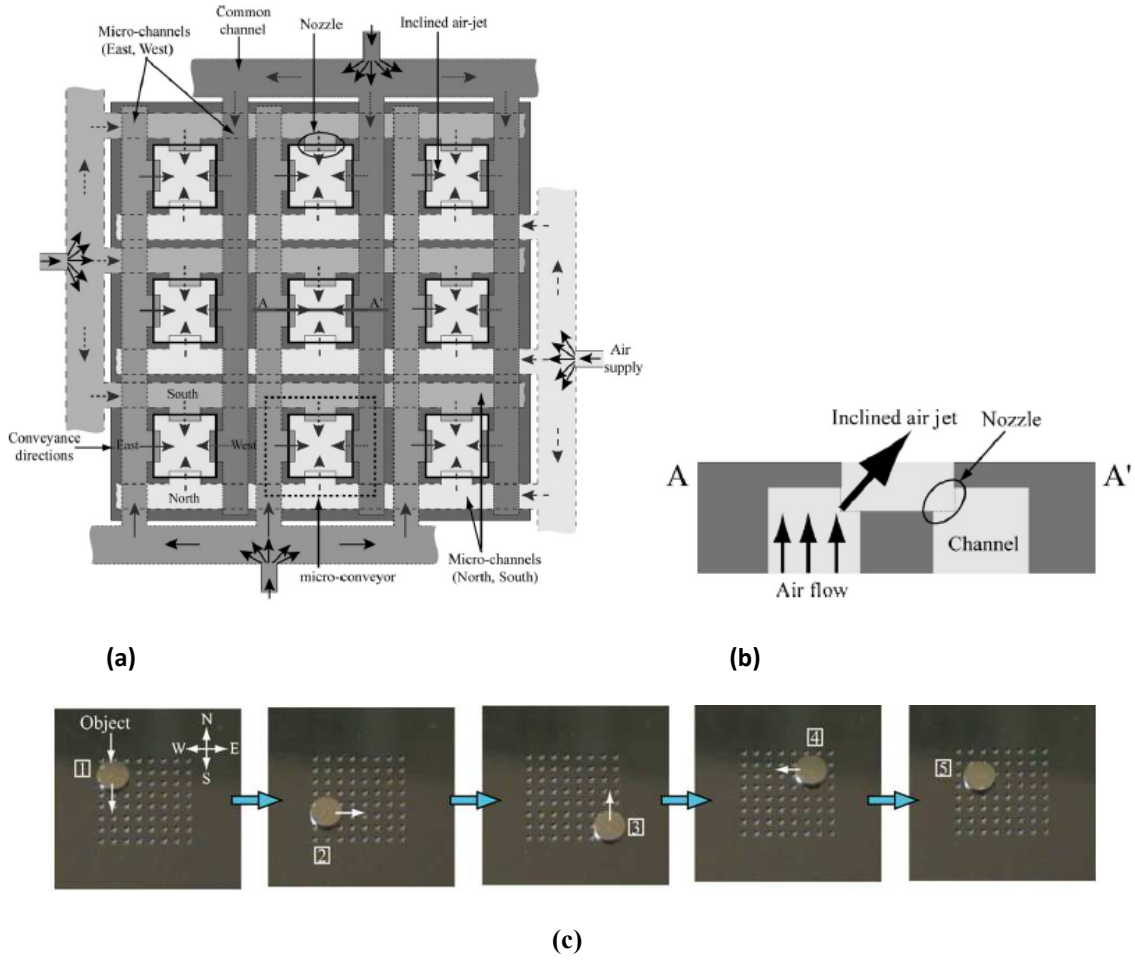

Figure 1.12 Pneumatic micro-conveyor systems [YAHI 2012; ZEGG 2010]((a) Principle of conveyance (b) Scheme of actuator (c) Conveyance of silicon chip on the prototype

Another 2D pneumatic micro-conveyor based on MEMS technology for micro manipulation has been developed at FEMTO-St institute in France [YAHI 2012; ZEGG 2010]. This device is based on array of micro actuators which generates oriented air jets in four directions (North, East, West and South) and generates the motion of the object. Figure 1.12 (a) and (b) shows the top and cross section view of the micro conveyors, respectively. The actuator is composed of a set of similar blocks of micro-conveyors and each conveyor consists of a square orifice and four nozzles. The compressed air flows through the common channel and then spread to the micro channel and ejects through the nozzles. Air can then be ejected by the nozzles resulting four conveyance directions. The device surface is a 9×9 mm^2 square design which is composed of a stack of three layers.

Experimentally, the device is able to convey a silicon chip of 3 mm in diameter, 0.5 mm thick and 2 mg weight. The displacement of the chip is observed with the air pressure of 20 kPa. In the experiment, the mean velocity for conveying the object from position (1) to (4) was

around 2–3 mm/s (Figure 1.12 (c)). Four independently controlled pneumatic electro valves were used in order to control the air flow and the movement of the object.

1.6.2 **Thermal actuation principle**

The second physical principle used for actuation is the thermal actuation principle. It is used under different forms. One is based on thermal phenomenon which is based on heating or cooling of the fluid in order to vary its volume and therefore, the pressure of the chamber in which it is placed is changed. This pressure variation causes the tilting in one direction or the other of the movable part of an actuator. Thermomechanical method is also used for actuation which is based on the expansion of one or more beams by heating. Thermal actuation can also be done by using Shape Memory Alloys (SMA) which deforms, to regain initial shape, under the action of a variation of temperature.

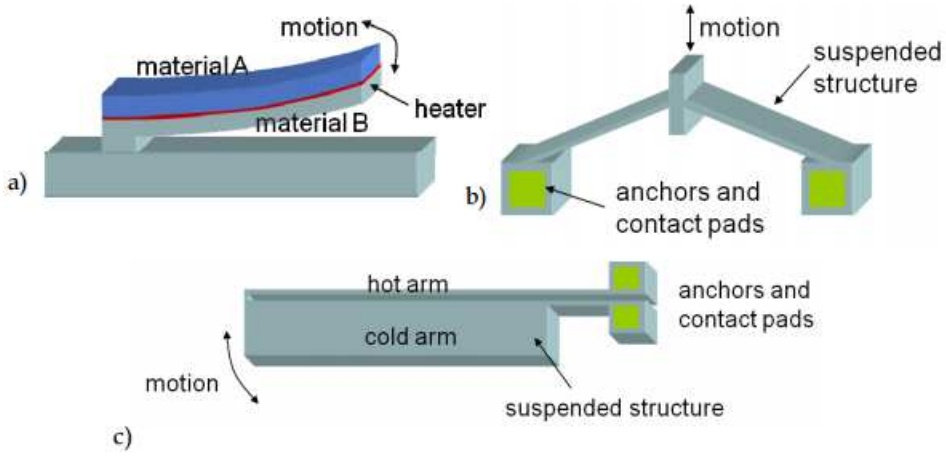

Figure 1.13 Schematics of thermal microactuators (a) bimaterial (b) bent beam (c) bimorph [PHIN 2012]

Figure 1.13 shows schematics of three thermal microactuator designs: bimaterial, bent-beam, and bimorph [PHIN 2012]. Bimaterial actuators consist of two materials with different coefficients of thermal expansion and function similarly to a bimetallic thermostat (Figure 1.13 (a)). Upon resistive heating, the material with higher value of coefficient of thermal expansion will expand more with respect to other resulting in motion

Bent beam actuators have angled legs that expand when heated, providing force and displacement output as shown in Figure 1.13(b). Similarly, a bimorph consists of two metallic arms (hot and cold arms) fabricated in the same material (Figure 1.13 (c)). The cross section of the hot arm is smaller than the cold arm. When current is injected, the hot arm will expand more due to smaller cross section relative to the cold arm. Due to the difference in volumetric expansion the motion occurs.

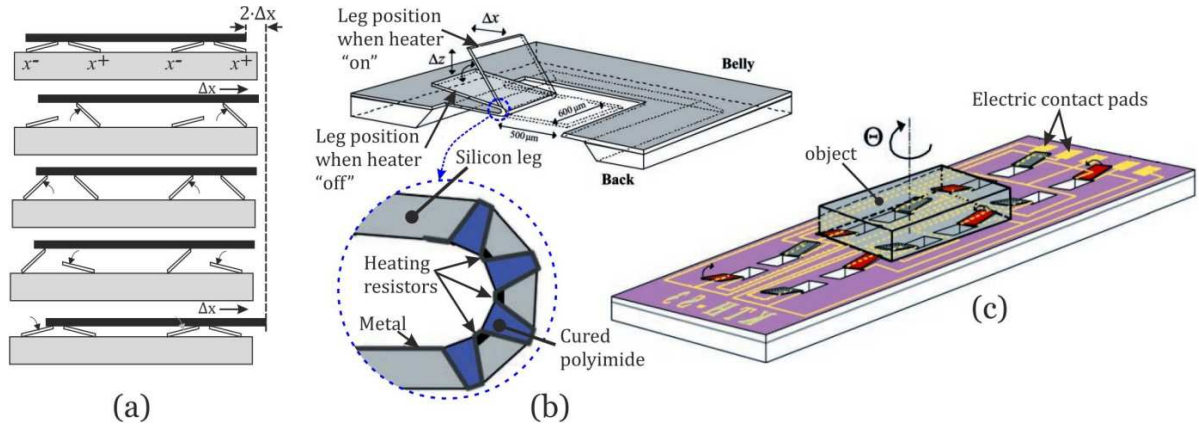

Figure 1.14 (a) Actuation principle (b) Single silicon leg (c) Micro conveyor [EBEF 2000]

A micro conveyance system based on arrays of movable robust silicon legs has been developed. Figure 1.14 (a) represents the step by step actuation technique for moving a flat object in the horizontal plane. The conveyance system has been realized with curved polyimide joints (Figure 1.14(b)). The deformation of the joints occurs when electrically heated, which create "Δz" and "Δx" displacement. The polyamide joint regains the original position when the heating is turned off. Based on this actuation concept, a conveyor platform composed of several polyamide actuators using heating resistors has been developed [EBEF 2000]. The fabricated conveyor (Figure 1.14 (c)) consists of a 15×15 mm^2 chip composed of 12 silicon legs to move a flat object at millimeter range. It can perform translational and rotational motion in horizontal plane. The maximum conveyance velocity of 12 mm/sec has been achieved.

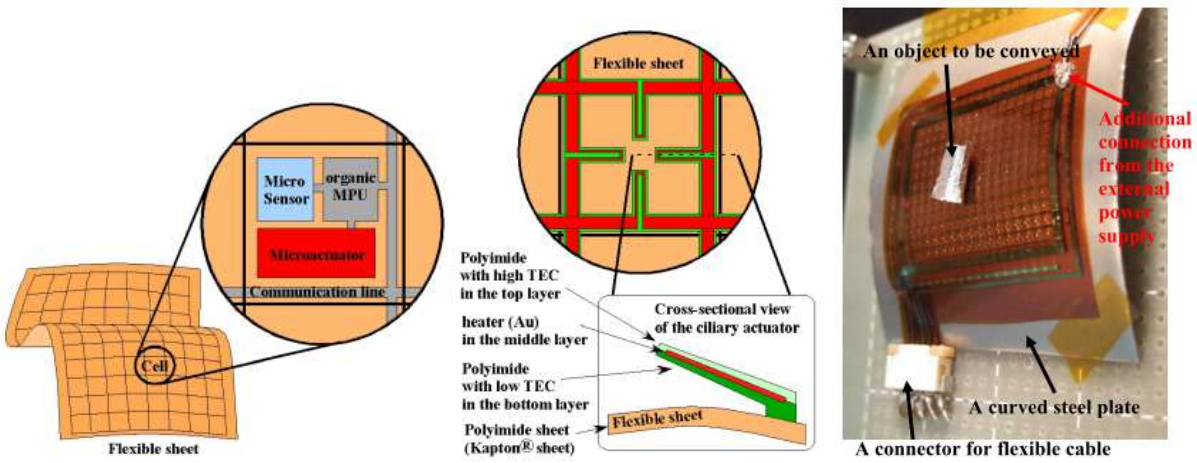

Figure 1.15 Smart MEMS sheet [ATAK 2013] (a) Micro actuator array (b) Four ciliary microactuators in a cell (c) Experimental prototype for 2D manipulator

A thermally driven micro-actuator array on a flexible sheet based on the concept of "smart MEMS sheet" has been fabricated and tested at the University of Tokyo in Japan [ATAK 2013]. The actuators array consists of thermally driven cantilever actuators and a flexible sheet (Kapton® sheet). 768 actuators have been fabricated on a sheet of 18 × 24 mm^2 and used as a 2D manipulator on a curved surface. The system consists of several cells and each cell has micro-actuators integrated with a Micro Processing Unit (MPU) consisted of organic flexible electronics and sensors shown in Figure 1.15 (a). Four cantilever-type actuators are present in each cell, which are addressing four orthogonal directions (Figure 1.15 (b). The actuator is composed of two layers of polymide with different thermal expansion coefficients and a metal heater between the layers. When current flows in the heater, the actuator moves down to the substrate. An aluminium paper of 7.5 × 4.5 mm^2 with 10 mg of weight was conveyed on the flexible sheet. The experimental prototype as a 2D manipulator is presented in Figure 1.15 (c).

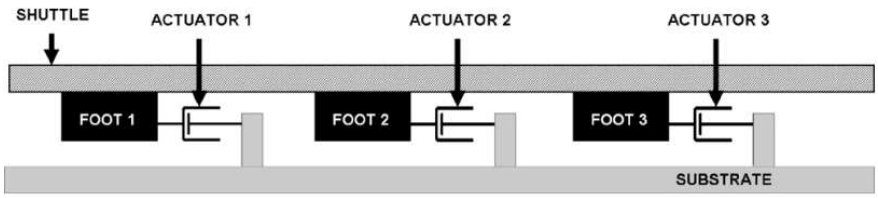

Figure 1.16 Schematic showing side view of a frictional micro-conveyor [SHAY 2008]

Another micro conveyor based on conventional thermal actuators has been developed. The operation of the frictional MEMS micro-conveyor is based on frictional forces [SHAY 2008]. The schematic of side view of the conveyor is shown in Figure 1.16. It consists of two parts; a shuttle and a driving unit that moves it. The driving unit consists three inverted feet than can be moved by thermal actuators. Driven by thermal actuators with a proper sequence of

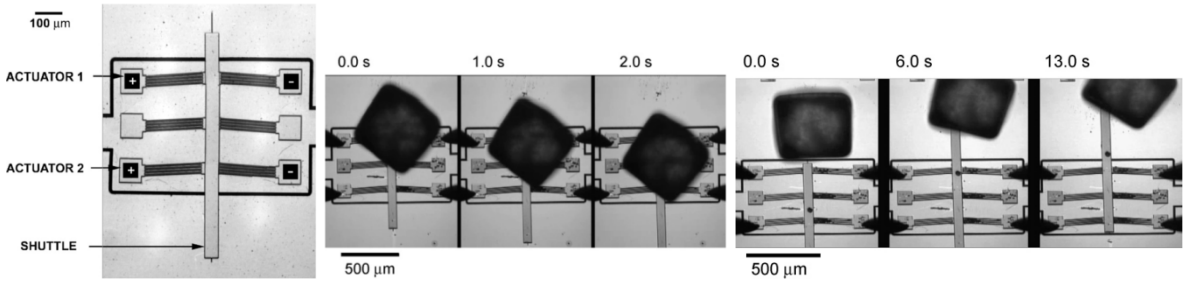

(a) **(b)** **(c)**

Figure 1.17 micro-conveyor with shuttle resting on a driving unit feet [SHAY 2008](a) photograph of micro conveyor (b) moving a grain of salt downwards in the plane of the page (c) pushing a grain of salt upward in the plane of the page

signals, it can move a shuttle resting on a driving unit (Figure 1.17 (a)), over long ranges exceeding hundreds of microns. The direction of the motion is reversible. The upward and downward of the actuators are shown in Figure 1.17 (b) and (c), respectively. The conveyor can be operated in two modes; either two or three feet being driven. The range of the conveyor is only limited by the length of the shuttle. The micro-conveyor driving unit has an area of 400 × 650 μm^2 and can move a 750 × 50 μm^2 shuttle. It is capable of moving external load weighing more than 150 µN. The micro conveyor can transport micro-sized objects at a controllable velocity. This conveyor can be applied for micro-transport of other MEMS components or materials such as micro-lenses, micro-mirrors and micro-stages, or as actuators for micro manipulators with multi degrees of freedom. There is a possibility of extending the concept to multi degrees of freedon (DOF).

1.6.3 **Electrostatic actuation principle**

The third physical principle encountered in the literature for planar actuators is the electrostatic one. It is based on the generation of a force between two electric charges. An electrostatic actuator generally consists of two facing surfaces called electrodes or armatures. These surfaces are charged in opposite or identical manner and allow the generation of an

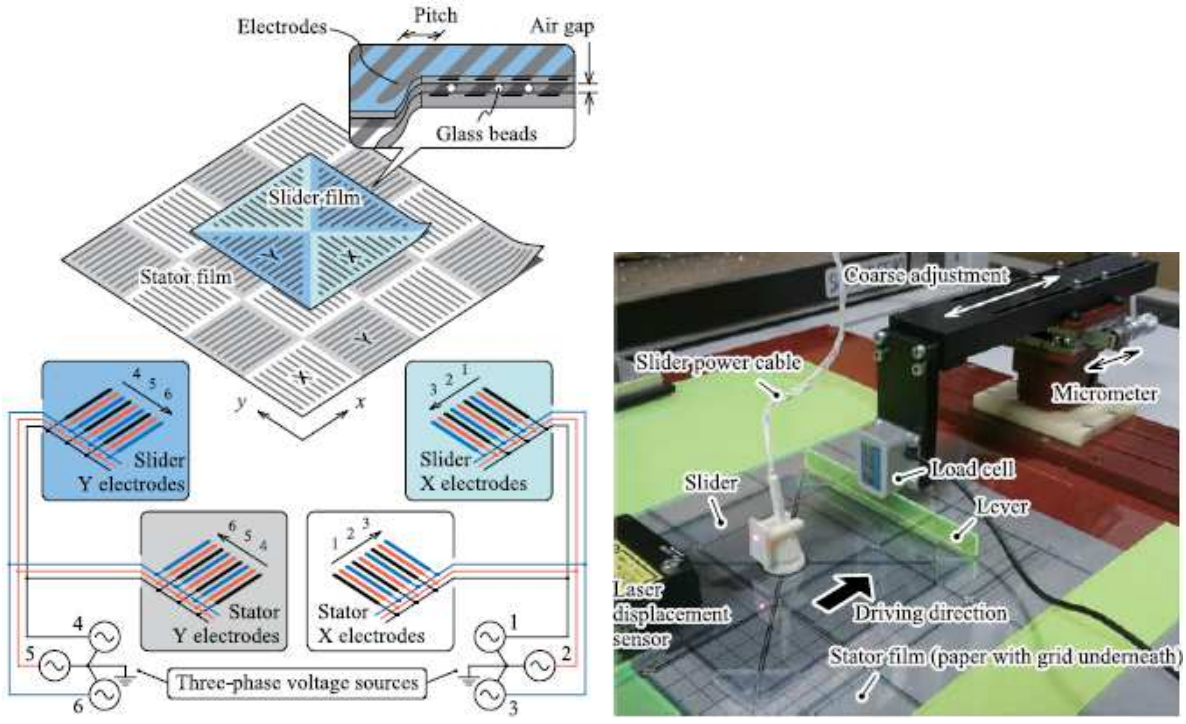

(a) **(b)**

Figure 1.18 Transparent electrostatic actuator (a) Schematic of actuator with checkerboard patterned stator and cross slider (b) Experimental set up [HOSO 2015]

electrostatic force of attraction or repulsion, respectively between them.

Based on this principle, a transparent synchronous electrostatic actuator for long stroke planar motion has been developed at University of Tokyo in Japan [HOSO 2015]. The actuator is based on a pair of transparent plastic films with strip electrodes connected in three-phase (Figure 1.18 (a)). Half of the electrodes in each film are X electrodes and the other half are Y electrodes. Three phase voltage is applied to these electrodes to excite electrostatic forces that drive the actuator at speeds proportional to the excitation frequency. The actuator has a stator part which consists of X and Y electrodes alternately arranged in a four-by-four checkerboard pattern. And a slider which is based on a square film with X and Y electrodes separated by diagonal lines. This arrangement of electrodes has been chosen for position independence of overlapping areas of electrodes which gives a uniform thrust force characteristic required for long-stroke planar motion. In the experiments, the prototype could exert approximately 100-mN thrust force with an excitation by a pair of 500-V three-phase voltages, and could travel along straight and curved paths within a 132 mm by 132 mm movable range.

1.6.4 **Electromagnetic actuation principle**

Electromagnetism is characterized by the interaction between the magnetic and electrical phenomena and is carried by the appearance of a Lorentz force exerted on an electrically charged particle in the presence of magnetic field. This electromagnetic principle is widely used to realize actuators and can be used to generate three types of electromagnetic forces.

The first type of electromagnetic force is the reluctance force. Like the electric current follows the path of least resistance in an electric circuit, the magnetic flux follows the path of least reluctance in a magnetic circuit. By analogy, the magnetic reluctance thus corresponds to the electrical resistance. When the coil of magnetic circuit is energized, a force of reluctance (1.1) appears and tends to minimize the overall reluctance of the circuit. This minimization is embodied, for example, by reducing a gap in the circuit.

$$R = \frac{F}{\Phi} \tag{1.1}$$

where

R : Reluctance (H^{-1})

Φ : Magnetic flux (Wb)

F : Magnetomotive force (AT)

Based on the reluctance actuation principle, a 2DOF planar motor for position control applications has been developed (Figure 1.19) [PAN 2011]. This guide rail based design of the planar motor provides a stroke of 100 ×180 mm^2 with the ability to withstand hostile operating conditions in industries. Small silicon-steel sheets were assembled together to form building blocks to make the stator of the planar motor. Optical encoders (resolution 1 μm)

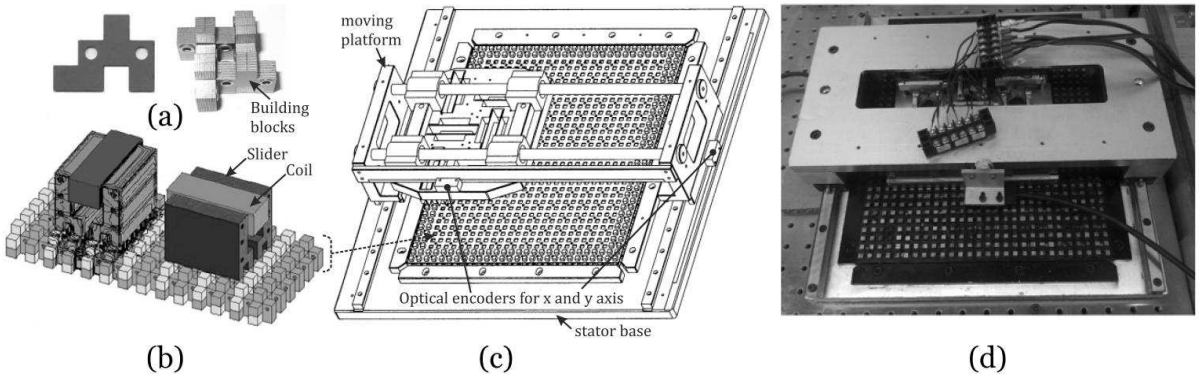

Figure 1.19 (a) Building blocks of the stator (b) Interaction principle (c) Schematics of the planar motor (d) Developed prototype [PAN 2011]

were integrated to measure the planar displacement.

The second type of force used is the induction force described by the Faraday Law (1.2). In an electromagnetic system, an induced current occurs in a coil due to a variation of the magnetic field around it. This induced current in turn creates, a magnetic field opposing the variation in flux.

$$\varepsilon = -\frac{d\Phi}{dt} \tag{1.2}$$

where

Ɛ : Electromotive force (V)

Φ : Magnetic flux (Wb)

In mechatronics field, actuators based on induction force are often used to construct multi-DOF planar motors for small object conveyance. For example, an integrated planar motor for heavy miniature component conveyance has been developed (Figure 1.20(a)) [DITT 2006]. In order to realize 3DOF motion on a copper sheet, four orthogonally arranged linear induction actuators were used. The weight of the planar motor (2.5 kg) has been compensated by using air bearings. The planar actuator is able to carry a maximum load of 21.5 N at a speed of 0.36 mm/s and is integrated with two optical sensors (resolution 63.5 µm). This approach has led to the development of a 3DOF based planar actuator (Figure 1.20(b)) [KUMA 2012]. Three Linear Induction Actuators (LIA) in delta (Δ) configuration were used. 100 magnetic steel sheets were used to realize the core of the planar actuator resulting in a 4.8 kg total mass. The planar actuator travels over a 1.5 mm copper sheet and offers a payload capacity of 60 N with

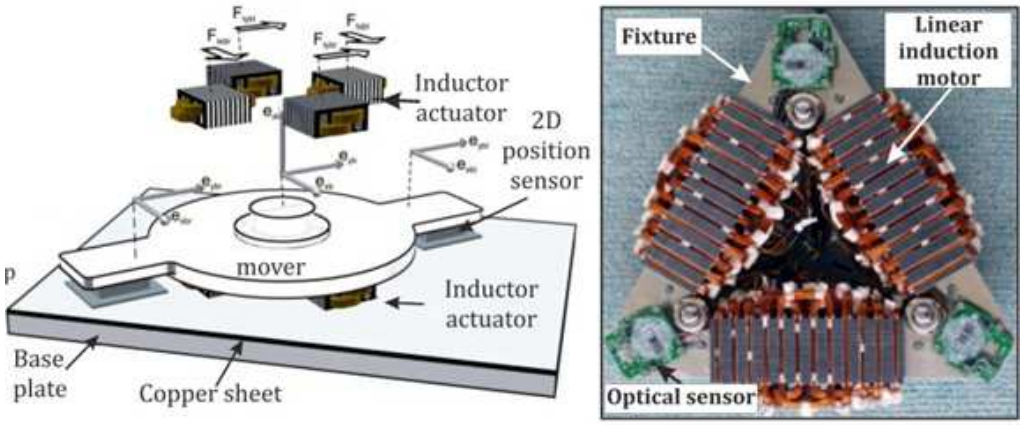

(a) **(b)**

Figure 1.20: (a) Construction of 3 DOF planar motor[DITT 2006] (b) Planar induction motor[KUMA 2012]

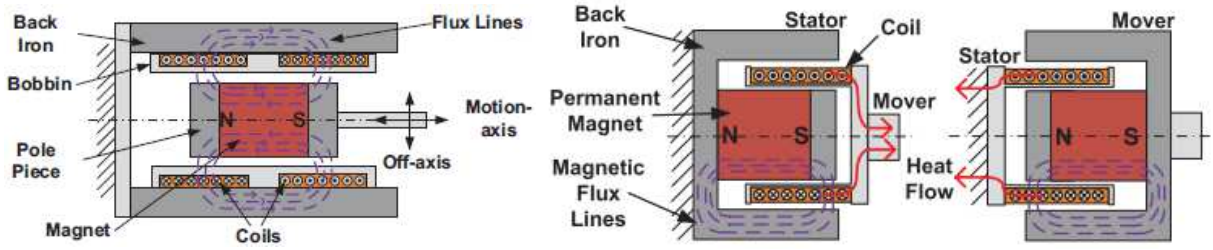

(a) **(b)**

Figure 1.21 (a) Moving Magnets Actuators (MMAs) (b) Voice Coil Actuators (VCAs)[HIEM 2014b]

a maximum 12 m/s^2 acceleration.

The third phenomenon is the Lorentz force which is based on the interaction between an electrical conductors carrying an electric current (I) and prevailing magnetic induction around the conductor (B) (1.3). In this case, a Lorentz force (F), whose direction is determined using the right hand rule or corkscrew, is applied to the conductor orthogonally thereto.

$$\vec{F} = I \times \vec{l} \wedge \vec{B} \tag{1.3}$$

where

$\vec{F}$: Lorentz Force (N)

I : current through the conductor (A)

$\vec{l}$: Length of conductor (m)

B : magnetic induction (T)

In this phenomenon, depending on the applications, different magnets and coils configurations are employed in nanopositioning stages and conveyors. Each configuration has its own advantages and drawbacks and are used as required by the application. Two different design configurations are frequenly used in electromagnetic linear actuators. One is called Moving Magnet Actuators (MMA) and the other is Voice Coil Actuators (VCA) [HIEM 2014a].

In MMAs, an axially oriented cylindrical permanent magnet is sandwitched between two iron pole pieces forms the mover (Figure 1.21 (a)). The stator consists of a back iron along the two oppositely wounded coils connected in series. The field around the permanent magnet produces Lorents force and hence, the motion. [HIEM 2014b]. MMAs are direct-drive, single-phase linear electromagnetic actuators based on Lorentz force principle. They provide frictionless and backlash-free motion over a range of several millimeters. MMAs are widely used where lack of moving wires leads to heat rejection capability or coil protection is important. They exhibit some cogging forces. They also have higher eddy current and hysterisis losses than VCAs due to changing magnetic field while the mover is in motion.

Neverthless, MMAs have several additional advantages that includes superier heat rejection and no disturbance inducing and fatiguing moving coil leads.

There are two type of VCAs, one is moving coil type and second is moving magnet type. Moving coil type VCA consists of stationary field (magnet) assembly and moving coil assembly (Figure 1.21 (b)). Moving magnet type VCAs has a reverse configuration to moving coil type. It has a coil attached to an stationary soft magnet housing which serves as a conductor and an axially magnetized permanent magnet and two soft magnetic pole pieces attached to both ends of the magnet. In moving coil type VCAs, heat dissipation from the coil and disturbance due to the moving coil degrades the motion quality. Though, moving magnet type VCAs overcome these problems, the large mass of the magnet and back iron is added to the motion stage. VCAs can achieve very high acceleration and speed with high precision and accuracy over a several millimeter range which is true for MMAs as well. VCAs are cogging free and have variation of coil force over the stroke and are hysterisis free. These attributes makes them suitable for feedback control which is important for achieving high precision.

For example, a moving coil single-moving-part planar positioner moving over a concentrated field magnet matrix has been developed [NGUY 2012; NGUY 2013]. The mobile part moves over a superimposed concentrated-field magnet matrix where permanent magnets are arranged in Halbach array layout to enhance the magnetic flux density on one side (Figure 1.22(a)). In this research work, a single moving part planar positioner with six coils was designed and implemented which moves over a concentrated field of a permanent magnets matrix. The

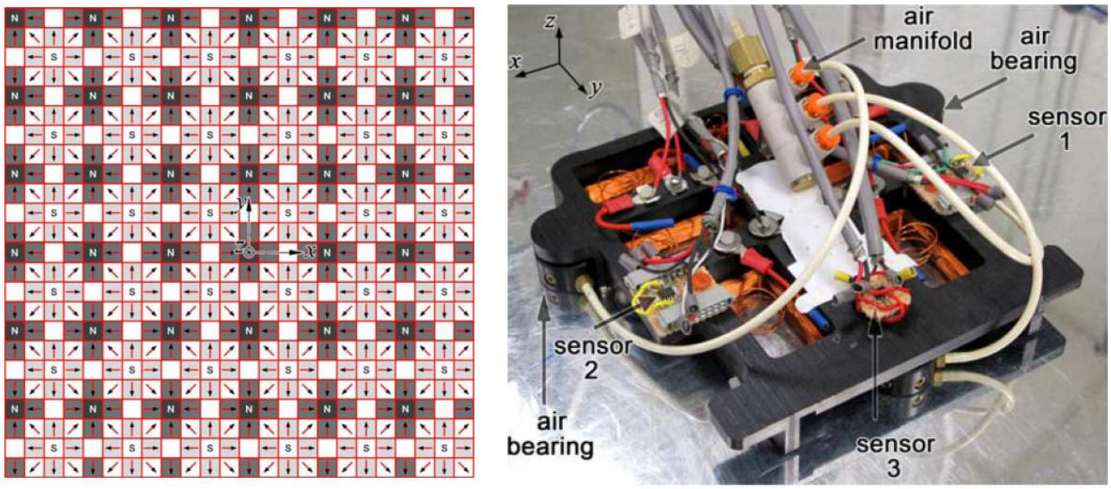

(a) **(b)**

Figure 1.22 Compact planar positioned [NGUY 2012; NGUY 2013] (a) Superimposed Concentrated field magnet matrix (b) 3 DOF planar positioner

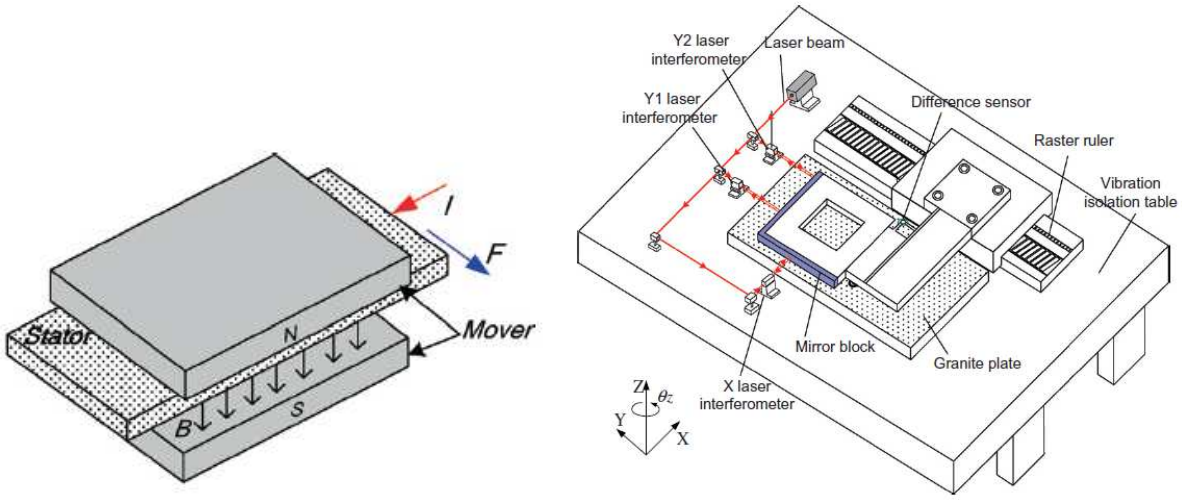

(a) (b)

Figure 1.23 (a) Working principle of Lorentz motor (b) Schematic view of the measurement system of the planar stage [LEI 2010]

moving platen carries three planar motor armatures. Closed loop control system was designed to obtain the precise performances. The travel range in x, y directions and the rotation were: 15.24 cm, 20.32 cm and 12.03° with a micrometric resolution, Figure 1.22(b) displays the constructed planar positioner. The design presented is highly applicable for stepping and scanning applications that require long-range precise translational motions in *x*- and *y*- axes and large rotations around the vertical axis.

Another example is a combination of both moving coil and moving magnet. A 3-DOF planar stage composed of three Lorentz force based motors have been developed [LEI 2010]. This device is composed of a Long Stroke Motor (LSM) which includes stationary permanent magnets and moving coils for y- axis motion and a Short Stroke Motor (SSM) which contains stationary coils and moving permanent magnets for x-axis motion. Long stroke motor is floated by two air bearings for motion along z-axis. LSM is a permanent magnet linear motor consisting of a row of permanent magnets on the stator and set of coils on the mover. The motion range of LSM is in hundreds of millimeters.

The Short Stroke Motion (SSM) consists of three independent Lorentz motors that are X, Y1 and Y2. The three motors are assembled in a H- type configuration. The working principle of each Lorentz motor is given in Figure 1.23 (a). In the design, the PM assembly is attached to the mover and coil assembly to the stator of the SSM. The stator of the SSM is connected with the mover of the LSM through a rigid driving arm. The mover of SSM is levitated by integrating two annular air-bearings with high bi-directional stiffness. The positioning platen is levitated by using rectangular air-bearings on a granite plate, and is connected with the

mover of the SSM rigidly. Therefore, the LSM and SSM are combined together in order to drive the positioning platen in the XY-plane. The schematic view of the positioning stage is shown in Figure 1.23 (b)

The three Lorentz motors are combined, so the SSM has 3-DOFs, i.e. translation along X and Y directions, and rotation about the Z axis. The maximum rotation of ±1.5 mrad about the Z axis and translation of ±1.5 mm in the X and Y directions for the positioning platen can be achieved by applying different currents in the X, Y1 and Y2 coils. The position accuracy of 15 nm has been confirmed experimentally.

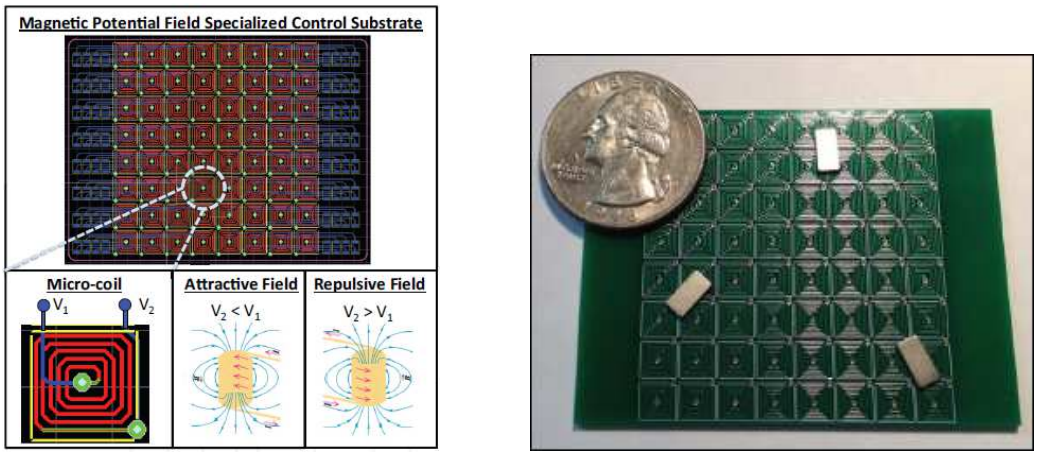

(a) (b)

Figure 1.24 (a) Design and mechanisim to control mobile microrobots (b) Printrd Cicuit board version of planar coils [CAPP 2014]

The next development is based on moving magnets actuator. An approach for independent controlling of multiple magnetic microrobots been developed [CAPP 2014]. For this, a fine grid of planar, MEMS fabricated micro coils of the same size as the microrobots (($\leq$ 500 µm) has been utilized (Figure 1.24). Real generated magnetic potentials using the coils and therefore, attractive and repulsive forces are used to control the trajectories of the microrobots. Translations for a single microrobot can be achieved by inducing a positive (repulsive) potential at the initial position of the microrobot along with an attractive (negative) potential at its goal position. This generates magnetic force vectors in the workspace of the microrobot, propelling it along a straight-line trajectory from its initial position to its goal position. The similar procedures can be followed for more complex translation trajectories when more than one robot or goal position are used. For rotations, change in the relative position of the potentials around the microrobot can be done. In this case, the positive (repulsive) potential is kept stationary under the robot while the negative (attractive) potential rotated around the

positive potential in counter-clockwise direction. It leads to counter-clockwise rotation of the micorobot. Similarly, by generating negative potential, clockwise rotation can be achieved. A microrobot is able to travel at a constant velocity of 200 mm/s along the path.

For the validation of the concept, an 8 × 8 grid of planar coils on a printed ircuit board is used for the experimentation. The experiments were mainly performed to move the magnet from one coil to another one given various different settings.

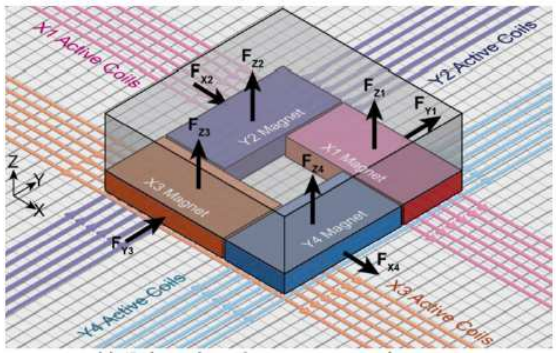

Figure 1.25 6D direct drive electromagnetic configuration [LU 2012]

In another study, 6D direct drive technology for planar motions has been developed [LU 2012]. The main advantages of this novel planar stage is that it is able to move in several millimer range and the number of coils increases linearly with the motion range. The design is composed of a stator with 3-phase planar coils fabricated on a 16 layer printed circuit board with 8 layers of X coils and 8 layers of Y coils (Figure 1.25). The overall dimensions of the PCB are 559 mm × 320 mm × 5.7 mm The mover is an assembly of four magnet arrays fixed on a mobile platen. The permanent magnets are arranged in Halbach Array configuration in order to compensate the weight of the moving platen which is 2.3 Kg. High thickness of coils (210 µm) are used to inject higher currents. The position measured with resolution of 0.5 µm in X and Y direction and 2 µm in Z direction have been achieved using external stereo vision sensor.

The Smart Surface project began in France in 2007 aims at designing a microrobotics system (an array of fully integrated micromodules that are also referred to as cells) for conveying, sorting or positioning microparts (http://smartsurface.free.fr/index.html). Each cell will contain a sensor, processing unit and actuators. There are some developments on conveyor designs based on MEMS technology that have been recognized in the past few years.

Based on this design a development has been made for a planar self-reconfigurable modular robot based on sliding blocks for conveying microparts [PIRA 2013]. In this modular conveyor design, each block embeds arrayed-MEMS actuators on its upper face. Figure 1.26 (a) represents the design of each block of the conveyor. The block is a 10 mm cube and consists of an upper and a lower part. The rotor part is composed of two cylindrical 1 mm × 1 mm neodymium magnets. The stator part consists of three Electro Permanent (EP) magnets per blocks with a size of around 2 mm in diameter and 3 mm in length. One block housing is

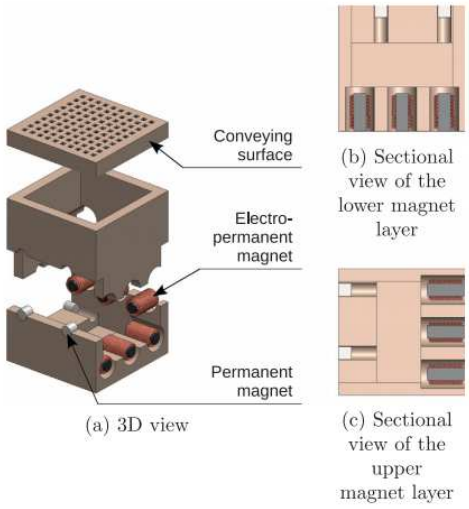

(a)

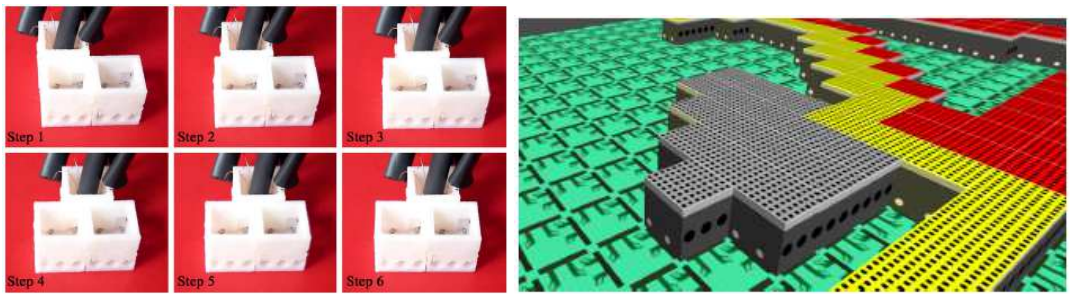

(b) **(c)**

Figure 1.26 (a) View of the linear motor units within a block with the EP and the neodymium magnets. (b) Snapshots of motion (six state sequence) (c) Captures conveyor image from the simulator software [PIRA 2013]

made by rapid prototyping with a fused deposition modeling machine. EP magnets are built using the AlNiCo core which has a diameter of 1 mm and a length of 3 mm. It has been placed in a vice and wrapped with 60 turns of 0.1 mm enameled copper wire in three layers. The final assembly has been done by placing and gluing all magnets in the lower part of the block, before gluing the upper part on it. The image from the simulator software showing blocks with conveying actuators on the top is shown in Figure 1.26 (c). The floor is covered by tracks that guide the blocks during their displacement.

A block is moved by sliding on other blocks to create an original way of moving. It needs a special reconfiguration algorithm based on a distributed algorithm which reconfigures a set of blocks according to a target map. The motion of one block for six state sequences is presented in Figure 1.26 (b). Several motion configurations were shown such as horizontal, diagonal, sinusoidal and vertical lines. The energy consumption for 10 mm move of a cube is computed around 78 mJ. The displacement speed has been evaluated by one hundred sequences and measuring the time. The mean speed was given 0.61 s for 1 cm (or 10 blocks distance in 6.1 s) which represents 16.4 mm/s.

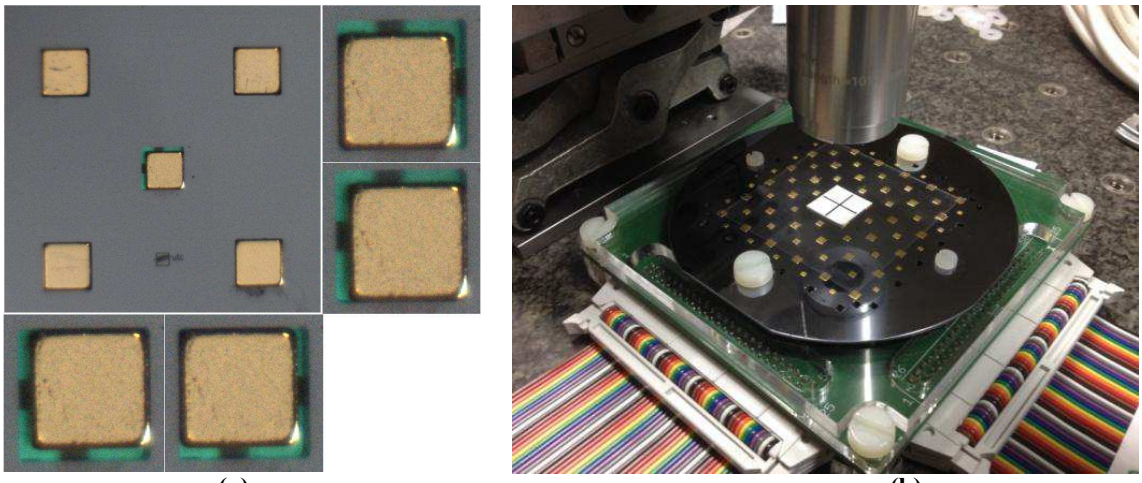

(a) (b)

Figure 1.27 (a) Elementary digital actuator with the four reachable positions. (b) Digital actuator array for planar conveyance application [SHI 2017]

A planar conveyance device based on a 5 × 5 digital electromagnetic actuator array has been developed [HUYA 2015; SHI 2017]. All actuators of the array are identical and composed of one mobile permanent magnet placed in a square cavity. The mobile magnet is able to reach four discrete positions (at the four corners of the cavity) and then to move along x and y axes (stroke 200 µm) (Figure 1.27 (a)). The switching of the mobile magnet is obtained thanks to Lorentz force with two orthogonal wires placed below the mobile magnet. Around the cavity, four fixed permanent magnets are placed in order to ensure a magnetic holding of the mobile

magnet in each discrete position. A plate (thin glass layer), placed over the array and in contact with the top side of the mobile magnets, is moved thanks to the stick-slip effect (Figure 1.27 (b)). A step-by-step movement of the plate is then obtained. Displacements of the plate in either x, y or xy direction are possible. Experimental tests have shown that the plate displacement step is several tens of microns and the displacement velocity is several mm/s.

1.7 Assessment of the different actuation principles

In previous sections, different micro-conveyance systems based on different actuation principles have been presented. From this state of art, it has been observed that pneumatic actuators are powerful devices as they deliver strong output forces where frictionless and high speed conveyance is required. These devices are mainly developed for the conveyance of delicate and clean objects such glass sheets, silicon wafers etc. Due to the complexity in the design, it is difficult to fabricate scaled down versions of the pneumatic actuators. Though, they offer large motion strokes but the displacement resolution is poor (~10 μm).

Thermal actuators operate at lower voltages than electrostatic actuators (5−10V vs. 50−100 V), but they consume more power [SHAY 2008]. With this kind of actuators, it is possible to extend the motion stroke using levers and motion amplifiers, but at the price of reduced output force. On the other hand, electrostatic actuators have very high frequency bandwidth; however the output force is relatively low as compared to other actuation principles [KARP 2008]. However, both thermal and electrostatic actuators produce small working strokes and these actuators are limited to the MEMS applications due to their temperature dependency and control difficulties.

Electromagnetic actuators present some advantages as low cost, simple design and easy to control. However, electromagnetic actuators are sensitive to their environment (electromagnetic disturbances, temperature…). These positioning stages are useful particularly for the tasks requiring nanometre level positioning precision with millimeter stroke measurement [HIEM 2014b]. These actuators also provide high operational speeds that has been demonstrated in several developments on electromagnetic actuation [CAPP 2014; LU 2012] In industrial applications, low-cost optics, large mirrors as well as large displacements are often required. These requirements can be fulfilled by magnetic micro-actuator and system (MAGMAS) due to the long range of magnetic forces [REYN 2002]. This actuation technique can easily be made compatible with existing optical electro-mechanical systems (MOEMS). Thus, advantages of silicon technology such reliability, mass

parallel-production, high frequencies, etc. can be made compatible with a simple, low-cost and reliable actuation.

To ensure high performances levels, a closed loop control is generally needed. For that, displacement sensor has to be integrated. In the following paragraph, a brief description of long stroke displacement sensors is provided. Then, the displacement sensor developed in the Roberval laboratory and used in this thesis is introduced.

1.8 Long stroke displacement sensors

Planar conveyance systems require sensing solution in order to be able to control trajectories of their mobile parts and also to be able to perform their precise positioning. In a lot of applications video camera are place above the conveyance systems. It has the advantage to be far from the workspace and then to not disturb the mobile parts. Nevertheless it has some drawbacks : either it is possible to reach high resolution but with on a poor range or the field of view is priviledged but the resolution is then poor. That is why other sensing solutions can be explored in order to ensure high resolution on long range.

1.8.1 Sensors based on different physical principles

Classical sensors which are frequently being used for precise positioning positioning are interferometers, optical encoders and magnetic encoders. Out of these, the most known method is interferometer method which gives good performances but is very expensive and their big size makes their integration into meso-machines very hard.

A laser interferometer encoder has been developed which uses two micro machined gratings [SHIN 2011]. The phase difference of 90° in the two optical signals from the two gratings comes from the 86 nm step difference between the two gratings. The study has confirmed that the resolution of the developed sensor is 1/8 of the wavelength of HeNe laser by using the quadrature signals.

On the other hand, the scale grating of linear optical encoders has been greatly reduced in size, but, clearly, further reduction is constrained by physical considerations. A double pass surface encoder for measurement of planar motions has been developed with the measurement resolution better than 5 nm [WATA 2007]. It is composed of 2D sinusoidal grid and an optical sensor for nanometer position measurement in the XY plane.

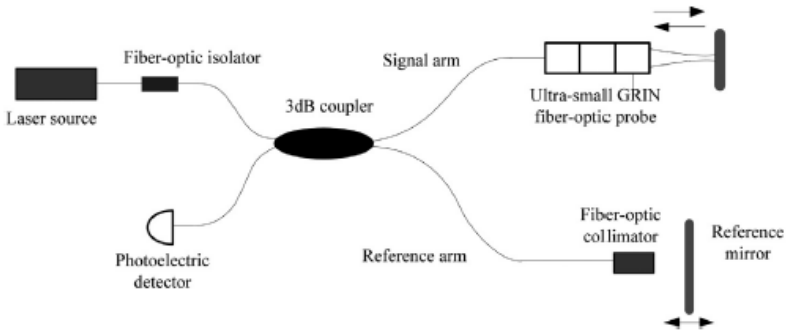

Figure 1.28 Model of integrated fiber-optic interferometer [WANG 2016]

Further, CMOS technology is also used to integrate optical metrology (photodiode, analog and digital circuits) on a single chip [FOUR 2004]. The dimension of the packaging is smaller than 10mm×10mm×30 mm. This prototype is a high resolution micro-optical encoder using sub-micron period gratings. The period of the measurement grating is 1µm whereas the period of the reading grating is 0.5µm. The interfered beams are detected and processed by the optoASIC2 reported on a CMS circuitry card. The result is an interferometric linear encoder principle using diffraction grating in reflection. Magnetic encoders have also been increasingly applied due to their ability to withstand harsh environment. However, these measuring systems have low resolutions as compared to optical encoders. For these sensors, the nanometric resolution is obtained after interpolation.

Over the past decades, Fiber Optic Sensors (FOSs) are being increasingly applied because they offer many advantages compared with other sensors such as resolution of a few nanometers, small size, low cost and light weight. Despite of being used in many domains such as robotics, biomedical etc., the measurement range of fiber optic sensor is generally very small in the range of few micrometres. Recently, one such development has been seen which is based on an integrated fiber-optic interferometer model for its application in micro-displacement measurement [WANG 2016]. The model based on the ultra small GRIN fiber probe has been investigated for the micro-displacement and has been verified its feasibility experimentally for the measurement (Figure 1.28). The results have shown the linear displacement measurement of 10 µm, linearity error 1.36% and the sensitivity is 8 mV/µm.

A long-range and high resolution displacement sensor has been developed at Roberval Laboratory at Université de Technologie de Compiegne (UTC) [PREL 2006]. This measurement technique lies between interferometer and encoder measurement technologies. Indeed, the measurement system provides continuous signals which can be used to determine

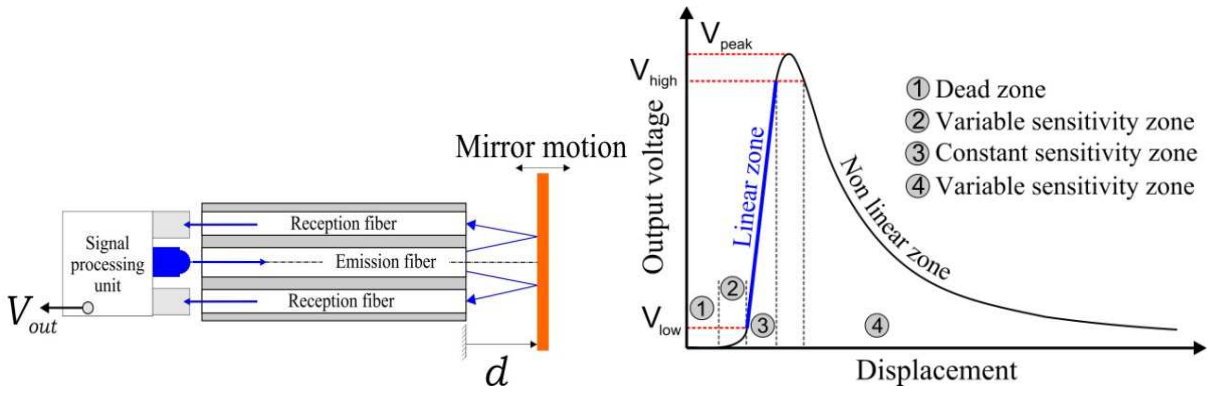

(a) (b)

Figure 1.30 Fiber Optic Sensor (a) Fiber Optic Probe (b) Sensitivity calibration curve

the displacement of the mobile part as interferometers however; these signals are also periodic and can be used as encoders.

Each fiber optic probe is composed of one emission fiber at the center and several reception fibers placed around, collecting the light reflected by the flat mirror. The light collected by the reception fibers depends on the mirror position (d) (Figure 1.29 (a)). The sensitivity calibration curve is shown in Figure 1.29 (b) and is obtained by moving the flat mirror in the direction aligned with the probe mechanical axis. In this measurement curve, the linear zone is the most interesting part because of its high and constant sensitivity. However, the range of this zone is very small (≈100 - 200 µm) and in order to increase the range while keeping a high resolution, tilted mirror configuration has been proposed and a grating composed of repeated tilted mirrors can be used (Figure 1.30 (a)) [PREL 2006]. In this configuration, the displacement direction is not orthogonal to the sensor axis; the range of the linear zone is then increased. Initial prototype consisted of two fiber optic probes and a gold coated grating microfabricated in silicon material (Figure 1.30 (b)) [KHIA 2010]. Each fiber optic probe

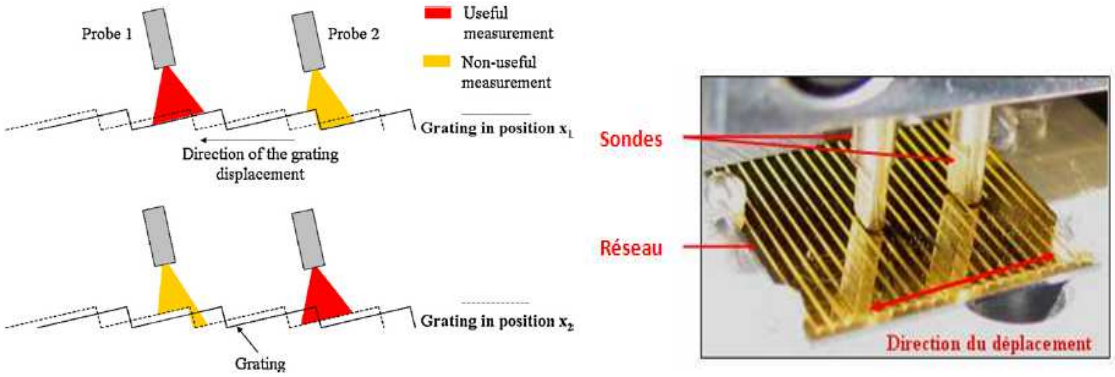

(a) (b)

Figure 1.29 Fiber Optic Displacement Sensor (a) Working principle (b) Initial prototype

consists of one emission fiber and six reception fibers. The diameter of each probe is 1 mm. The sensor is able to measure displacement with 14.9 nm resolution over 11.8 mm range with the tilted mirror configuration. With this kind of grating, two probes are necessary because when one probe is at the crossing edge of two teeth it gives non useful measurement but the other one gives useful measurement [PREL 2006]. With two probes, either of the two probes always gives a valid measurement. This ensures the continuous displacement measurement without interruption. When the grating moves, only the linear signals of the two probes are taken into account and hence, the alternate signals coming from each probe are utilized in order to compute total displacement measurement.

There are several ways of improving the performance of the measurement systems. One way improving a fiber optic sensor has been done by increasing the number of reception fibers and on low noise electronics have been reported [PERR 2011]. 16 reception fibers were used around one emission fiber. On this set up, a sub-nanometric resolution an a 400 ms integration time and a long term drift as low as 40 nmh^{-1} has been acheived. The set up has been tested for high speed applications by increasing the bandwidth upto 38 Khz. The limit of resolution of 28 nm peak- to-peak on a aluminized piezoactuator has been displayed.

1.9 Different techniques for signal processing of sensors

Nevertheless, the quality of the measurement also depends on the quality of the signal processing algorithm which is used to treat the signals in order to obtain high precision measurement. Many approaches based on signal processing techniques have been proposed to improve the performances of some measuring systems.

The reduction in pich of the scale grating in linear optical encoders is greatly constrained by physical considerations. An optical resolution of one micrometer can be currently achievable. Interpolation using soft techniques provides an interesting possibility to further improve on the encoder resolution, by processing the analog encoder signals online to derive the small intermediate positions. An interpolation method in order to increase the measurement resolution obtainable from quadrature encoder signals has been done by calculating the high order values in Look Up Tables in advance and based on that, they have provided neural network approach [TAN 2005] with two radial basis function stages (RBF). The first stage is to correct the imperfect signals, and the second one works as an inference machine to interpolate the quadrature pulses. The proposed approach improves the tracking performance of the controller, with fast speed. There are advantages associated with this approach when

compared to the look-up table approach, in the use of storagememory and execution speed. Under the proposed approach, it is only necessary to reserve memory space for storing the parameters of the RBF networks.

Another approach has been proposed to correct signals and generate high-resolution quadrature pulses for magnetic encoders. It consists of two parts: one is called the Advanced Adaptive Digital Phase-Locked Loop (AADPLL) which compensates the noise in the encoder signal and the second is the pulse interpolator which generates high resolution quadrature pulses [HOAN 2011, HOAN 2007]. This method is able to remove the time lag caused by low pass filters, changing the cutoff frequency of the applied filters and adjusting the AADPLL parameters to suitable values in real time as well. Four input frequencies were tested: 0.5, 100, 400, and 900 Hz, corresponding to the linear motorspeeds: 0.5, 100, 400, and 900 mm/s. It has been concluded that the AADPLL can track the signals in both very low and high frequency domains. The second scheme employed in the pulse generator has the ability to increase the resolution for the encoders, which is represented by the interpolation factor N (N = 8n, where n is the order of the high-order sinusoids extracted from the original encoder signals). Moreover, although the encoder signals become rough during the change of direction of rotation, the AADPLL still provides a good tracking performance in this situation.

For precise and robust position estimation for optical incremental encoders, a converter with linearized technique has been proposed [YE 2015]. In this approach, the sinusoidal signals are converted into perfectly linear output signal, from which displacement can be determined precisely using a simple linear equation. The implementation of the converter with FPGA has shown successful results with very low positiong error on an optical encoder.

For a 6 DOF planar actuators, a look-up table based real-time commutation of the actuator has been proposed [BOEI 2009]. A feedback linearization law has been applied for decoupling of forces and torques. It is based on the coupling matrix that links the current in each coil to the force and toque vector on the actuator. A look-up table based method has been used to apply feedback linearization and verified with measurements. It is able to realize the desired forces and torques within an accuracy of 97%.

1.10 Conclusion

In this chapter, a state of art on the microfactory concept and then on the micro-conveyance systems has been presented. At first, the definition of the micro-factory has been given and the associated characteristics, as reconfigurability, flexibility, etc. of a microfactory have been described. The different components of a micro-factory have then been presented and it has been highlighted that the conveyance system represents an important component because it should be able to be quickly adapted and reconfigured according to the modifications of the product flow. For that, conveyance surfaces based on elementary modules, which can be independently controlled, are well adapted. This architecture can indeed be simply reconfigured without the need of manual intervention. Only a software modification, acting on the control of the surface, is indeed needed to change the trajectories of the conveyed products.

After the section on the microfactory concept, the state of art has been focused on micro-conveyance systems. In this second section, conveyance systems based on different actuation principles have then been presented and described. The architectures and performances of these systems have also been given. Then, a brief assessment of the actuation principles has been realized.

In the present thesis, a micro-conveyance system has then been studied. Based on the state of art, a matrix architecture composed of independent elementary cells has been selected for the proposed system. Moreover, based on these advantages and on the experience of the Roberval laboratory on the development of electromagnetic actuators, the electromagnetic principle has been selected. The originality of the proposed work lies in the proposed design which is able to ensure the displacement and the guidance of the mobile part. The design limits also the energy consumption and the Joule heating to generate long displacement.

In this thesis, the principle and the proposed design of the system are firstly described and the originalities are highlighted. Then, a modeling is presented and used to size a prototype which has been manufactured. Experimentally characterization of the system is then provided. Moreover, a part of the thesis deals with the realization of an algorithm for a long-range displacement sensor used to measure the mobile part displacement.

The thesis is divided into five chapters. The second chapter describes the principle and the concept of the proposed micro-conveyor system. The third chapter is focused on the modeling and on the sizing the proposed system. The fourth chapter presents the experimental tests and

the characterization of the prototype. The fifth chapter describes the proposed algorithm to ensure the mobile part displacement measurement on long strokes. Finally, a conclusion of the thesis is provided and several perspectives of the work are given.

Chapter 2: Principle of Smart Electromagnetic Conveyor (SEC) platform

In this chapter, the concept of the Smart Electromagnetic Conveyor (SEC) platform based on electromagnetic actuation principle is presented. Starting with the principle of single axis linear motor, a miniature electromagnetic planar conveyor with 3 DOF using Lorentz force has been developed in the previous works at Roberval laboratory of the Université de Technologie de Compiègne [BENC 2006]. Later, improvement and optimization of the planar conveyor has been done and a new 3 DOF electromagnetic Micro Positioning Stage (MPS) for few millimeter stroke motions that allows planar motions and rotation around the centre of the mobile part has been developed [KHAN 2014]. In this work, a SEC platform, based on the MPS system, is proposed for centimeter stroke motions of the mobile part on the whole platform surface. The design of the platform is based on a matrix coil design configuration. Each cell of the matrix is composed of 2D coils that allow planar motions along the two axes and rotations around the centre of the mobile part.

At first, functioning of two layer coil design of the SEC platform has to be tested and validated. In order to do that, a 2D planar electromagnetic actuator composed of two layer coil assembly design for micro applications is developed. In the design, the stator part is one cell of the matrix design and the mover is developed by assembling PMAs. The design and working principle of 2D actuator is described in further sections. After validating the functioning of the 2D actuator design, the whole matrix design of the SEC platform is realized. In the design the displacement between the two cells of the matrix is tested. The general working concept of the SEC platform along with the general layout of the platform is presented. The idea of this work is to develop a platform that allows long displacements for the automated transportation of micro objects to the desired location within the platform. The design should be flexible enough so the mobile can perform different motion trajectories to reach the desired location by following different motion paths. And this has to be done with minimum energy consumption. Therefore, all these parameters are taken into account while designing the SEC platform.

2.1 Electromagnetic actuation principle

The electromagnetic actuation principle is based on Lorentz force law. This law states that when a Permanent Magnet (PM) is placed near a current carrying conductor, an electromagnetic force appears due to the interaction between magnetic field generated from

the PM and current carrying conductor. The resultant force appears over the PM as the current carrying conductor is fixed. The generated electromagnetic force (or Lorentz force) can be computed using equation (2.1) [Furl 2001].

$$F = I \int_{wire} dl \times B_{ext} \tag{2.1}$$

Where, F is the generated electromagnetic force, l is the length of the current carrying conductor, I is the current flowing in the wire and B_{ext} is the external magnetic field generated around the conductor by the PM. The direction of the generated electromagnetic force depends on the relative orientation of magnetic field of the PM and direction of the current

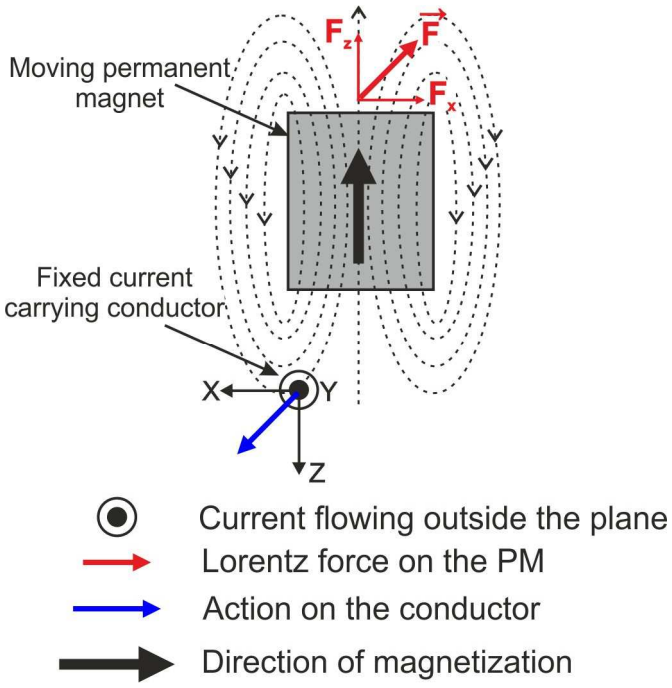

Figure 2.1 Electromagnetic actuation principle

flowing in the conductor (Figure 2.1). The resultant force $\vec{F}$ appears on the PM due to the relative interaction between the magnetic fields from the PM and the conductor. Due to the relative position between the conductor and the PM, the electromagnetic force can be decomposed into three components. Because it is assumed that the conductor is perfectly aligned along the length of the PM as shown in Figure. 2.1 for y- axis direction, the 3D problem can be reduced to 2D in y-axis direction [KHAN 2014]. The components of the electromagnetic force F can then be mathematically written as in equation (2.2).

$$F = \begin{Bmatrix} F_x \\ F_y \\ F_z \end{Bmatrix} = \begin{Bmatrix} +I_y \cdot B_z \cdot l \\ 0 \\ -I_y \cdot B_x \cdot l \end{Bmatrix} \tag{2.2}$$

The components F_x and F_z represents the translational and vertical forces in *xz*- plane. The magnitude of these forces depends on the intensity of the magnetic flux density on the conductor, magnitude of current flowing in the conductor and length of the current carrying conductor subjected to the magnetic field.

In order to optimize the system, the abovementioned parameters are defined in order to achieve the maximum electromagnetic force. However, the design constraints play a crucial role in defining the values of these parameters and increasing the force. One way is to increase the magnitude of current in the conductors. But it is limited by the cross sectional area of the conductor. Therefore, the current can't be increased beyond certain value as the cross section of the conductor is fixed by the technology limitation. Otherwise it leads to Joule heating effect which may destroy the conductor or degrade the remanent magnetization of the PM. The second way to increase the force is to reduce the relative distance between the conductor and the PM. In this work, though this distance is not a limitation for miniaturization, it is a very important parameter in generation of electromagnetic forces. The influence of the distance in functioning of the platform is described in detail in further sections. Another way is by either increasing the number of PMs. But this option will add up to more weight and also will change the overall dimensions of the SEC platform.

2.2 Single axis Linear Motor

The working principle of a single axis Linear Motor (LM) is shown in Figure 2.2. The actuation principle presented in the previous section has been extended to realize long range linear motion actuator. For that, a Permanent Magnet Array (PMA) is used as a mobile part and Planar Electric Drive Coils (PEDCs) as a fixed part. In this work, Neodymium Iron Boron PMs with low operating temperature are used. PMs are arranged in opposite magnetic orientation called "North South (NS) array configuration" [KHAN 2012]. This arrangement has been chosen as PM assembly is very easy with this configuration. And also it offers various advantages such as symmetrical magnetic field on top and bottom sides of the PMA. This due to the opposite orientation of the magnetization and does not need any equipment for bonding and alignment. In this work, 14 PMs are used in a PMA and are placed above two fixed two phase PEDCs (see Figure 2.2 (b)). When two sinusoidal currents, I_1 and I_2, with a

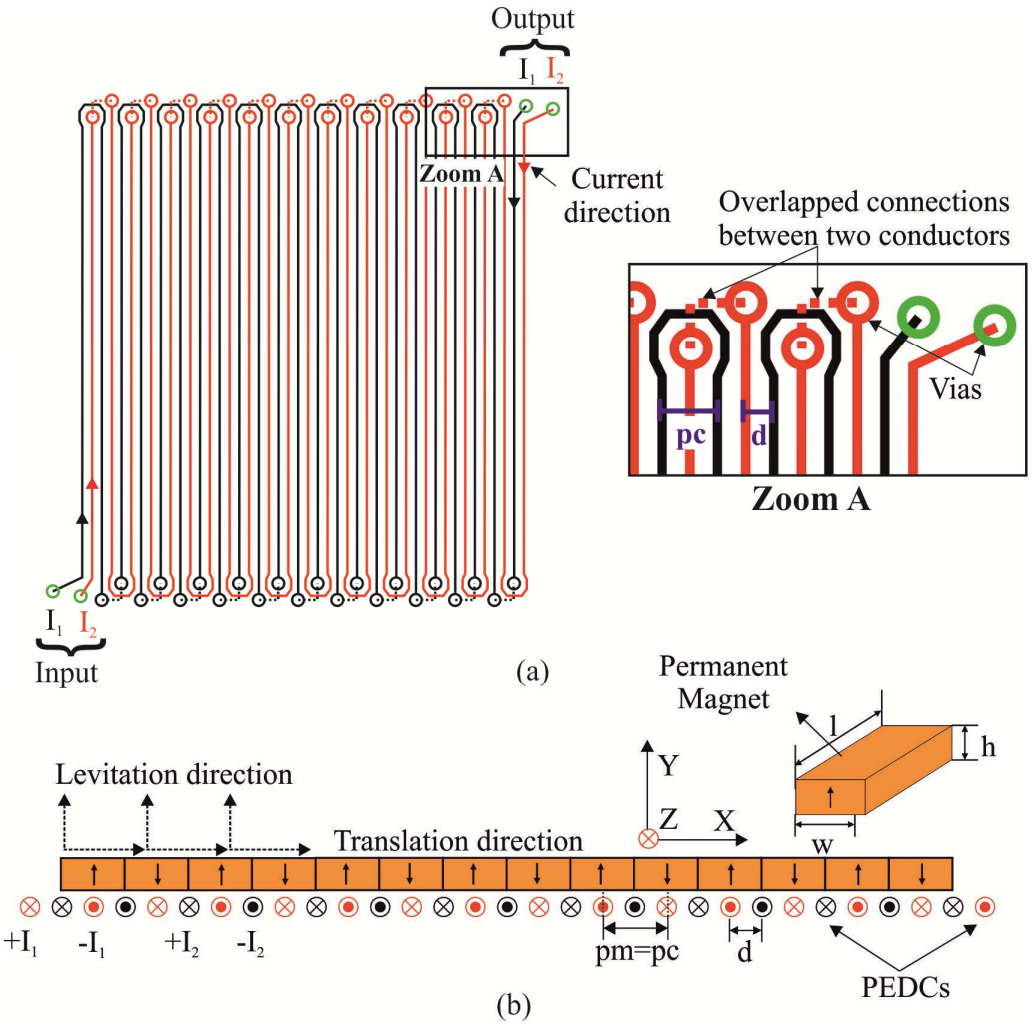

Figure 2.2 Single axis linear motor (a) coil design (b) cross sectional view of single axis LM

relative phase shift of π/2 are supplied to two fixed PEDCs placed underneath a PMA, electromagnetic force is generated due to the interaction between the magnetic field from the PMAs and the currents in the coils and hence, generates motion of the PMA.

Firstly, the PEDC design has been realized. In previous works, an overlapped planar coils formation approach has been adopted to minimize the volume of PEDCs of the LM [KHAN 2012]. The same construction coils are used in this work. The dimensions and other design parameters are considered according to the required performances (e.g. motion range, maximum input current, etc.) and PCB fabrication constraints. The PEDCs consists of two phase coils as shown in Figure 2.2 (a) where length of each conductor is 25 mm. The width and height of the PEDC are 250 µm and 35 µm respectively. The pitch of the coil, 'pc' is 1 mm and the distance 'd' between the two PEDCs is 0.5 mm. The above dimensions and parameters are selected depending on the design (e.g. motion range, maximum input current, etc.) and PCB fabrication constraints. Vias (through holes) are fabricated for the overlapped connections between the conductors for a single phase coil and for the connections with the external source Figure 2.2 (a).

The working principle of the LM to perform long range continuous motion is presented in Figure 2.2 (b). A PMA with 14 PMs is placed above the two fixed PEDCs. Each PM has the following dimensions: length, l= 6 mm, height, h= 1 mm and width, w= 1 mm. The currents injected in the PEDC, called "I_1" and "I_2" are expressed as in equation (2.3).

$$\begin{aligned} I_1 &= I_{max}\sin(\omega t) \\ I_2 &= I_{max}\sin(\omega t + \pi/2) \end{aligned} \tag{2.3}$$

Where, "I_{max}" and "ω" is the maximum amplitude (A) and the angular frequency (rad/s) of the injected current, respectively.

The coil pitch 'pc' and period of the PMA 'pm' have to be equal in order to obtain long range continuous motion. This condition is necessary to ensure the alignment of the peak current amplitude with the peak magnetic flux density generated by the PMA. The interaction between the current and magnetic field results in the generation of Lorentz forces along the same direction [KHAN 2014].

2.3 3 DOF Micro Positioning Stage (MPS)

In the previous works, a 3 DOF *xy* positioning stage based on the working principle of the single axis LM has been developed [KHAN 2014]. It is capable of performing planar

displacements on a few millimeters stroke and a rotation along the axis perpendicular to the plane.

The MPS is based on an orthogonal arrangement of four LMs. Each LM consists of a PMA composed of 14 PMs placed above a pair of fixed PEDCs. Also, a glass layer of thickness 130 µm has been placed on the top side of the PCB for the insulation between the fixed part and the mobile part. It helps in reducing friction and ensures smooth motion. The layout of the electromagnetic Micro Positioning Stage (MPS) is shown in Figure 2.3.

A microfabrication technique is used for the fabrication of mobile part i.e. a cross shaped pallet on silicon material because low fabrication tolerances are required to ensure perpendicularity of axes and precise positioning of each PMA. And the fixed part is based on

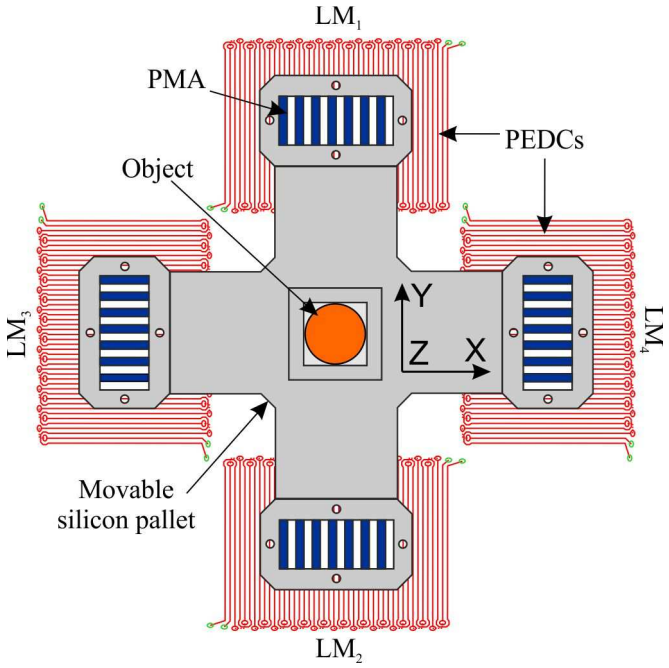

Figure 2.3 Layout of 3 DOF electromagnetic micro positioning system

the Cu coils which have been fabricated on double sided PCB. The top side of the PCB is used to fabricate the coils and the bottom side is used for the connections with the external power source. In the MPS system, only two LMs are required to be activated at a time in order to perform motion of the pallet along one displacement axis. LM_1 and LM_2 ensure motion of the pallet along *x*-axis while LM_3 and LM_4 move the pallet along *y*- axis (Figure 2.3). That means, the total electromagnetic generated force along *x*- axis (y-axis) is the sum of the forces generated by LM_1 and LM_2 (LM_3 and LM_4).

Different motion capabilities of the MPS system are presented in Figure 2.4. Thanks to its layout, MPS system is not only able to perform motions along *x*- and *y*- axes, planar motions

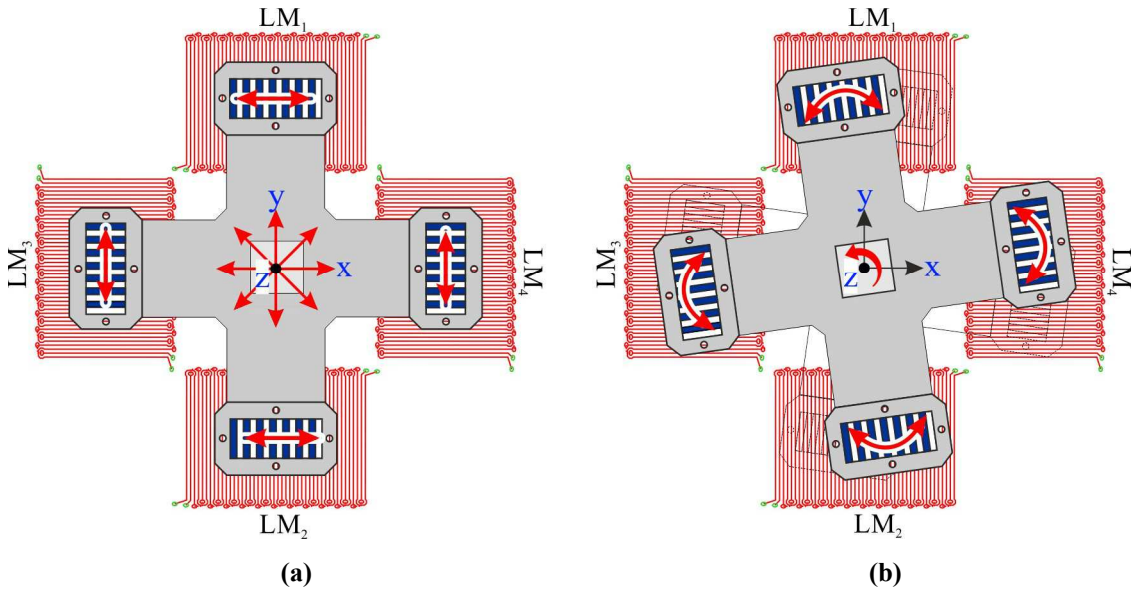

Figure 2.4 Different motion directions of the MPS system (a) Planar motions (b) Rotation about the center

along *xy*- axis by injecting currents in all the four LMs at the same time (see Figure 2.4 (a)). Moreover, the displacements can be performed with different angles by changing the frequency of signals in each axis for *xy* motion. Also, rotations have been demonstrated. It has been done by inversing the directions of the current in the two LMs situated along the same axis with respect to each other. It produces a torque about the centre of the mobile part and thus, generates rotation along the axis perpendicular to the plane. However, the torque is limited due to the design constraints of the MPS system. Also, by differentiating pulsations in each axis, it can be moved with any angle in *xy* direction. Maximum $\pm 11°$ of rotation have been reported in the MPS system [KHAN 2014].

Furthermore, the MPS system provides a guidance function which helps in reducing the straightness error during motion along an axis. The guidance function can be used by injecting constant currents into the LMs situated perpendicular to the motion axis. This has been done to reduce straightness error during motion which can occur due to geometrical and dimensional errors of PMs or PMA assembly errors that can lead to variation in magnitude of the forces along an axis.

Overall, the developed MPS system ensures light weight and simple design for millimeter stroke actuation which are limited due to the design constraints. In this new work, the concept of the MPS system is further extended to perform long stroke displacements. In order to do that, the area of fixed part needs to be enlarged to perform long stroke motions of the silicon pallet.

2.4 Smart Electromagnetic Conveyor (SEC) platform

In this section, the context of the SEC platform is described. Then, the design and working principle of the SEC platform is presented. Based on the SEC platform, the design and principle of 2D actuator is then presented. In the end, an application of the SEC platform is presented.

2.4.1 Context

The objective of the presented work is to develop a long stroke planar displacement conveyor platform. The only way to enlarge the coils area without changing the cross structure dimensions is to superimpose the coils to generate the displacement in each direction. Two possible configurations for the conveyor design are proposed (see Figure 2.5). The first configuration is based on a mesh of 2D overlapped coils where the lengths of the PEDCs are increased. In this configuration, the stroke can be increased relative to the length of PEDCs as shown in Figure 2.5 (a). This architecture ensures long stroke motions of the pallet along x- and y- axis but has some main drawbacks. The first one is that several platforms can be simultaneously controlled but not independently because of identical controlling currents for the whole surface. Secondly, energy consumption will be highly increased compared to the previous studies because the whole surface has to be energized in order to perform motions. In this case, the electrical resistance will then be high and so the Joule heating effect. Also, if one of the PEDCs is damaged or deteriorated, the whole conveyor platform stops functioning and

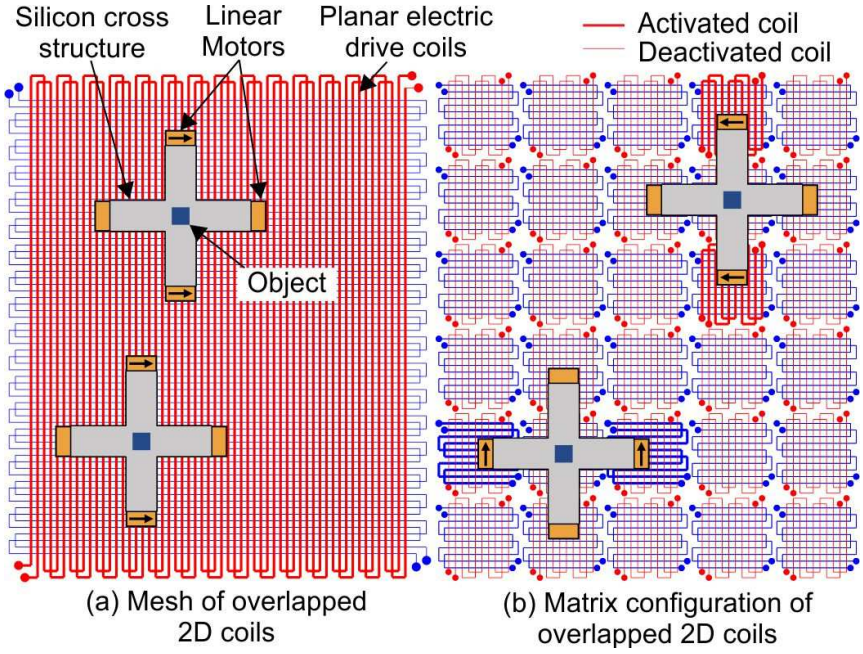

Figure 2.5 Two proposed SEC design configurations

need to be replaced. Rotations are also not possible with this design configuration. To overcome these drawbacks, a second approach based on smart surface composed of several similar cells arranged in matrix architecture is proposed (Figure 2.5 (b)). In this approach, the design is based on square matrix where each elementary cell is made of overlapped 2D coils. Square matrix design is chosen in order to achieve same motion stroke in the two directions.

The main advantage of this matrix based design is that instead of energizing the whole SEC surface, only the PEDCs which are beneath PMAs on the pallet will be supplied to perform motions. Therefore, each elementary cell of the matrix has to be managed and controlled independently by locally activating the PEDCs in the neighborhood of the mobile silicon pallet. This strongly reduces the electrical resistance of the activated coils (as only few coils are activated) and thus, energy consumption is low especially over large surfaces. In this way, one or many pallets can be displaced and controlled at the same time. Moreover if one cell is damaged, the other cells are not affected and the smart surface is still working. The pallet can change the trajectory to avoid the damaged cell and still the operation will not stop. But, this will be the degraded mode of operation because the entire surface will not accessible. In addition, rotations are possible on the matrix design architecture of the SEC platform.

2.4.2 **Design and principle of the SEC platform**

In this work, the fixed part of the SEC platform conveyor is designed and developed according to the size and dimensions of the movable silicon cross structure pallet developed in the MPS system. A 5 × 5 matrix design prototype of the SEC platform is presented in Figure 2.6. The PEDCs of each elementary cell of the matrix for the translation along *x*- axis are situated in Layer 1 of the platform. Similarly, the PEDCs for *y*- axis translation are placed in Layer 2 of the SEC platform. Each cell of the square matrix design is 25 mm × 25 mm in dimensions.

The working principle of the SEC platform is shown in Figure 2.7. Alike the MPS system, for displacement of the cross structure pallet in one cell along an axis, only two opposite LMs are required to be activated. LM_1 and LM_2 in Layer 1 for x- axis motion (Fig. 2.7 (a)) and LM_3 and LM_4 in Layer 2 are energized for the motion along y- axis (Fig. 2.7 (b). All the four LMs need to be energized in order to perform whatever motions in the plane (x,y) (see Figure 2.7 (c)).

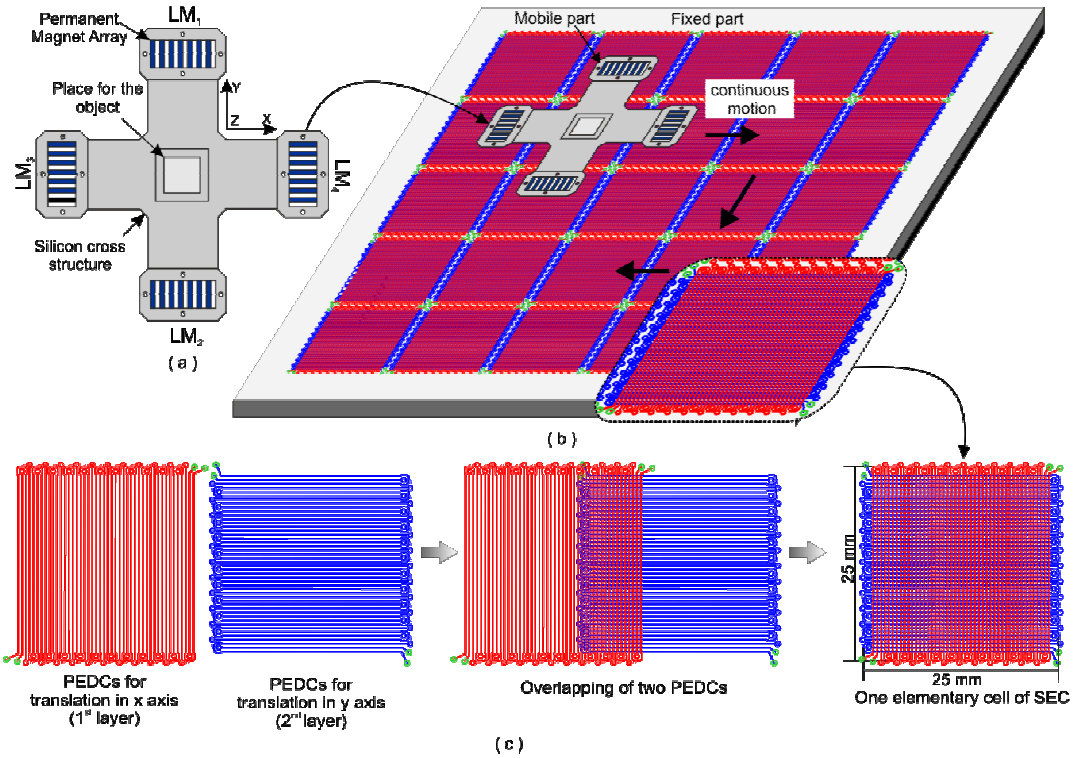

Figure 2.6 Matrix design of the SEC platform (a) Silicon cross structure (b) SEC matrix architecture (c) one cell of the matrix design composed of 2D overlapped coils

In order to perform long displacements such as translation from one cell of the matrix to the next one, the two cells adjacent to the cell where LM_1 and LM_2 are, are also be supplied for x-axis motion (see Figure 2.8 (a). In the same way, the two cells adjacent to LM_3 and LM_4 are supplied for y- axis motion (see Figure 2.8 (b)). This shows that for a given position of the mobile part, only specific cells of the matrix are required to be activated in order to generate motion while the remaining cells are deactivated.

Furthermore, the proposed SEC platform design is also adapted to the guidance function. SEC

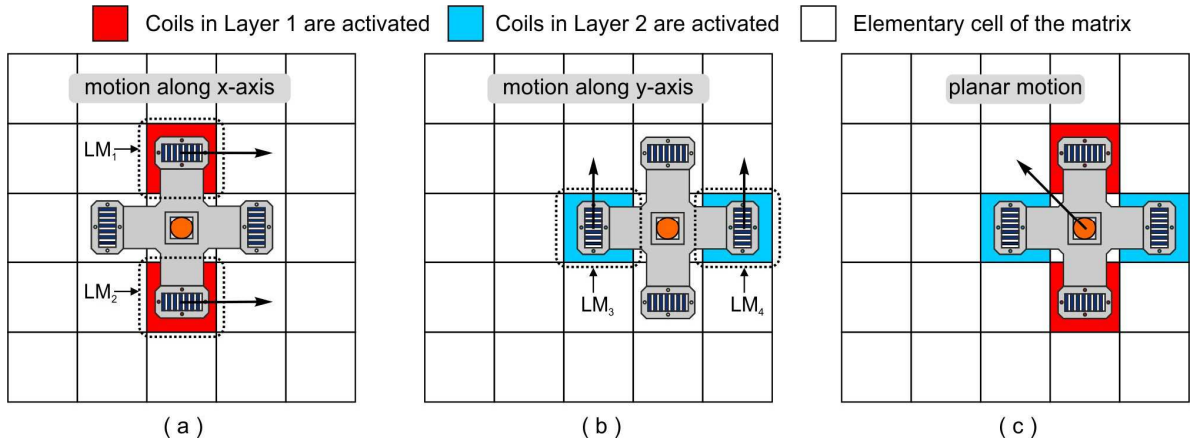

Figure 2.7 Working of SEC platform (a) motion along x- axis (b) motion along y- axis (c) motion along xy-axis

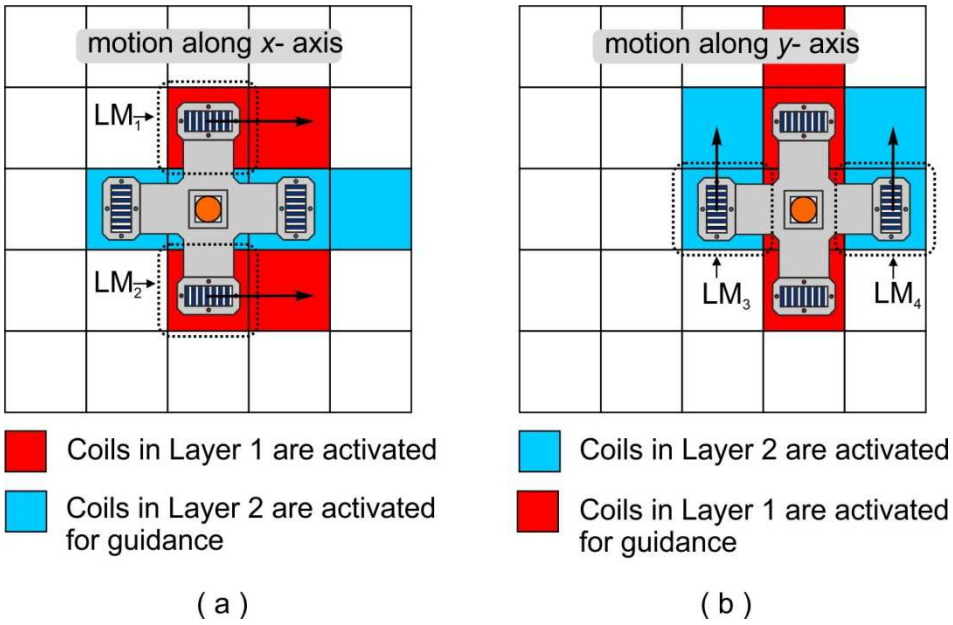

Figure 2.8 Guidance function (a) along x- axis (b) along y- axis

matrix design configuration provides a guidance that helps in reducing the straightness error during motion by providing guidance to the moving pallet. This function is necessary when moving along *x*- and *y*- axes. For the combined motion along *xy*- axis, it is directly integrated. Alike MPS system, the drift in the motion straightness occurs during the motions along *x*- and *y*- axes where two opposite LMs are used. Although same currents are injected into the two LMs, the generated forces are not always identical. Due to dimensional tolerances of the PMs or assembly errors may lead to changes in the magnitude of forces along an axis. It causes drift in motion straightness. To overcome this issue, the guidance funcstion can be used by supplying constant currents to the LMs perpendicular to the motion axis. The constant currents are injected into two opposite LMs in Layer 2, LM_3 and LM_4 (i.e., guidance along *y*-axis) during motion along *x*- axis (Figure 2.8 (a)). Similarly, guidance function can be used in *x*- axis by supplying constant currents to the LMs, LM_1 and LM_2 in Layer 1 while actuation along *y*- axis (Figure 2.8 (b)). It improves the motion characteristics by aligning the mobile pallet relative to the PEDCs during motion.

2.4.3 **2D actuator design and principle**

Before testing and validating the principle of the whole SEC platform, the functioning of one cell of the matrix has been tested. To do that, a mover, which regroups orthogonally oriented PMAs, has been placed above one elementary cell of the matrix. The design layout of the mover and stator of the 2D actuator is presented in Figure 2.9. The cross sectional view of the planar actuator is presented in Figure 2.9 (b). Six PMs are used to generate the Lorentz force

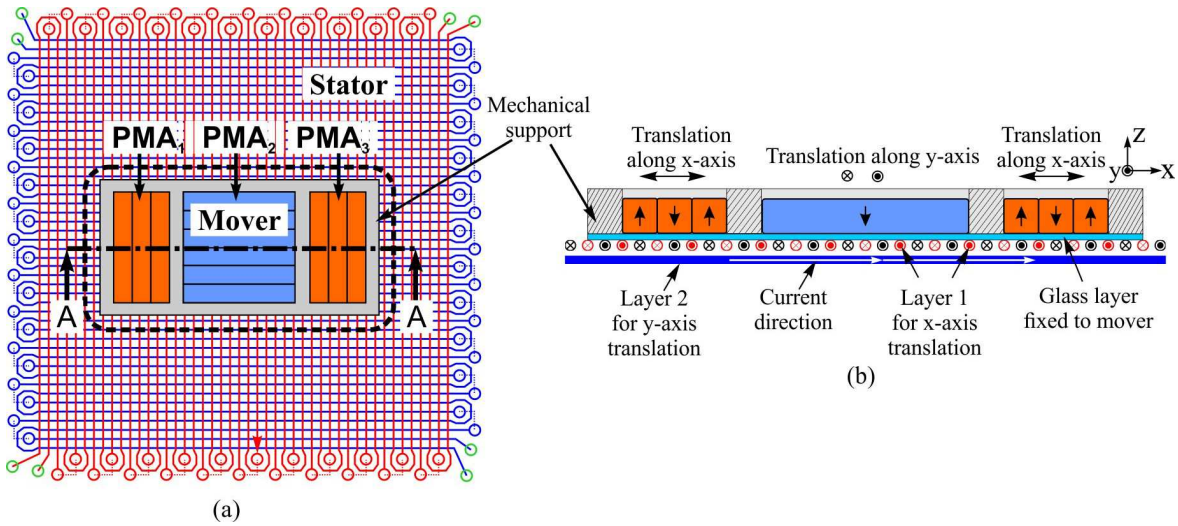

Figure 2.9 2D electromagnetic actuator based on two layer coil assembly (a) 2D actuator design (c) cross sectional view of the actuator

along each displacement axis. For x-axis motion, the six PMs are distributed equally between PMA1 and PMA2; each consisting of three PMs (see Figure 2.9 (a). PMA1 and PMA3 are located at the extremities of the mechanical support and are arranged in the same orientation. Along *y*-axis, a single PMA composed of six PMs to form PMA_2 is used and placed at the center of the mover. It is arranged orthogonally with respect to the other two PMAs. This distributed configuration ensures the same number of PMs along both the axes and provides symmetrical architecture for the mover. This design is adapted in order to achieve symmetrical motion behavior during functioning of the actuator.

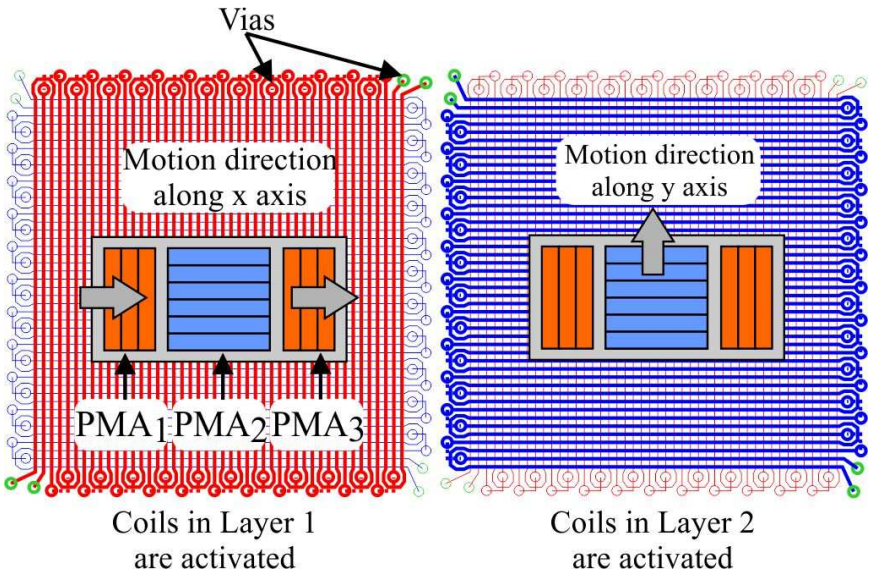

Figure 2.10 Working principle of 2D actuator

To perform a linear motion along one axis, a pair of PEDCs in one of the two layers (according to the desired displacement axes; *x*- or *y*- axis) should be supplied (Figure 2.10). When the pair of PEDCs of Layer 1 is supplied, the PMA_1 and PMA_3 ensure the mover displacement along *x*- axis. Similarly, when currents are injected in PEDCs of Layer 2, the PMA_2 moves the structure along *y*- axis. In this way, planar motions can be achieved by injecting currents to the PEDCs in both the layers at the same time.

2.5 Application of the smart surface

In this work, the proposed SEC platform can be used to realize a conveyance device especially in the context of micro factory where reconfigurablity, flexibility, low energy consumption are the strong requirements. The concept and design of the SEC platform is well adapted to these requirements. The conveyance system presented is composed of several elements in terms of physical parts such as mobile pallets, elementary cells and in terms of organization i.e. manufacturing tasks in order to manage complex trajectories. Also high performances (robustness to cell failures, minimization of energy consumption, prevention of pallets collisions etc.) are needed. To achieve this, a specific information and organization system is required to access the micro scale requirements of the micro world [Magali 2014]. Specifically the conveyors used for the transportation of micro objects within the microfactory

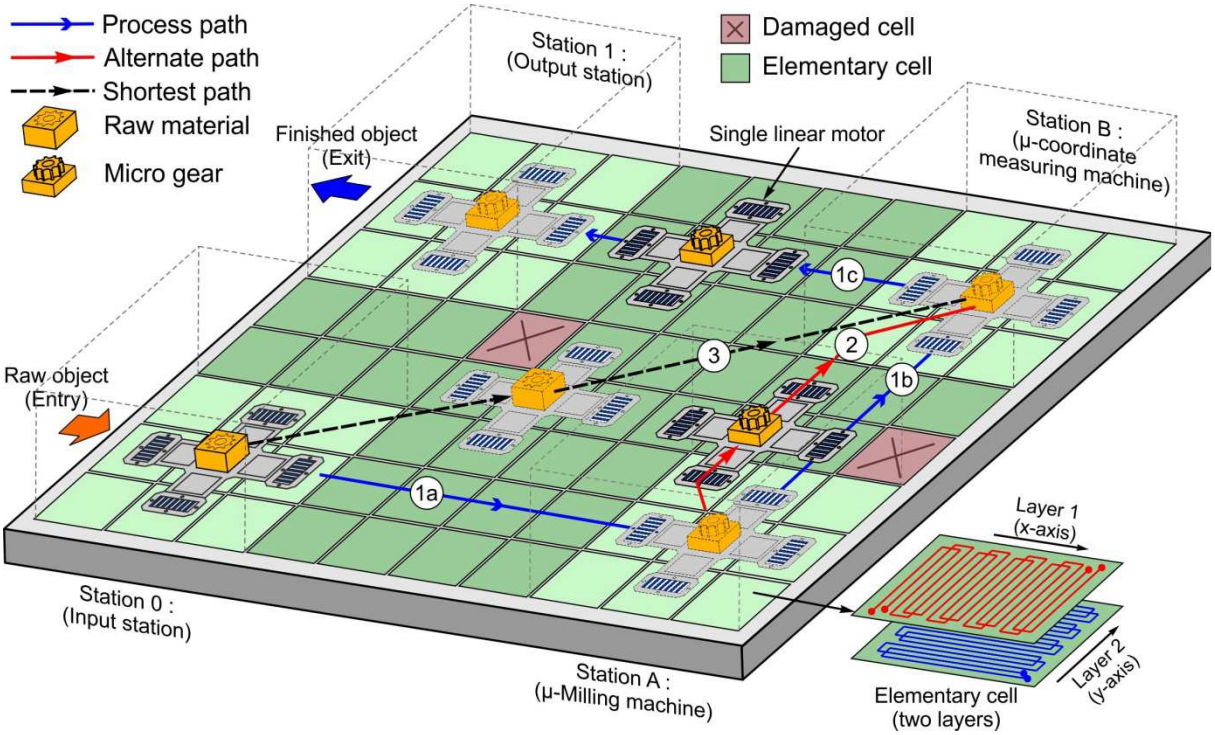

Figure 2.11 Working concept of Smart Electromagnetic Conveyor platform

require control and management to acquire specific characteristics adapted to the micro scale requirements.

A theoretical example of manufacturing a gear is shown in Figure 2.11. One pallet is shown that follows a particular process path for various manufacturing tasks. So the conveyance device presented has one pallet that transports the raw object from the start to end in order to achieve the final product by passing through various manufacturing stations on the surface. In order to do that the pallet has to change its trajectories to follow the process path. This is shown to illustrate if several pallets are moving at the same time, the SEC platform is able to manage the paths of each pallet in order to avoid collisions between them.

Station 0 is the input station of the raw object and Station 1 is the output station of the finished product. At start, a block of raw material is placed on the mobile pallet which takes path (1a) to reach Station A for micro-milling machine task. Once the gear is machined, the pallet moves to a micro-coordinate measuring machine located at Station B (1b) for the dimension measuring task. After the dimensions of the object are verified, the finished object takes exit from Station 1 (output station, 1c). Thus, the whole process path of the mobile pallet in order to successfully complete all the manufacturing tasks is path (1a)→(1b)→(1c). There is a possibility of damaged cell on the surface that means where the PEDCs of the cell cannot be activated. In order to avoid damaged cells, thanks to the matrix design configuration of the SEC platform which allows independent controlling of each PEDC in each cell, it is able to change the path of mobile pallet automatically and an alternative path is defined, for example; path (1a)→(2)→(1c). In this way, all the tasks are finished without any manual intervention and replacement. If only one task is required to be done, such as the raw object has to be moved directly to Station B for the dimension measuring task, instead of following the whole process path, the pallet takes the shortest possible path i.e., path (3)→(1c). By doing this, the minimum consumption of energy can be achieved and the process is much faster. The conveyance system can also be configured to control the trajectories of several pallets moving at the same time to avoid collisions. To achieve these tasks, a dedicated control system is required in future.

Chapter 3: Modeling and sizing of Smart Electromagnetic Conveyor (SEC) platform

This chapter presents the modeling of a single Linear Motor (LM) in order to characterize the generation of forces according to the current magnitude, number of magnets, distance between the magnets and the coil and transition zone between the two cells. The realization of the model will allow to study the architecture of the actuator in order to optimize it and will also facilitate the design. This chapter details the realization of the model of the actuator which includes static model and dynamic model. The static model is implemented in the semi analytical software RADIA that computes the electromagnetic forces exerted on a PMA in the 2D actuator design. And then the static analysis in the transition zone is performed that ensures the functioning of the matrix design of the SEC platform. After this, the dynamic model is implemented in MATLAB/Simulink to study the motion behavior of the PMA in the transition zone and to compute displacement of the mobile part.

3.1 Model of a single linear motor

In this section, the analytical magnetic flux density and electromagnetic force computation models of a single linear motor are presented. These models are based on the previous models developed for the Micro Positioning System (MPS) system in the previous works explained in Chapter 2 [KHAN 2014].

3.1.1 Magnetic flux density model

In the first step, an analytical model of the magnetic flux density computation for a PMA is described. This model is necessary to compute electromagnetic forces. During the development of this model, some hypotheses were considered. The geometries of the PMs are considered perfect and their magnetizations are equal, uniform and oriented along z- axis.

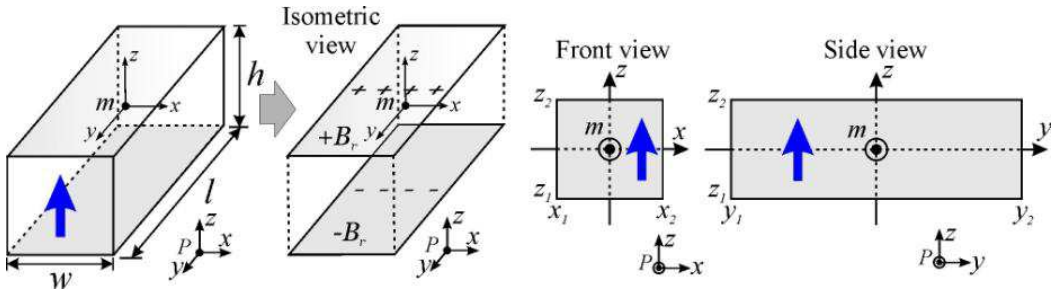

Figure 3.1 Reduction of a single PM to equivalent magnetic charge distribution and its 2D representation in reference frame [KHAN 2014]

Based on these assumptions, a single PM with magnetic polarization along z-axis is reduced to a distribution of equivalent magnetic charge as shown in Figure 3.1 [FURL 2001]. The analytical expression for magnetic flux density components B_x, B_y and B_z at any point located outside the PM dimensions are given by (3.1) [FURL2001]. The center of the PM is located at "*m*" and $(x_2 - x_1)$, $(y_2 - y_1)$ and $(z_2 - z_1)$ represent the dimensions of the PM along the three axes. In addition, μ_0 is the magnetic permeability of air ($4\pi\times10^{-7}$ $N\cdot A^{-2}$) and M_s is the magnetization of the permanent magnet (A/m).

$$B_x(x,y,z)=\frac{\mu_0 M_s}{4\pi}\sum_{k=1}^{2}\sum_{m=1}^{2}(-1)^{k+m}\ln\left(\frac{(y-y_1)+\left((x-x_m)^2+(y-y_1)^2+(z-z_k)^2\right)^{1/2}}{(y-y_2)+\left((x-x_m)^2+(y-y_2)^2+(z-z_k)^2\right)^{1/2}}\right)$$

$$B_y(x,y,z)=\frac{\mu_0 M_s}{4\pi}\sum_{k=1}^{2}\sum_{m=1}^{2}(-1)^{k+m}\ln\left(\frac{(x-x_1)+\left((x-x_1)^2+(y-y_m)^2+(z-z_k)^2\right)^{1/2}}{(x-x_2)+\left((x-x_2)^2+(y-y_m)^2+(z-z_k)^2\right)^{1/2}}\right) \quad (3.1)$$

$$B_z(x,y,z)=\frac{\mu_0 M_s}{4\pi}\sum_{k=1}^{2}\sum_{n=1}^{2}\sum_{m=1}^{2}(-1)^{k+n+m}\times\tan^{-1}\left(\frac{(x-x_n)(y-y_m)(z-z_k)^{-1}}{\left((x-x_n)^2+(y-y_m)^2+(z-z_k)^2\right)^{1/2}}\right)$$

Based on these equations, the magnetic flux density distribution model for "*R*" PMs assembled in a PMA with NS configuration was developed. In this case, all PMs are reduced to the distribution of equivalent magnetic charges as shown in the Figure 3.2 [KHAN 2014].

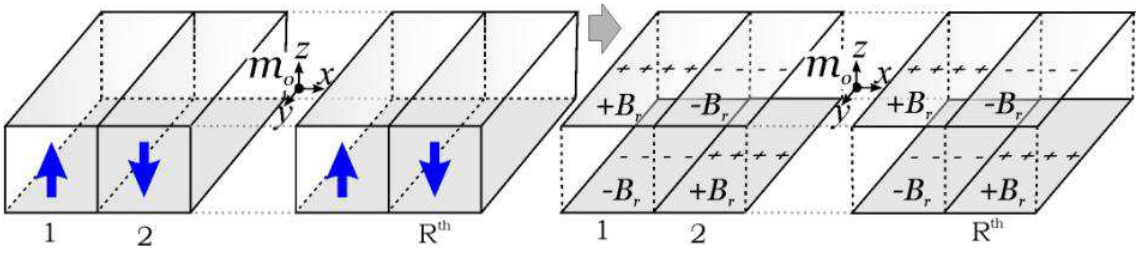

Figure 3.2 Reduction of "*R*" PMs in a PMA to equivalent magnetic charge distribution [KHAN 2014]

The total magnetic flux density at any point is defined as the sum of the contribution of each PM and is expressed in equation (3.2) [KHAN 2014].

$$B_{ext}(x,y,z)=\sum_{i=1}^{R}(-1)^i\times B_{ext}^{(i)}(x,y,z) \quad (3.2)$$

Where B_{ext} and i are the external magnetic flux density component (B_x, B_y, B_z) and index of the PM in the PMA, respectively.

In the previous works [KHAN 2014], the analytical model was implemented in MATLAB software for a PMA with 14 PMs with the airgap of 100 µm between the PMA and conductor. It has been concluded that over the PMA length (along *y*- axis), the B_y component of the magnetic field remains constant except at the edges of the PMA. This is due to the concentrated magnetic field near the ends of PMs. However, the B_y component has been neglected in order to reduce the magnetic flux density computation time during simulations. The main reason behind this assumption is that the contribution of *By* component in the generation of electromagnetic force is very small. Also, B_x and B_z magnetic field components are the ones responsible to generate translation and levitation forces, respectively and hence, produces motion.

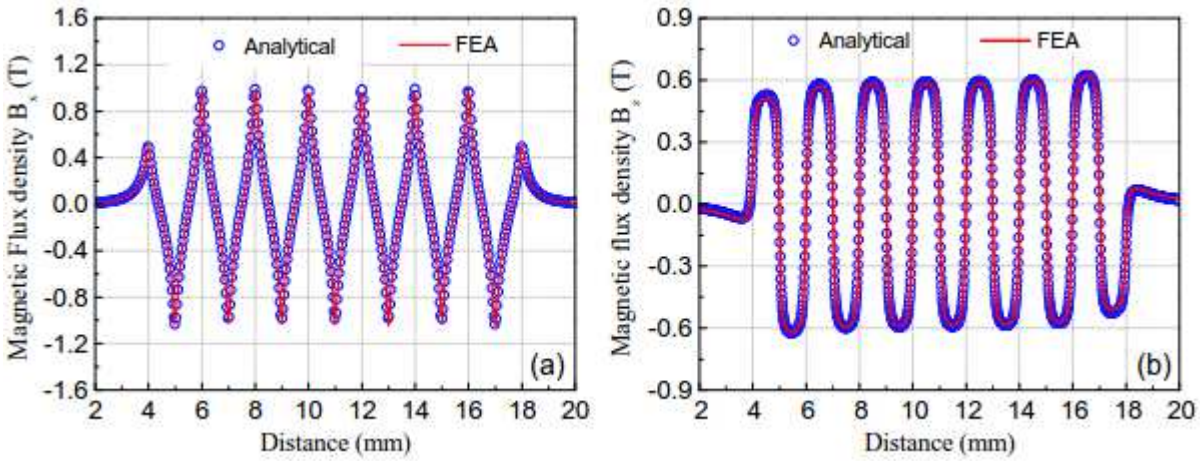

Figure 3.3 Comparison of the magnetic flux density components [KHAN 2014]

The analytical magnetic flux density computation model has been validated for a PMA composed of 14 PMs where each PM of 6 × 1 × 1 mm^3 in volume with Remanent magnetization, Br of 1.43 T. The B_x and B_z magnetic field components generated by the PMA were compared to Finite Element Analysis realized in COMSOL. The comparison of both components showed a good agreement with the relative order of 10^{-5} T (Figure 3.3) [KHAN 2014].

The analytical model had been also validated for small rotations of the mobile part about *z*-axis. In this case, B_x and B_z magnetic flux density components over the length of the conductor will vary due to the relative angle between the PMA and PEDCs. Simulation were performed in MATLAB using the PMA consisting of four PMs at the angles 0°, 2.5°, 5° rotation angles were compared to the FEA analysis. And a good agreement was found

between the two analyses. It has been concluded that this model can be used to represent the magnetic field variation over the length of PEDC.

In previous studies mentioned above, each PM was 6 × 1 × 1 mm^3 in volume whereas in this work, smaller PMs of dimensions 6.0 × 1.0 × 0.5 mm^3 are used. However, the remanent magnetization of the both PMs equal to 1.4 T. This shows that the PMs with smaller PMs used in this work are as powerful as the bigger ones and will have similar magnetic behavior. They also contribute to the light weight design of the LM. Therefore, same magnetic flux density models are used in this work.

3.1.2 **Electromagnetic Force Computation model**

The next step is the modeling of Lorentz electromagnetic force. Its expression is function of current flowing in the conductor, the length of the conductor and the external magnetic flux density that reigns around it. The expression of the model of magnetic flux density along the conductor (see equation 3.3) is integrated in order to determine electromagnetic forces. This expression is also implemented in the static model developed in the software RADIA and also in analytical model to compute magnitude of forces that has been developed in MATLAB/Simulink.

$$F_{electromagnetic} = NI\int_{conductor} dl \times B_{ext} \qquad (3.3)$$

Where :

$F_{electromagnetic}$: Electromagnetic force (N)

N : Number of conductors in a single PEDC

I : Current flowing in the conductor (A)

l : length of the conductor (mm)

B_{ext} : External magnetic flux density (T)

In the previous works, it has been concluded that the total force about the center of the MPS is the vector sum of the electromagnetic forces generated by each linear motor of the MPS system [KHAN 2014]. The forces were computed for a single LM consisting of 14 PMs in a PMA and 60 conductors representing two phase coil currents. Current magnitude of 0.8 A has been injected in the PEDCs with the airgap of 100 µm. The computed translation and levitation forces obtained were 36.61 mN and 55.36 mN in RADIA. A very small error of less than 1% was obtained in the analytical computations of forces.

In this work, considering the design of the SEC platform composed of two layers of PEDCs for *x*- axis translation and *y*- axis translation, the distance between the PEDCs and PMs is very crucial in computing Lorentz force. The force computations for *x*- axis and *y*- axis have been done by considering the distances between the PMAs and Layer 1, and PMAs and Layer 2; respectively. Since these two distances are different in the design, forces generated using Layer 1 and Layer 2 will be different with the same current amplitude. However, equal forces are needed in both the Layers of the SEC platform in order to have same motion behavior along the two axes. For that, higher currents need to be injected if the distance between the PMA and PEDCs is more. However, the current amplitude is limited due to the design constraints of the PEDCs. An analysis is performed to obtain equal forces along the two axes. Before presenting this analysis, the sizing and design limitations of the SEC platform that are considered for the force analysis are presented in the next section. Later, the force analysis based on static and dynamic functioning of the SEC platform is discussed in further sections.

3.2 Sizing of the SEC platform

In this work, a prototype of the SEC platform is designed and manufactured. As mentioned before, the prototype is a 5 × 5 matrix square design where each elementary cell of the matrix is composed of two orthogonal pairs of PEDCs. The dimensions of each cell are 25 mm × 25 mm. These dimensions have been chosen according to the dimensions of the silicon pallet and the PMs. Each PMA is composed of 14 commercially available Neodymium Iron Boron PMs where each PM measures 6 mm × 1 mm × 0.5 mm in dimensions. The remanent magnetization of each PM is 1.4 T. The magnetization is periodically oriented along the z-axis.

Apart from the size and dimensions mentioned above, two parameters are very crucial while sizing the SEC platform in order to perform continuous motion behavior. First is the transition zone which is the gap between two adjacent cells of the matrix and second is the distance between the PMAs and the PEDCs in Layer 1 and Layer 2. Both these parameters are described and their influence on the motion behavior is further discussed in this work.

3.2.1 Transition zone

Due to the design constraints of the PEDCs, a transition gap (g_t) exists between two adjacent cells of the matrix (Figure. 3.4 (a) and (b)). This design limitation is due to the presence of current source pads (through vias) that are used in the coil design for the connections between the conductors for a single phase coil and for the connections to the external power sources.

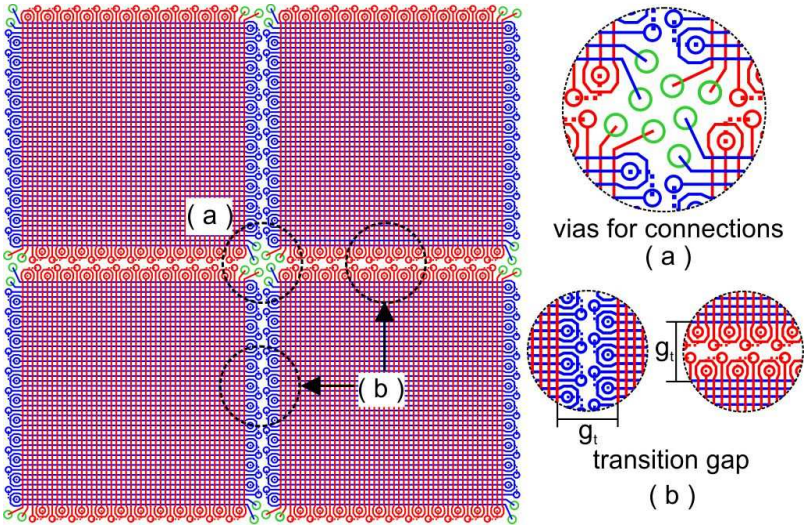

Figure 3.4 Transition gap (g_t)

The length of the transition gap (g_t) between two elementary cells of the matrix is crucial to achieve continuous motion of the cross structure pallet. The larger is transition gap, the less force will be generated. Hence, it is important to reduce the transition gap as much as possible to minimize the force loss to ensure a smooth displacement without interruption.

Figure 3.5 details a strategy that has been adapted to inject currents in transition zone that helps in obtaining continuous motion without interruption despite of less force. In Figure 3.5, PMA is crossing over the transition zone between two cells (cell 1 and cell 2) is represented. Initially cell 1 is activated, and PMA is moved (Figure 3.5(1.)). Once the PMA crosses the transition zone and arrives at the cell 2, it will be activated and the force generated together by the interaction between magnetic flux density generated by PMs and currents flowing in cell 1 and 2. It helps to move the PMA towards cell 2 (Figure 3.5(2.)). This action helps the PMA to cross from cell 1 to cell 2 in a smooth motion. Once the PMA moved to cell 2, cell 1 will be

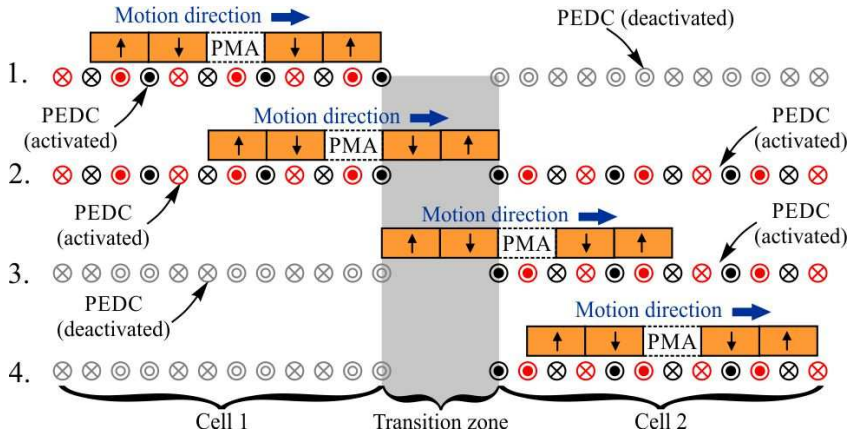

Figure 3.5 Cross sectional view and motion behavior in transition zone

deactivated (Figure 3.5(3.)). In this way, continuity of the motion can be obtained without much increasing the energy consumption.

Based on the above discussion, it is observed that the smaller the transition gap, the better for the motion continuity. It leads to easy transition of the pallet from one cell to the other. Various different design parameters are considered to obtain minimum transition gap (gt). This gap is limited due to the design constraints of the coils and also, the standard specifications given for manufacturing PCBs where the minimum standard distances between a via and a coil, distance between two vias, minimum drill size of a via and thickness of the coils etc. have been considered.

3.2.2 **Distance between the PMAs and PEDCs**

A standard four layer PCB is used for the fabrication of the SEC platform. The first two layers of the PCB are dedicated to two orthogonal PEDCs. The fourth layer is used for routing and connections to the external power source. The third layer is not used for the functioning purpose. The four layer PCB layout for the single linear motor is shown in Figure 3.6. The advantage of using four layer PCB configuration is the large distance between the PEDCs (Layer 1 and 2) and the routing layer (Layer 4) that can be obtained and that helps in avoiding any disturbances (e.g., electromagnetic, Joule heating, etc.) between the PEDCs and the routing layer during functioning. In standard four layer PCBs, a thick core is used between

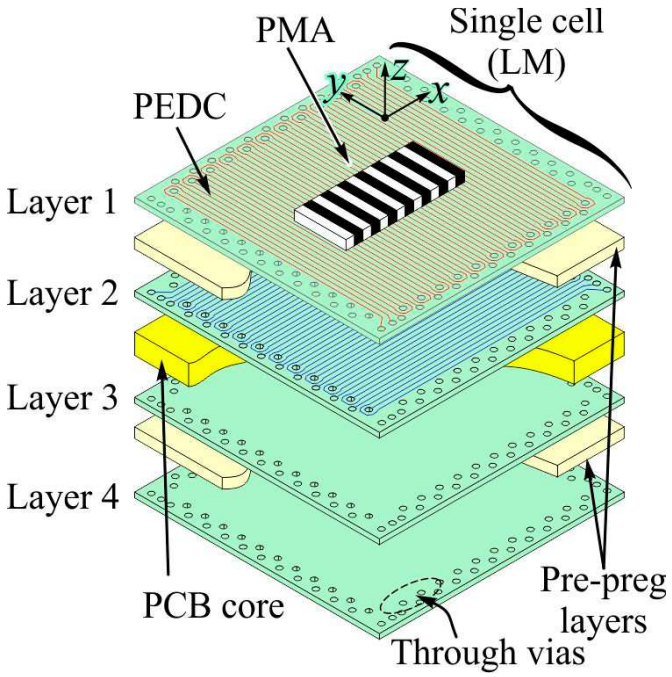

Figure 3.6 Four layer PCB layout

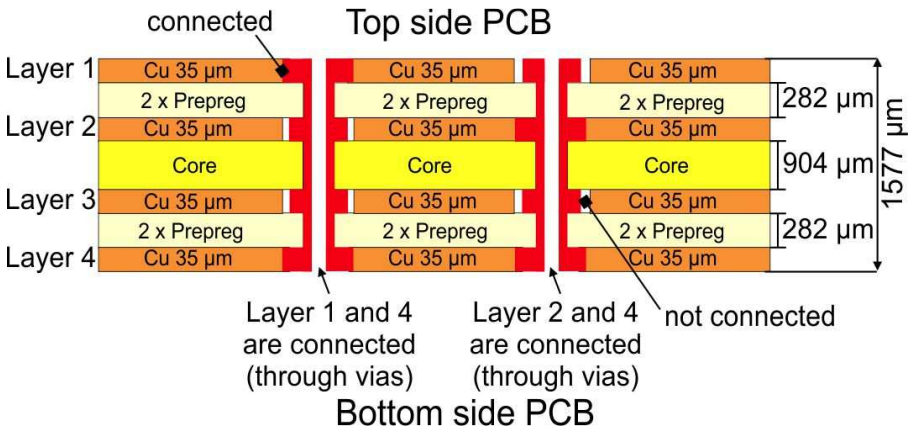

Figure 3.7 Four layer PCB stack up

Layer 2 and Layer 3 to stack all the layers together during manufacturing to make it a rugged structure. Due to the presence of this thick core, the distance between the Cu PEDCs and the routing layer is increased which ensures disturbance free functioning of the actuator. It also ensures the rigid build up of the PCB.

Four layer PCB stack up used for the manufacturing of the prototype structure is presented in Figure 3.7. The thickness of the PCB is limited due to the standard thickness of the materials used in between each layer during fabrication. Layer 1 and Layer 2 consist of two pairs of PEDCs, each with 35 µm thickness of copper. Two prepregs are pressed together to stack Layer 1 with Layer 2 and Layer 3 with Layer 4. The total thickness of the two prepregs is 282 µm which is also the distance between the first two layers. The total thickness of the PCB is 1577 µm with a 904 µm thick core between Layer 2 and Layer 3. The connections of Layer 1 and Layer 2 with the routing layer (Layer 4) are realized using through vias (Figure 3.7).

In order to ensure insulation between the PMA and the PEDC in Layer 1 and to minimize friction, a thin glass layer is placed. In case of 2D actuator, one glass layer is glued to the bottom of the mechanical support of the PMAs. For SEC platform, four glass layers are glued to the bottom of the four edges of the silicon pallet (four cavities) where the PMAs are placed. In both the cases, the presence of the glass layers under the cavities fabricated to place PMAs also helps for easy and uniform assembly of the PMAs. It can be done just by placing the PMAs over the glass layers in the cavities. The thickness of the glass layer is 130 µm. Due to glass layer, the distance between the PMAs and the PEDC in Layer 1 and Layer 2 become 130 µm and 412 µm, respectively. These gaps will be taken into account for the calculation of forces exerted on the PMA.

3.3 Modeling of SEC platform

Static and dynamic models have been developed to the design and sizing the SEC platform. At first, a model of the 2D actuator is developed to validate the working principle of one cell of the matrix design. Firstly, a static model able to compute the forces exerted on PMAs when currents are supplied to PEDCs in Layer 1 and Layer 2 is developed. Using this model, a study on the forces generated using two layers is specially done. An analysis on the force exerted on the PMAs in the transition zone is also performed. Further, a dynamic model to calculate the displacement of the mobile part has been performed. The characteristics of a single cell used for the analysis in this work are mentioned in Table 1.

3.3.1 Static Model

Firstly, the static model analysis of one cell of the matrix is performed. That means performance of 2D actuator is analyzed to predict the functioning of the SEC platform. In this analysis, the influence of the distance between the PMA and PEDCs on the force exerted on the PMAs is studied. Using these results, the second analysis that has been performed is the static analysis of the SEC platform where the force generation in the transition zone of the platform is studied. This analysis ensures the functioning of the SEC platform in the transition zone so that the mover can perform motions on the whole platform without any interruption.

Table 1

SINGLE CELL CHARACTERISTICS	
SIZE OF ONE CELL	25×25 MM^2
LENGTH OF EACH CONDUCTOR	25 MM
NO. OF CONDUCTORS IN ONE CELL	46
TRANSITION GAP BETWEEN TWO CELLS	3.5 MM
DISTANCE BETWEEN EACH CONDUCTOR	0.5 MM
SIZE OF EACH PM	$6 \times 1 \times 0.5$ MM^3
THICKNESS OF THE GLASS LAYER	0.13 MM
DISTANCE BETWEEN PMA AND LAYER 1	0.13 MM
DISTANCE BETWEEN PMA AND LAYER 2	0.412 MM
REMANENT MAGNETIZATION OF EACH PM	1.4 T

3.3.1.1 2D actuator with two layer coil assembly (one cell of the SEC platform)

Based on the design of 2D actuator presented in Chapter 2, six PMs are used for the translation along *x*- axis (two PMAs at the extremities, each having 3 PMs) and *y*- axis (PMA at the centre with six PMs), a model is developed in RADIA to compute electromagnetic forces applied on the 2D actuator (Figure 3.8). The distance between each PMA is kept 2 mm for easy arrangements on the mechanical support and also to prevent any interactions between the PMAs which could affect their behavior.

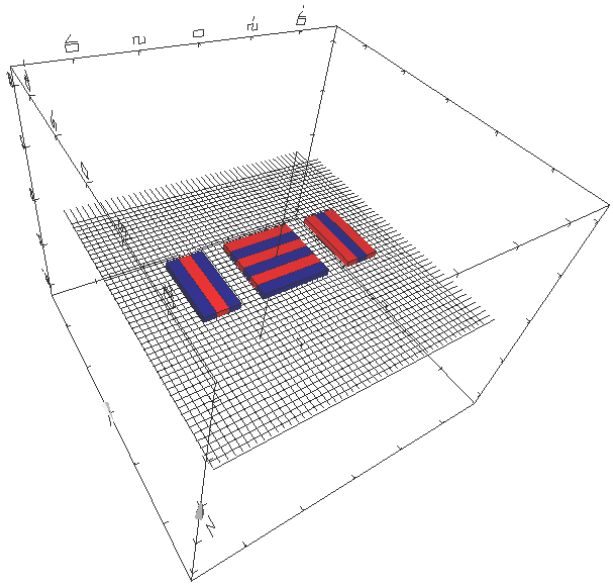

Figure 3.8 2D actuator view in RADIA

As mentioned earlier, the distance between the PMA and PEDCs plays an important role in functioning of the actuator. As the distance between PMA and Layer 1 (130 µm) is smaller than the distance between PMA and Layer 2 (412 µm), higher magnitude of forces will be generated using Layer 1 than Layer 2. Hence, motion behavior will be different along the two axes. In order to generate equal forces along the two axes, higher current needs to be injected in Layer 2. Therefore, an analysis has been performed to obtain the same motion behavior in the two layers.

The maximum allowable current per coil is 0.8 A which is limited due to joule heating [KHAN 2014]. The model has been used to compute the net translation and levitation forces generated by injecting the current ranging from 0.2 A to 0.8 A in each layer. This will give the nominal value of current which is enough to generate motion using both layers.

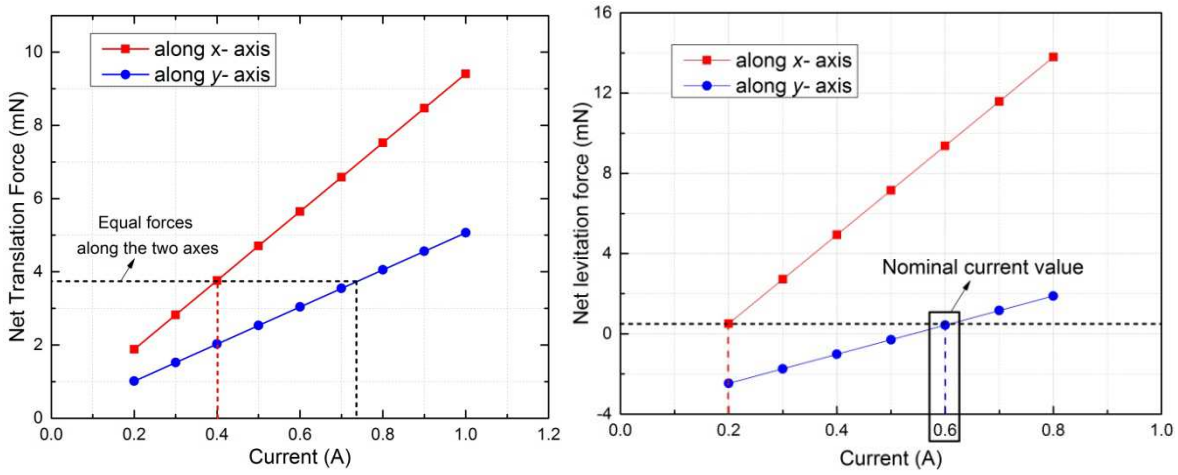

(a) **(b)**

Figure 3.9 Force computations (a) Net translation force (b) Net levitation force

Firstly, the net translation forces exerted on the PMAs by the PEDCs in Layer 1 (F_x) and Layer 2 (F_y) have been computed for different current values considering the distances between the first two layers and the PMAs. Figure 3.9 (a) represents the evolution of the net translation forces along the *x*- and *y*- axes (F_x and F_y) in function of current values. The analysis shows that in order to generate the same net translation forces along both axes, the PEDCs of Layer 2 requires higher current value as compared to the PEDCs of Layer 1 and the relation between these two currents is given in Eq. (3.4).

$$I_{top} = 0.538 \times I_{bottom} \tag{3.4}$$

where I_{top} is the current injected in the Layer 1 and I_{bottom} is the current injected in the Layer 2.

Similarly, the net levitation forces are computed along the two axes in order to compensate the weight of the mobile part. The graph in Figure 3.9(b) represents the net levitation forces in function of current amplitude. For the motion along *x*- axis (using Layer 1) and *y*- axis (using Layer 2), the minimum current required for the motion is 0.2 A and 0.6 A, respectively. The nominal current value has been chosen at 0.6 A for the motion along both the axes because it represents the minimum value of the current required in Layer 2. This ensures a positive residual levitation force that partially compensates the net weight (i.e. W_{net}) of the mover where $W_{net} = W - F_z$ where F_z is the levitation force and W is the weight of the mobile part, 3.92 mN in this case. Higher current amplitude can also be used but the nominal current value has been chosen to prevent heating of the coils during back and forth motions.

3.3.1.2 SEC platform

For the SEC platform, the mobile part is the silicon pallet where each linear motor consists of 14 PMs in a PMA. Therefore, the force computations are performed using 14 PMs in one LM Figure 3.10 (a). The computed forces are doubled as two PMAs are required for the motion of the pallet along an axis. The PMA is placed over two PEDCs consisting of 46 conductors representing two phase currents.

An analysis has been performed using the static model in order to compute electromagnetic forces exerted on a PMA. Two analyses are performed considering two crucial parameters.

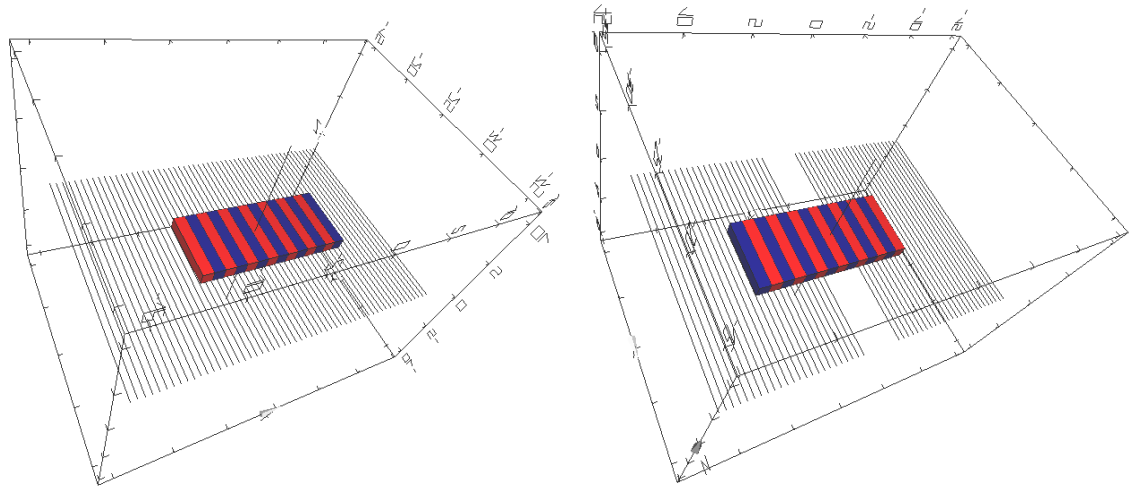

(a) **(b)**

Figure 3.10 RADIA view (a) Single LM (b) PMA in the transition zone with six conductors removed

First, the distance between the PMA and PEDCs in Layer 1 and Layer 2 is considered to compute forces. This analysis would give the nominal currents required to perform motions of the pallet along *x*- and *y*- axis. Second, the force computations in the transition zone using the nominal currents obtained for *x*- and *y*- axis motion from the previous analysis. It ensures the motion of the pallet in the transition zone using the nominal currents.

As mentioned before, the distance between the PEDCs and PMAs is crucial for the functioning of the platform. For that, it is important to find out the minimum current required for the motion along *x*- and *y*- axes. An analysis has been performed to compute forces considering the distance between PMA and PEDCs in Layer 1 (130 µm) and Layer 2 (412 µm) in function of different current amplitudes. Figure 3.11 represents the evolution of net translation and levitation forces in Layer 1 and Layer 2 with the increase in current amplitude.

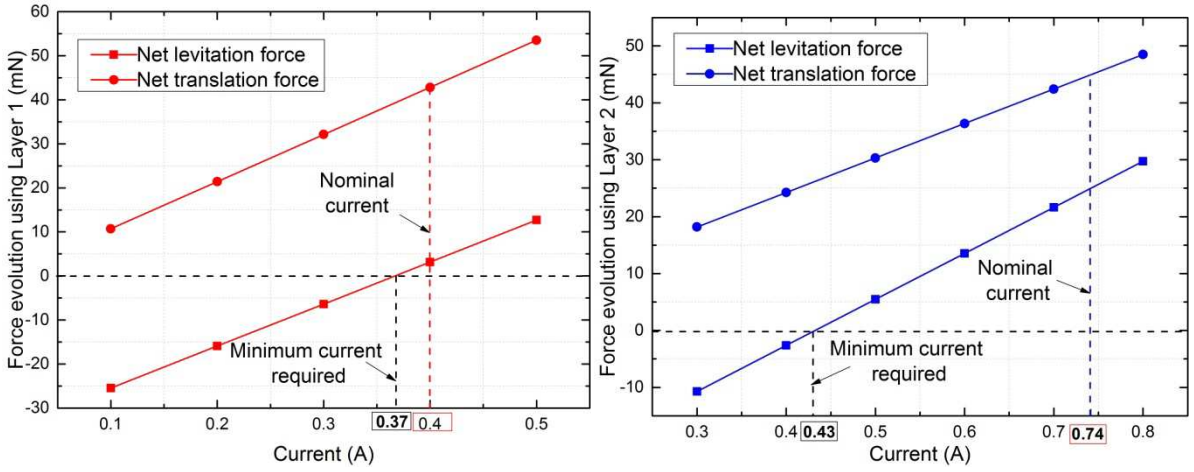

(a) **(b)**

Figure 3.11 Lorentz forces in function of current magnitude (a) along x- axis (b) along y- axis

As mentioned in the previous section of 2D actuator, net levitation forces are computed considering the weight of the mobile in order to compensate it. The mobile part in case of SEC platform is the silicon cross structure pallet. The weight of the mobile part is 3.6 g (W=35 mN) that includes the weight of the silicon pallet, four PMAs and the four glass layers attached to the bottom of the four edges of the pallet. It can be observed, for Layer 1, that the current equal to or higher than 0.37 A ensures positive residual levitation force that partially compensates the net weight ($W_{net}=W-F_z$). 0.4A has been chosen as the nominal current value for Layer 1 because the current in Layer 2 should not exceed the maximum allowable current and this would be chosen according to (3.4). At 0.4 A in Layer 1, the computed net translation force is 42.8 mN (Figure 3.11 (a)). Similar analysis has been performed for Layer 2 shown in Figure 3.11 (b). The current value 0.43 A is the minimum current required that partially compensates the weight of the mobile part using Layer 2. According to (3.4), the current should be equal to 0.74 A in Layer 2 if the current in Layer 1 is 0.4 A in order to generate equal forces in the two layers. Therefore, the nominal current value in Layer 2 is 0.74 A. The computed net translation is 45 mN using Layer 2 (Figure 3.11 (b)).

Therefore, the computed net translation forces using the two layers are approximately equal using the nominal current values 0.4 A and 0.74 A for Layer 1 and Layer 2 respectively. Based on the above analysis and considering equation (3.4), all the force computations are done by injecting nominal currents in the two layers.

As mentioned in the previous sections, the transition zone between two elementary cells of the matrix is a crucial parameter to achieve continuous motion due to missing conductors in this zone. Another analysis has been performed in order to compute forces in function of no. of

conductors removed in the transition zone. Conductors are removed to compute forces in the transition zone. The RADIA view of a single LM and PMA in the transition zone is shown in Figure 3.10 (b). This analysis has been done to observe that with the chosen nominal currents for Layer 1 and Layer 2 in the previous analysis, how many conductors can be removed from the transition zone. Even if fewer conductors are removed, the higher the force is, the analysis will give the maximum transition gap that ensures a possible motion.

The generated electromagnetic forces have been computed in function of number of conductors removed from 0 to 10 (Figure 3.12 (a)). Two conductors are removed each time from the two PEDCs, one from each PEDC in each layer. It is obvious that the forces will reduce with the number of conductors removed underneath the PMAs. Further, the total weight of the mobile part 35 mN is considered while computing the net levitation forces in the two layers. Figure 3.12(c) represents the decrease in computed net levitation forces along *x*-

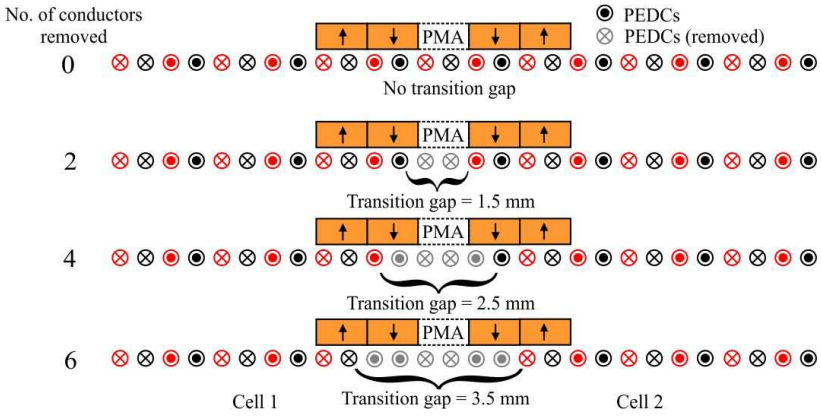

(a)

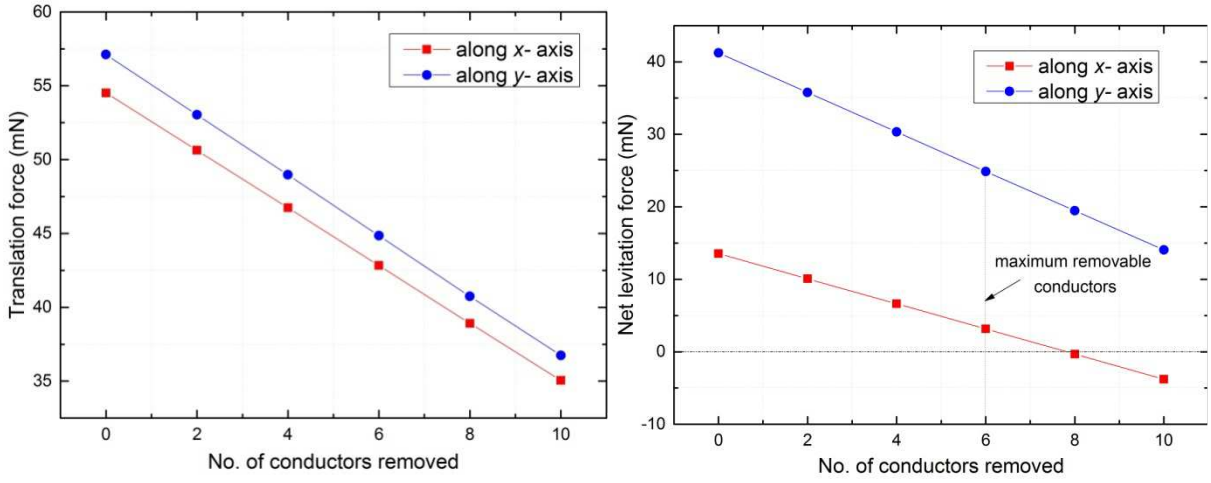

(b) (c)

3.12 Force computation in the transition zone (a) Increase in transition gap (b) translation force (c) levitation force

and *y*- axes with more no. of conductors are removed. It can be observed that when 6 conductors are removed, the positive residual levitation force along both the axes partially compensates the weight of the mobile part, however, when 8 conductors are removed, the computed net levitation force remains negative in Layer 1. That means it does not compensate the weight of the mobile part along *x*- axis. Therefore, the analysis shows that no more than 6 conductors can be removed with the chosen nominal currents 0.4 A and 0.74 A in Layer 1 and Layer 2, respectively. Therefore, the maximum transition gap feasible for the functioning of the SEC platform is 3.5 mm. The computed translation forces for *x*- and *y*- axis motion are decreasing as more conductors are removed (Figure 3.12 (b)). As mentioned before, the computed translation forces are 42.7 mN and 45.0 mN for Layer 1 and Layer 2, respectively when 6 conductors are removed. Compared to the configuration without removing conductors, the percentage decrease in force in the transition zone is 21.2% and 21.4% in Layer 1 and Layer 2, respectively.

3.3.2 **Dynamic modeling**

In this section, a dynamic model is presented and then dynamic simulations have been carried out. At first, the dynamic behavior of 2D actuator is presented in order to study the motion characteristics of one cell of the SEC platform. After that, in order to study the motion behavior of the pallet using Layer 1 and Layer 2 over the transition zone of the SEC platform. The nominal current values of 0.4 A and 0.74 A for Layer 1 and Layer 2, respectively are used in the dynamic analysis in open loop control.

Two sinusoidal currents I1 and I2 (Figure 3.13) are generated with the relative phase shift of $\pi/2$ and injected to force computation model to compute Lorentz forces. Magnetic flux

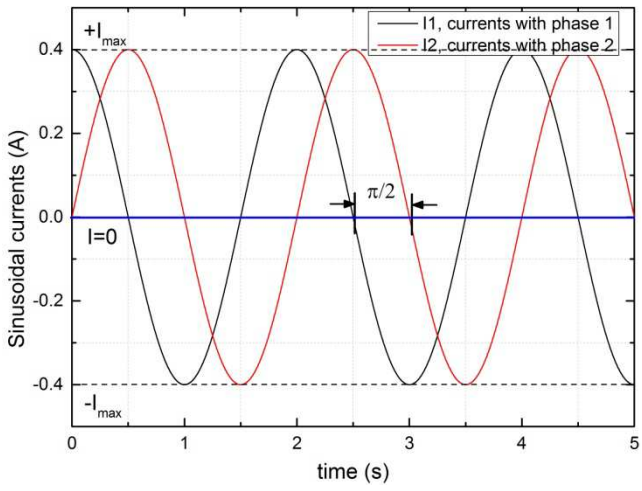

3.13 Currents I1 and I2 for single axis motion

density model (3.2) is taken into account to compute magnetic flux density of the PMA at the relative position (x, z) of the mobile part.

In the dynamic model, the friction and adhesion phenomena are considered. The friction force ($F_{friction}$) is computed with the net weight, $W_{net} = W - F_z$ and the friction coefficient ($\mu_{friction}$=0.21) (3.5). For the adhesion phenomenon, the adhesion force ($F_{adhesion}$) is computed with the net weight of the mobile part (W_{net}) and the adhesion coefficient ($\mu_{adhesion}$=0.23) (3.6).

$$F_{friction} = \mu_{friction} \times W_{net} \tag{3.5}$$

$$F_{adhesion} = \mu_{adhesion} \times W_{net} \tag{3.6}$$

The coefficient $\mu_{adhesion}$ has been determined experimentally using inclined plane technique whereas the coefficient $\mu_{friction}$ has been approximated due to the difficulty way of determining it experimentally. If the generated electromagnetic force enters in the range [$-F_{adhesion}$, $+F_{adhesion}$], its value is set to zero.

$$F = F_{total} - F_{friction} \tag{3.7}$$

where F_{total} is the total force exerted on the PMAs.

The friction force is reduced from the total force generated to calculate the actual force (F) (3.7). By inserting the computed Lorentz forces (3.7), Newton's second law has been used to compute the equation for translation of the mobile part. The displacement, X_d is determined by double integration of the acceleration of the mobile part given in equation (3.8). Simulations are carried out by implementing this model in MATLAB/Simulink.

$$\sum \vec{F} = \vec{F}_{total} - \vec{F}_{friction} = M \frac{d^2 \overrightarrow{X_d}}{dt^2} \tag{3.8}$$

where M is the total mass of the mobile part.

3.3.2.1 2D actuator (one elementary cell)

The displacement of the mover is computed by considering the weight of the mobile part, which is W = 3.92 mN. This weight includes the weight of three PMAs, the mechanical support and a glass layer attached to the bottom side of the mechanical support.

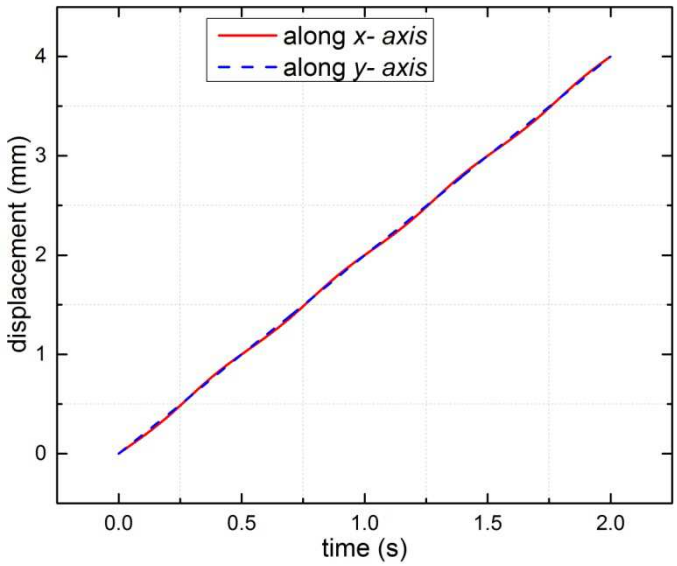

Figure 3.14 2D actuator displacement curve

Six PMAs are considered for the motion along each axis. In the previous section of static analysis, the nominal current was found to be 0.6 A for Layer 2. Based on (3.4), two sinusoidal currents of 0.6 A are injected in the two PEDCs in Layer 2 and two sinusoidal currents of 0.32 A are injected in two PEDCs in Layer 1. This has been done to generate equal forces in the two layers in order to obtain same motion behavior along the two axes. Two periods of 1 Hz sinusoidal currents are injected in Layer 1 and Layer 2. The measured displacement is found to be 4 mm along *x*- and *y*- axis. The displacement curves along *x*- and *y*- axis are presented in Figure 3.14. It can be observed that the two displacement curves are overlapping quite well. This shows that equal forces are exerted on the PMAs for the motion along *x*- and *y*- axes.

3.3.2.2 SEC platform

Using this dynamic model, the displacement of a PMA over the transition zone has been simulated in order to observe the effect of the absence of the conductors in the transition gap, g_t on the displacement (Figure 3.5).

The displacement of the pallet is computed by considering the total weight of the mobile part, which is 3.6 g (W = 35 mN). Two LMs are used to compute the displacement of the mobile

part. Firstly, displacements using Layer 1 are calculated by injecting 20 periods of 2 Hz sinusoidal currents (I1, I2) with 0.4 A into the PEDCs. The computed total displacement in Layer 1 is 40.45 mm without removing any conductor. Then, as it has been realized with the static model, the influence of the transition gap on the mobile part displacement has been studied. For that, one conductor is removed from each coil at each time. This means two conductors are removed at a time. The displacement computed in the transition zone in function of the number of conductors removed from 0 to 6 is shown in Figure 3.15 (a). In the zoom view the effect of removing conductors on the displacement is observed in the curves. The displacement curves are shifting little below as more number of conductors are removed in the transition zone. However, this effect has not changed the total computed displacement. Displacement error in the transition zone is presented in Figure 3.15 (b). This shows that, no significant change in the computed displacement has been found with the transition zone in the simulations. It shows that the removal of 6 conductors does not affect the motion of the mobile part.

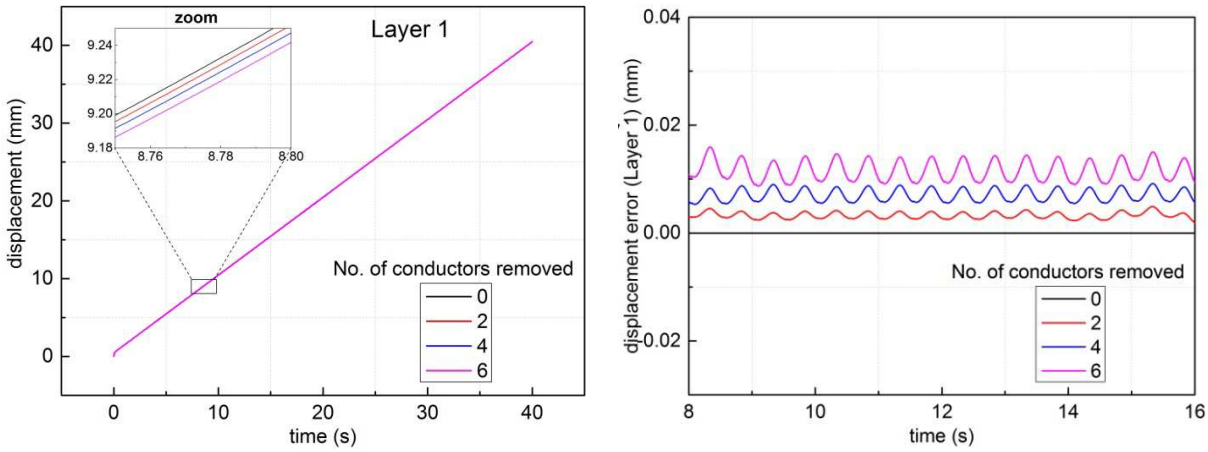

(a) **(b)**

Figure 3.15 Transititon zone analysis (a) Displacement measurement in the transition zone in Layer 1 (b) Displacement error

Similarly, in case of Layer 2, two sinusoidal currents with the amplitude of 0.74 A are injected and the displacement travelled by the pallet is found to be 40.4 mm. It remains the same when the mobile part crosses the transition zone with the transition zone in the simulations.

This study concludes that the chosen transition gap of 3.5 mm where 6 conductors have been removed from each axis is acceptable as it does not deteriorate the performance of the SEC platform. It also ensures smooth motions of the mobile part without any interruption.

3.4 CAD view of four layer PCB

In the previous section, the static and dynamic models enable to validate the proposed design of the PCB. Then the detailed design of the PCB has been done using the CadSoft EAGLE PCB design software. This software is specifically used to design PCBs in order to meet commercial manufacturing standards of PCBs. The manufacturing standards include, Cu width and height, vias drill size, distance between vias and copper, distance between layers etc.

In this section, the PCB design and corresponding CAD views are presented. Figure 3.16 shows an overall CAD view of the PCB with the four layers. Figure 3.16 (a) represents a single cell of the PCB. Through vias of 300 µm drill are used for the connections to the

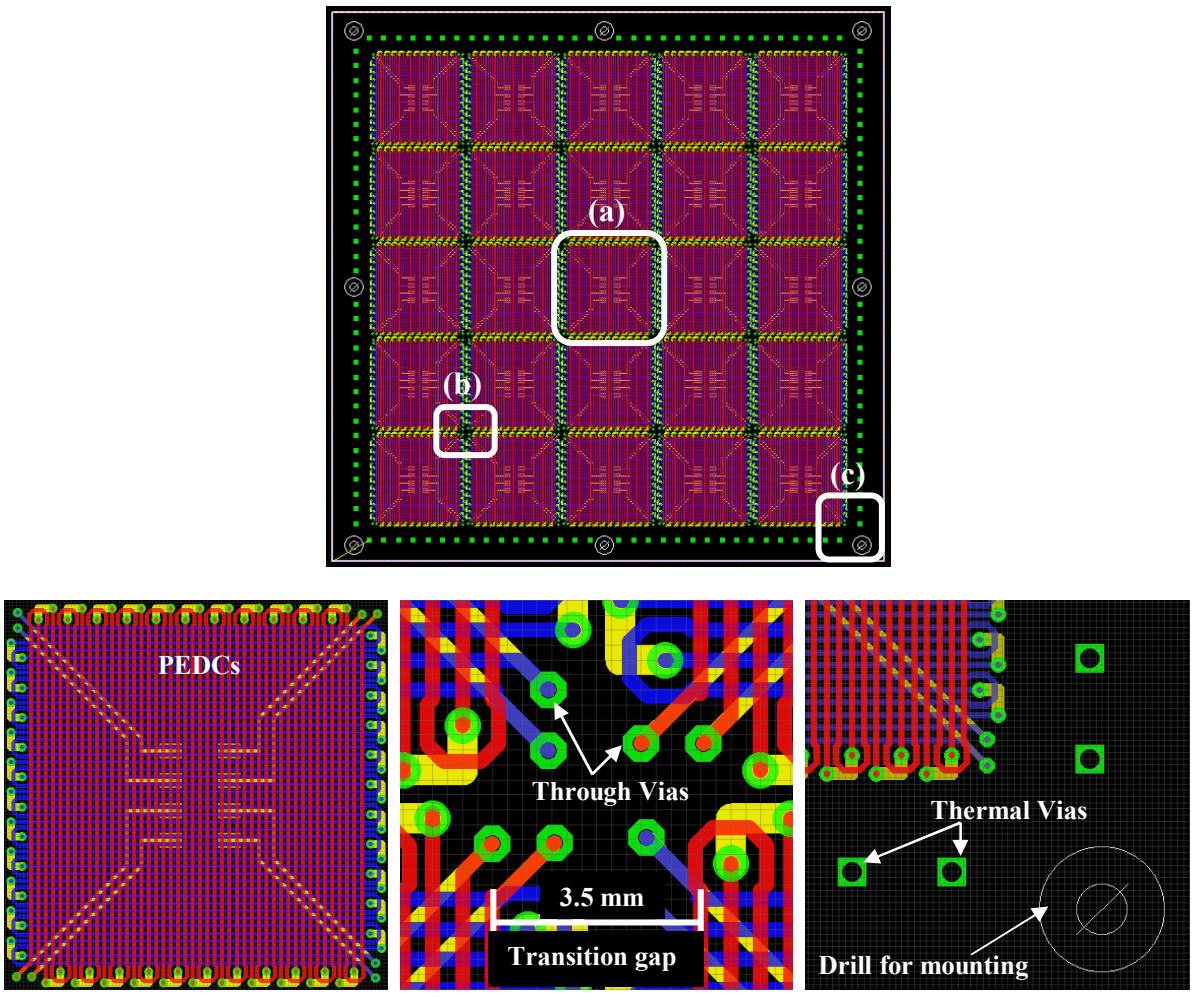

Elementary cell | Transition gap | Thermal vias

(a) | (b) | (c)

Figure 3.16 CAD view of 4 layer PCB design (a) Elementary cell (b) Design constraints (c) Thermal vias

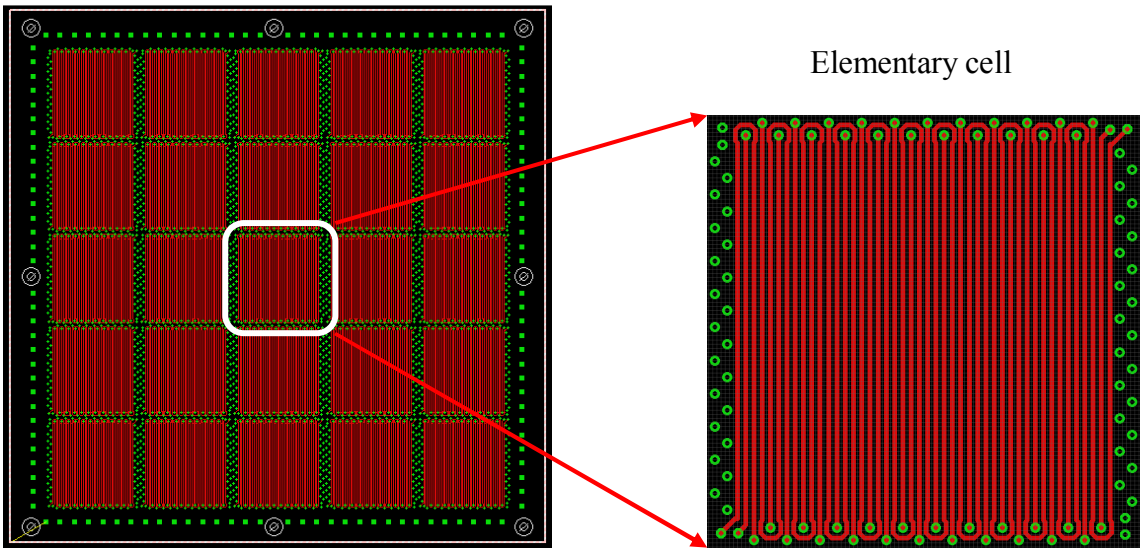

Figure 3.17 CAD view of Layer 1

external power source and routing shown in Figure 3.16(b). The design of the PCB has been realized by considering the standard design parameters for manufacturing a PCB, specially the distance between via-conductor and conductor-conductor, and also a transition gap of 3.5 mm between two cells. Thermal vias of 900 µm drill size have been added around the matrix coil design in order to dissipate heat during functioning (Figure 3.16(c)). Some holes for the mounting purpose have also been added at the periphery of the PCB.

The Figures 3.17 and 3.18 represent overall CAD views and zoom views of an elementary cell of the matrix for Layer 1 and Layer 2, respectively. Layer 1 is used to move the mobile part of the actuator along the horizontal axis and the Layer 2 is used to move along the vertical axis.

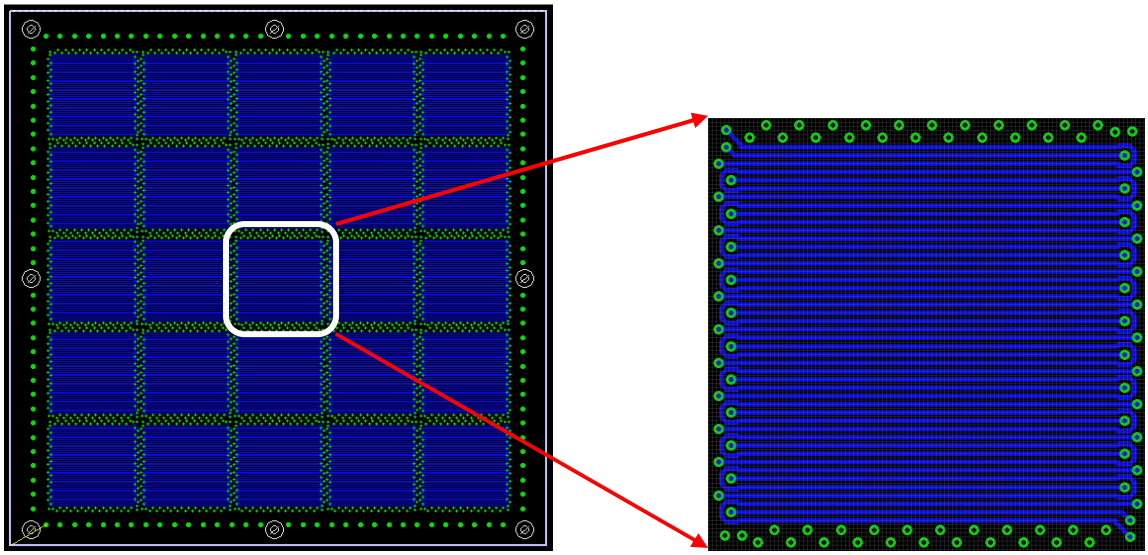

Figure 3.18 CAD view of Layer 2

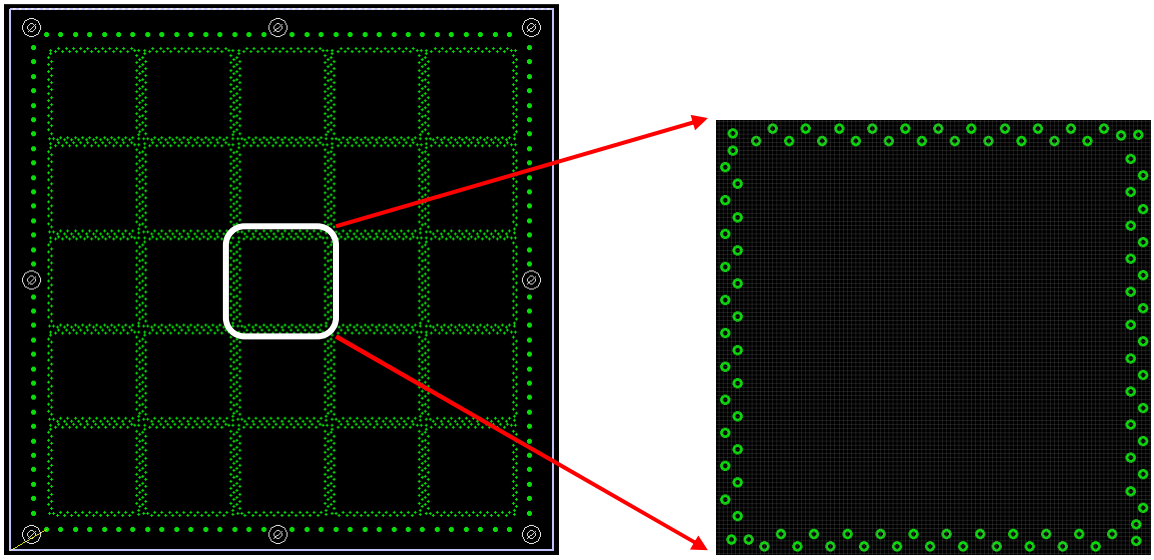

Figure 3.19 CAD view of Layer 3

The zoom views of the elementary cell in Layer 1 and Layer 2 show that the PEDCs are orthogonally arranged.

Figure 3.19 presents the CAD view of Layer 3 in which only through vias can be seen. This layer is then not used for the working purpose. Figure 3.20 presents the CAD view of Layer 4. SMD (Surface Mount Device) pads are fabricated on Layer 4 for the connections to the external power source. 8-pin micro connector is used for four inputs (two inputs for each PEDC) and four outputs (two outputs for each PEDC) for two PEDCs in one cell. Layer 1 and 2 are connected to Layer 4 thanks to through vias.

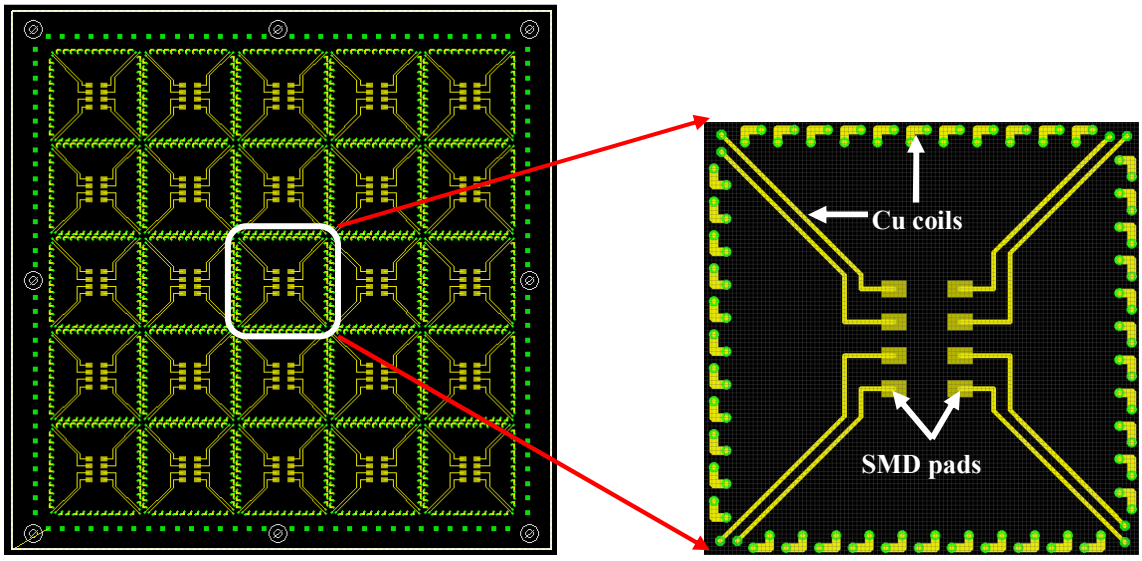

Figure 3.20 CAD view of Layer 4

3.5 Realization of SEC prototype

The four layer PCB for the SEC platform has been realized. The top view of the PCB is shown in Figure 3.21 where Layer 1 is visible.

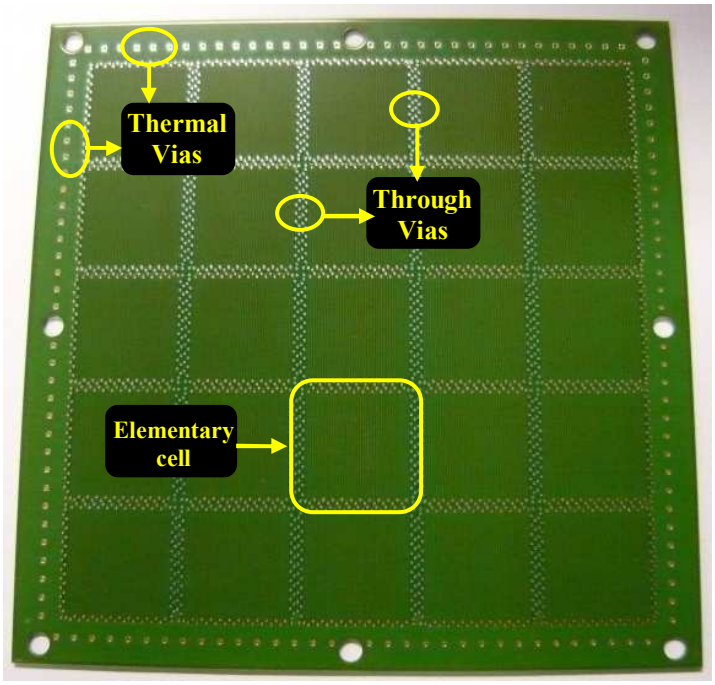

Figure 3.21 Top side view of the SEC prototype

The bottom side of the PCB shows the routing layer (Layer 4) of the PCB (Figure 3.22). SMD pads and input-output connections of the PEDCs in each cell are visible on Layer 4.

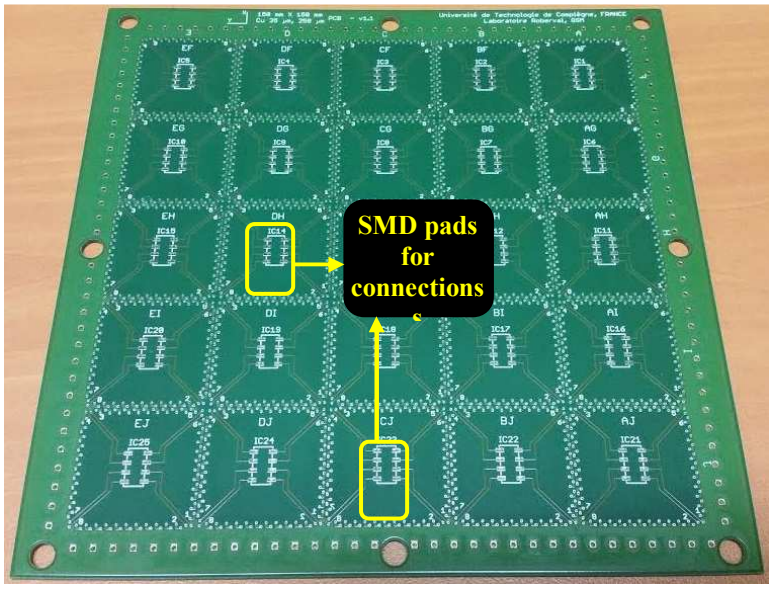

Figure 3.22 Bottom side view of the SEC prototype

The fabrication of the PCB has been done on standard FR4 board. Copper coils are used for the PEDCs in Layer 1 and 2 and for the connections between the coil turns from Layer 4. The PCB is fabricated by commercial PCB manufacturer Multi Circuit Boards Ltd.

3.6 Conclusion

In this chapter, the magnetic flux density model and electromagnetic force computation model for a single LM are presented. The models are then used to compute forces to analyze the static behavior of one cell of the SEC platform. For that, a 2D actuator has been developed in order to test one cell of the platform design. Lorentz force model is used for force computations in function of the distance between the PMAs and the PEDCs in Layer 1 (130 µm) and Layer 2 (412 µm), respectively. The performed analysis has validated the functioning of the developed four layer PCB design. The analysis defines the current required in order to generate equal forces in Layer 1 and Layer 2 in order to obtain similar motion behavior in the two layers. After that, functioning of the whole SEC platform has been modeled by performing force computations in the transition zone which is the gap between two cells of the matrix design. It has been performed in order to validate the transition gap of 3.5 mm that has been achieved by removing 6 conductors between the two cells in both Layer 1 and Layer 2. The transition gap occurs due to the design and manufacturing constraints of PCB design. The analytical modeling has been carried out in order to simulate the motion behavior of the SEC platform to evaluate its dynamic performances in the open loop control. The simulation has been carried out in both Layer 1 and Layer 2 in order to study the effect of transition zone on the total displacement travelled by the mobile part along *x*- and *y*- axis. The analysis has shown no change significant change in the computed displacement in the transition zone along both the axes.

These models have been used for the experimental tests and characterization of the SEC platform that validates the developed models. The experimental results and analysis are presented in the next chapter.

Chapter 4: Prototype and Experimentation

The purpose of this chapter is to first test one cell of the SEC platform prototype. For that, an experimental set up of the 2D actuator (composed of two PMAs each having 6 PMs) has been realized to perform displacements along *x*- and *y*- axis. Then, the experimentation of the full SEC platform has been performed using the moving silicon cross structure pallet. For each axis displacement, different connections between the PEDCs in Layer 1 and 2 have been realized and are discussed in this chapter. The experiments have been carried out in order to validate the working principle and to analyze different motion behaviors of the SEC platform in open loop control. Various linear and planar motion trajectories on the SEC platform have been performed in order to examine the dynamic behavior of the silicon cross structure pallet when it is supplied by both layers.

4.1 2D actuator

In order to verify the proposed concept of the elementary cell composed of two orthogonal PEDCs, the performances of only one cell of the SEC surface has been firstly tested. A 2D actuator has been realized to ensure planar motion of the pallet; thanks to first two layers of coils. The experimental set up and results obtained for the 2D actuator are discussed in this section.

4.1.1 Experimental set up of 2D actuator

The experimental setup has been realized in order to demonstrate the motion of the 2D actuator along *x*- and *y*- axes in open loop. 2D actuator prototype structure is shown in Figure 4.1. As mentioned earlier, the stator is composed of one cell of the fabricated four layer PCB and the pallet is developed by assembling PMAs orthogonally in order to perform planar motions along *x*- and *y*- axis. The PMAs integrated in the pallet part are formed with commercially available Neodymium-Iron-Boron (NdFeB) PMs. The two PMAs (for *x*- and *y*- axes displacements) are composed of six PMs. The six PMs for motion along *y*- axis are assembled at the center of the mechanical support. For motion along *x*- axis, the six PMs are divided into two PMAs, each composed of three PMs and placed at the extremities of the PMAs support. This distributed configuration has been selected in order to achieve symmetrical motion behavior during functioning of the actuator. The PMA support structure of dimensions length, l=10 mm and width, w=20 mm has been manufactured using laser

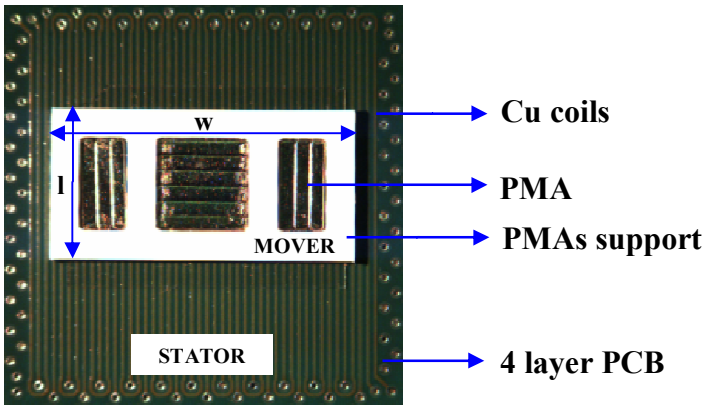

Figure 4.1 Prototype of 2D actuator

cutting machine with a 1 mm thick PMMA sheet. Considering the dimensions of the pallet, it is able to perform 4 mm displacement stroke along *x*- axis and 18 mm along *y*- axis.

The experimental setup is shown in Figure 4.2. The four layer PCB has been mounted on a table with the help of a mechanical PMMA support which has been manufactured using laser cutting machine. A computer equipped with a data acquisition board (NI PCI-6733) is used to generate two controlling voltages for each axis. These voltages are then converted into currents using voltage to current converters. The voltage input and current output of both the

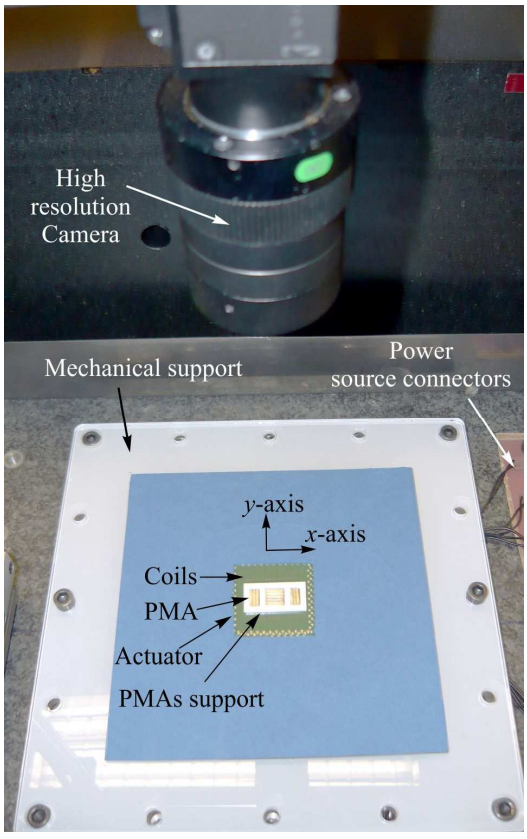

Figure 4.2 Experimental set up of 2D actuator

converters are in the range of [-10 V, 10 V] and [-3A, +3A] with a bandwidth of 50 kHz. For the displacement measurement, a high resolution camera (FLEA 2 – Point Grey) has been fixed above the PCB in order to capture images of the pallet during motion. To calibrate the camera, the first important thing is the desired motion range of the pallet depending on which field of view of the camera can be selected. The camera has been kept as close as possible to the PCB so that it covers the desired area of one cell of the matrix. The lengths of the PEDCs are used for the inclination and alignment purpose of the camera. An image is taken and the lengths of the two extreme PEDCs are measured using image pixels. If the lengths of the two extreme PEDCs are equal, it means the camera is well aligned. A low reflect grid distortion target # 62949 from Edmund Optics has been used to determine the resolution of each pixel. The pattern size is 25 mm × 25 mm with each dot diameter 0.0625 mm and the dot spacing is 0.125 mm. The resolution of each pixel has been determined by counting the dots to compute how many millimeters each pixel represents. The resolution of each pixel depends on the field of view of the camera which is changing in this work based on the different experiments performed. This information will be provided in the details given for each experiment in further sections.

Several images have been captured by the camera which is then used to measure the total displacement. This is explained in detail in further sections. In order to control the motion of the actuator, a LABVIEW interface has been developed.

4.1.2 **Linear displacements**

Experimental tests of the device have been carried out in open loop. For the experimental analysis, at first, a 2 mm forward and backward motion has been performed along x- axis. This has been done by injecting two sinusoidal signals of 2 Hz with the current amplitude of 0.6 A in the two PEDCs in Layer 1. Similarly, y- axis displacement have been performed by injecting two sinusoidal currents of 2Hz with the same current amplitude of 0.6 A in the two PEDCs in Layer 2. The actuation speed of the signals along the two axes is 4 mm/s. Images were captured by the camera while motion to demonstrate the motion along *x*- and *y*- axes are presented in Figure 4.3 (a) and (b), respectively.

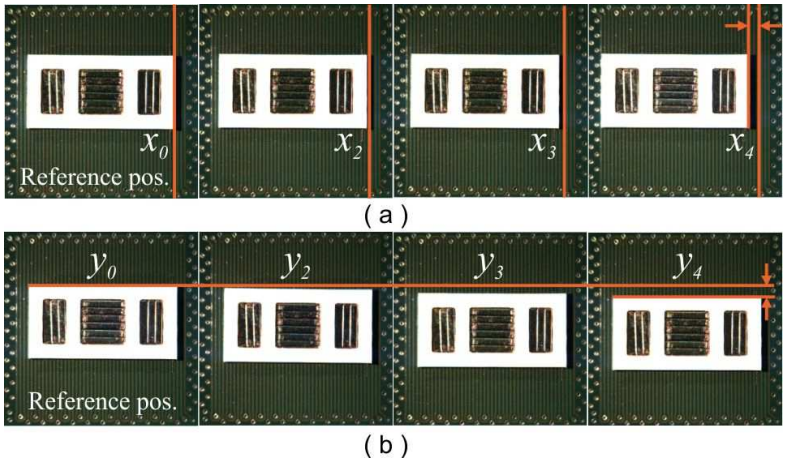

Figure 4.3 2D motion of the actuator (a) motion along *x*-axis (b) motion along y- axis

Different positions of the pallet during motion are presented where x_0 and y_0 are the reference positions along *x*- and *y*- axes, respectively. x_4 and y_4 represents the final positions after 2 mm displacement along *x*- and *y*- axes respectively. In order to calculate the mover displacement, an image processing algorithm has been developed in MATLAB software. This algorithm treats one image at a time and computes the position of the mover. The total displacement is then calculated by combining the positions from all the images. The method and process used in the algorithm are explained by demonstrating a flowchart shown in Figure 4.4.

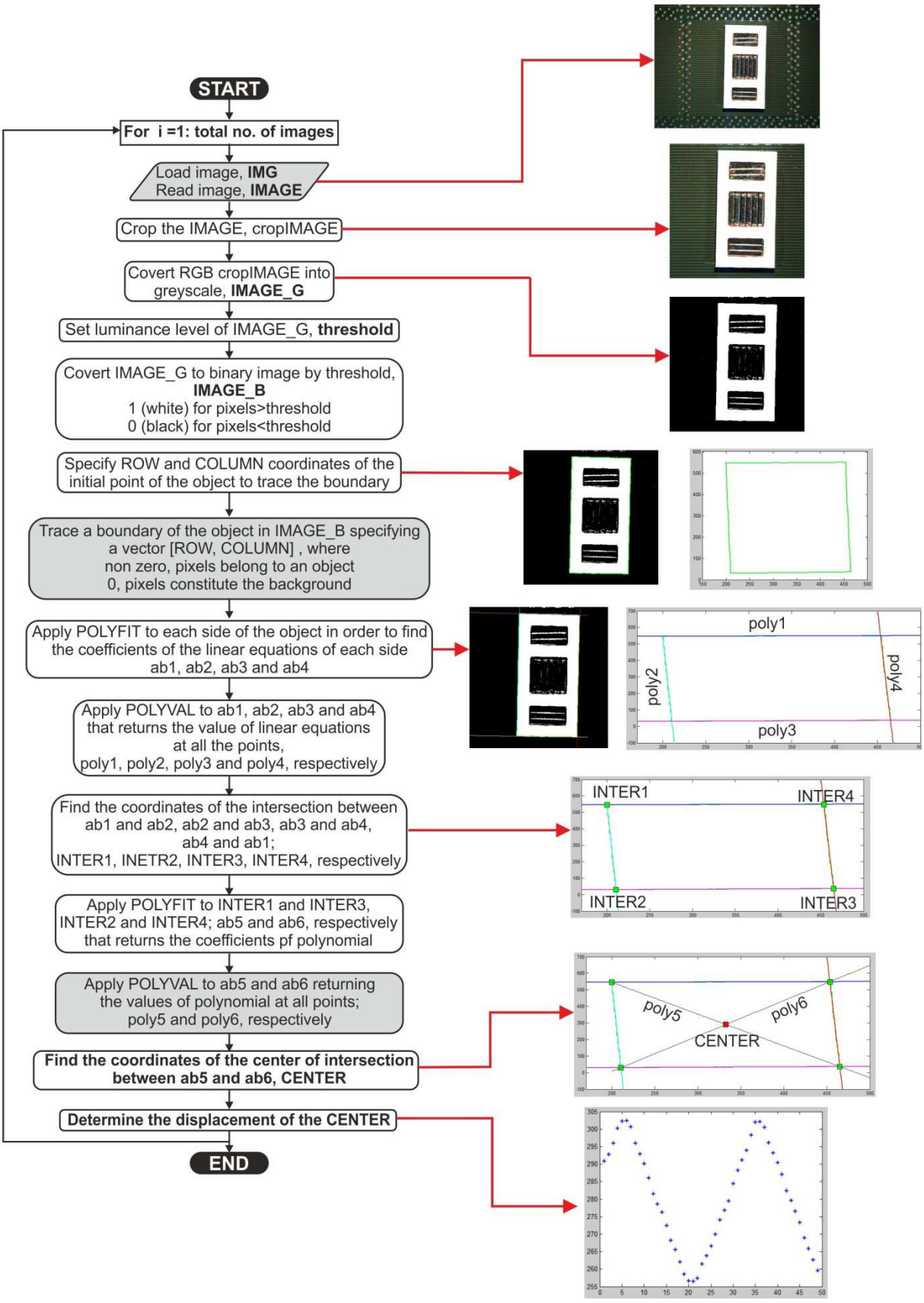

Figure 4.4 Flowchart of algorithm to measure displacement of 2D actuator

Steps involved in the algorithm

Take original image

Crop the original image to process the desired area.

The image is cropped to reduce the processing area of the image and to reduce the number of objects to be treated in the image. This will reduce the processing time of the image.

Convert image to grey scale.

It is easier to find the transition from black to white or white to black to identify the desired object.

Convert the grayscale image to binary image.

A threshold value is set which gives values of 1 (white) for all pixels in the input image with greater than the threshold and 0 (black) for all other pixels.

Trace boundary around the object (rectangle) in the image.

Initial coordinates [ROW, COLUMN] of the object are specified to identify the transition from black (0, constitutes to the background) to white (1, belongs to the object). It ensures to identify the object by drawing a boundary around it.

Find the centre of the object (rectangle).

Centre of the object is determined to trace the motion of the object. Firstly, polynomial equations of four sides of the object (rectangle) are determined. Using these equations, intersections points of four corners of the object (rectangle) are found. The intersections coordinates are then used to find the polynomial equations of the two diagonals of the object (rectangle). Hence, the intersection point of the two diagonals is obtained which is the centre of the object (rectangle).

Compute the displacement of the object (rectangle) using images taken during motion.

Centre of the desired object (rectangle) is calculated in all the images and accumulated to compute the total displacement of the object.

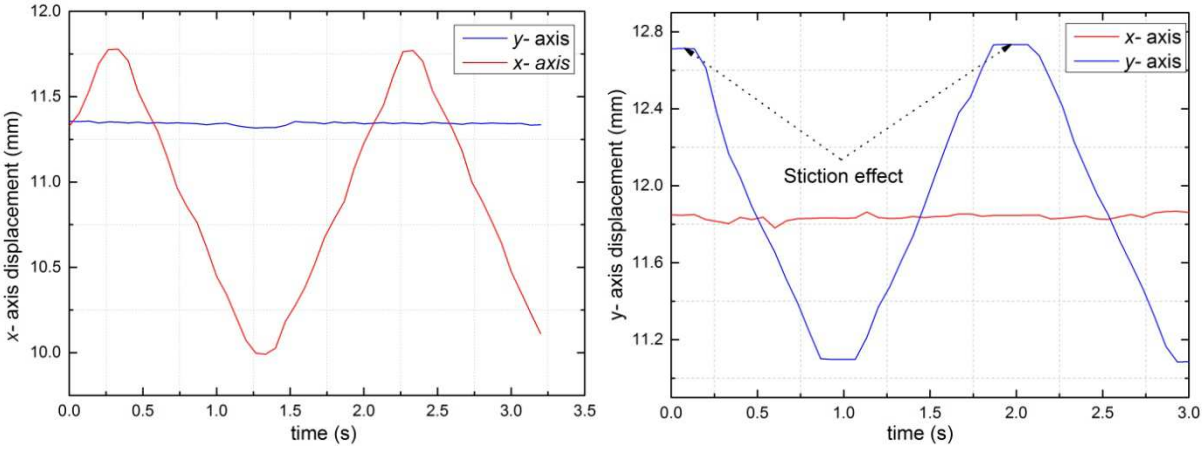

(a) **(b)**

Figure 4.5 Linear displacements (a) along *x*- axis (b) along *y*- axis

Several images were taken with the high resolution camera with the image acquisition frequency of 15 images per second. The size of each image is 1024 × 768 pixels. The resolution of each pixel is found to be 39 µm. Two periods of 1 Hz sinusoidal currents (I1, I2) of amplitude 0.6 A are supplied in order to perform motions along *x*- axis. Here, the displacement results are shown for back and forth motion with the velocity of 2 mm/s (Figure 4.5). For the motion along *x*- axis, the actuator exhibits a straightness error of 9 µm with a guidance current (constant currents) of 0.3 A along *y*- axis. The total displacement measured in this case is 1.8 mm (Figure 4.5 (a)). The difference between the theoretical displacement (2.0 mm) and the real displacement (1.8 mm) is 0.20 mm which is due to the friction loss. This phenomenon occurs due to adhesion effects which have also been observed in the MPS system developed in the previous works [KHAN 2014]. Similarly, along *y* -axis, the guidance current of 0.3 A along *x*- axis has been supplied. The straightness error along *x*- axis for *y*-axis motion is found to be 16 µm which is higher as compared to the straightness along *y*- axis for *x*- axis motion (9 µm). It could be due to electromagnetic forces generated by Layer 2 introduce higher disturbance due to heating that leads to higher straightness error. The total measured displacement along *y*- axis is 1.65 mm which makes the friction loss of 0.35 mm. The friction loss is also higher in case of *y*- axis motion compared to *x*-axis motion (0.20 mm). However, this effect is not really visible in *x*- axis displacement. This could occur due to higher distance between the PEDCs in Layer 2 and the PMAs compared to the distance between the PEDCs in Layer 1 and the PMAs. This causes low generation of forces along *y*-axis motion. Higher distance in Layer 2 could generate lower electromagnetic force or might create motion disturbance.

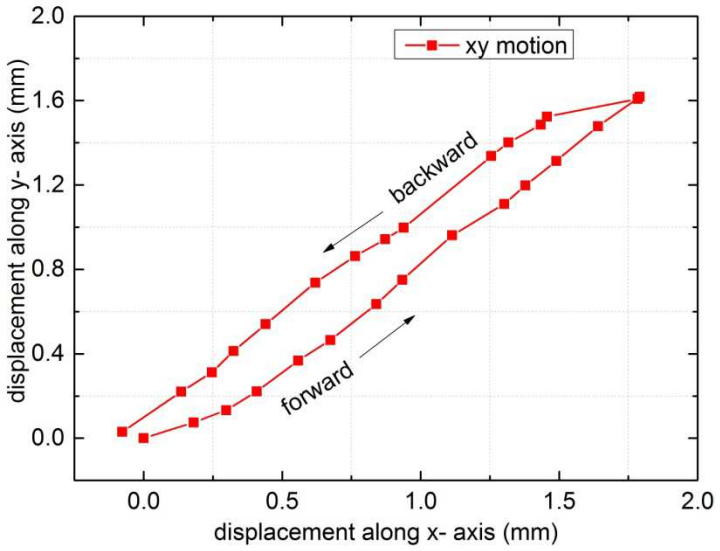

Figure 4.6 Motion of 2D actuator along xy- axis

Further, planar motions have been carried out by injecting two sinusoidal currents with 0.6 A to perform back and forth in open loop. One period of 2Hz sinusoidal currents are supplied. The coupled displacement curve of *xy*- motion can be seen in Figure 4.6. A deviation of the mover can be observed in the backward motion compared to the forward motion. This hysteresis could be due to the occurrence of different torques along the axis which could be caused by the assembly and manufacturing errors. Also occurrence of adhesion effect along the axis could contribute to the drift. In this case, the hysteresis in *xy*- plane is found to be 190 µm. Linearity error in both forward and backward motion has found to be higher than 1%. These errors can be minimized by injecting current in Layer 1 with the factor of 0.538 of current in Layer 2 (equation 3.4) in order to generate equal forces. The error can be further minimized by reducing assembly errors and also by introducing feedback control to minimize the trajectory deviation in real time..

4.1.3 **SEC platform**

After analyzing one cell of the SEC platform, motion characteristics (as different motion trajectories, straightness, repeatability etc.) of the whole SEC platform have been analyzed by performing long displacements of silicon pallet on the entire platform surface. The image processing algorithm has been adapted to measure the moving silicon pallet displacement on the SEC surface. Motions across transition zones have also been analyzed along *x*-, *y*- and *xy*- axes. Rotation have been performed and discussed in this section. Different ways of connections of the cells in order to reduce control signals and also to perform different motion trajectories have finally been studied.

4.1.4 **Experimental set up**

The experimental set up has been realized in order to test the motion performances. Firstly, the silicon pallet has been assembled. For that, four thin glass layers (130 ± 10 µm thicknesses) are glued to the bottom side of the silicon pallet below each PMA. These glass layers act as insulation layers between the PMAs and the PCB and as a reduction of friction which occurs due to mechanical contact and hence, assures smooth motion of the pallet.

In order to control each cell of the SEC surface, a separate circuit module has been designed to facilitate the routing and connections between the different cells. Five connecting PCBs, one for each column of the SEC PCB, have been designed and fabricated (Figure 4.7). Each connecting PCB is composed of five 8-pin connectors, each dedicated to a cell of the column to which the PCB is connected. Out of eight pins of each connector, 4 pins are dedicated to the two PEDCs in Layer 1 and the rest 4 pins are dedicated to the two PEDCs in Layer 2. The connecting PCB and the SEC PCB are connected using bus wires. As it can be seen in Figure 4.7, a connecting PCB is shown to connect Column 1 of SEC platform PCB. It has five connectors for the cells, A1, B1, C1, D1 and E1. Similar connecting PCBs are used to control the four other columns of the SEC PCB. In this way, each cell in Layer 1 and 2 of the SEC surface can be independently controlled. The whole SEC platform set up with all the circuit modules for routing and connections dedicated to each column of the SEC platform are shown in Figure 4.8.

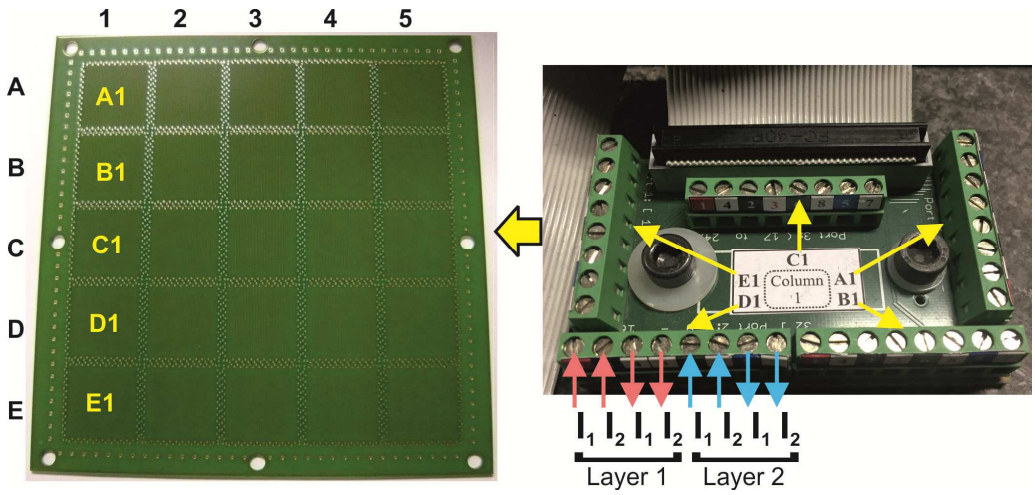

Figure 4.7 Connecting PCB for Column 1 of the SEC platform

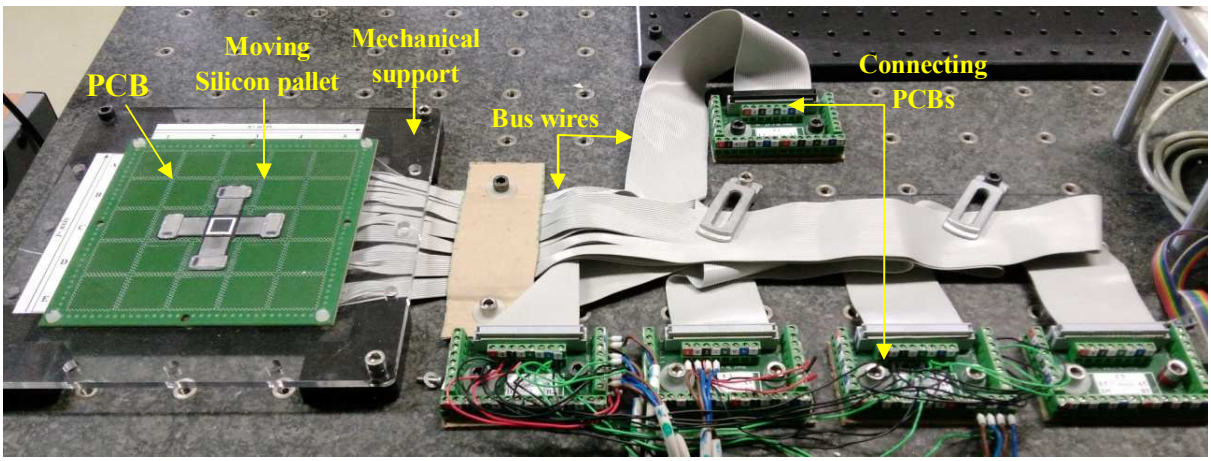

Figure 4.8 Experimental setup of the SEC platform with circuit modules for routing and connections

The four layer PCB has been mounted on a table using a mechanical support fabricated with PMMA material using laser cutting machine. Like for the previous prototype, a Labview interface, a NI PCI-6733 data acquisition board and voltage-to-current converters (input [-10V, 10V], output [-3A, +3A], bandwidth of 50 KHz) are used to control the device. The current signals generated by the voltage-to-current converters are injected into each cell of the SEC PCB thanks to the five connecting PCBs. Two voltages are generated for the displacement along an axis in each cell. The voltage-to-current converters that are used have been developed at the Service Electronique of UTC. The load that can be connected at one output is limited to 2.0 ohms. If a higher resistance is used, the linear behavior of the voltage-to-current converters is lost. The resistance of each coil of the SEC PCB has then been measured and varies between 1.8 ohms to 2.0 ohms. The maximal measured resistance corresponds to the maximum allowable value, the linear behavior of the voltage-to-current converters should then be kept for all the current range. The variation in resistance observed is due to fabrication variability of the PCB.

A high resolution camera (PointGrey Grasshopper 3) has been installed above the PCB in order to capture images of the platform during the functioning. The images taken by the camera are used to measure the displacement travelled by the pallet using image processing algorithm. The algorithm has been adapted to measure the pallet displacement which is described in the next section in detail.

4.1.5 **Image processing algorithm**

In order to measure the displacement of silicon pallet on the SEC platform, the previous image processing algorithm is modified to adapt to the images of the mover which is the silicon cross structure pallet. Due to the complicated design and large size of the silicon pallet, a black sticker in a square shape of dimensions 10×10 mm^2 has been placed at the center on the top side of the pallet in order to facilitate the position measurement. The position of the black square is tracked using image processing algorithm presented in the flowchart given in Figure 4.9.

A bigger field of view is required for displacement measurement. It is challenging to measure displacement precisely due to lot of variations in the images such as change in resolution, blurredness in images (especially during motion of the pallet), change in calculated area of the desired object etc. These variations come from the fact that the physical conditions such as external lights available, room lights, camera limitations (sensitivity, resolution etc.) given where the experiments are performed are not well adapted to the size of the pallet and motion range. In order to study these variations, an analysis has been done in order to find out how much the limitation of the given equipments and physical conditions affect the measurement precision and what are the scopes of improving it in future works. The analysis is presented in Annex B.

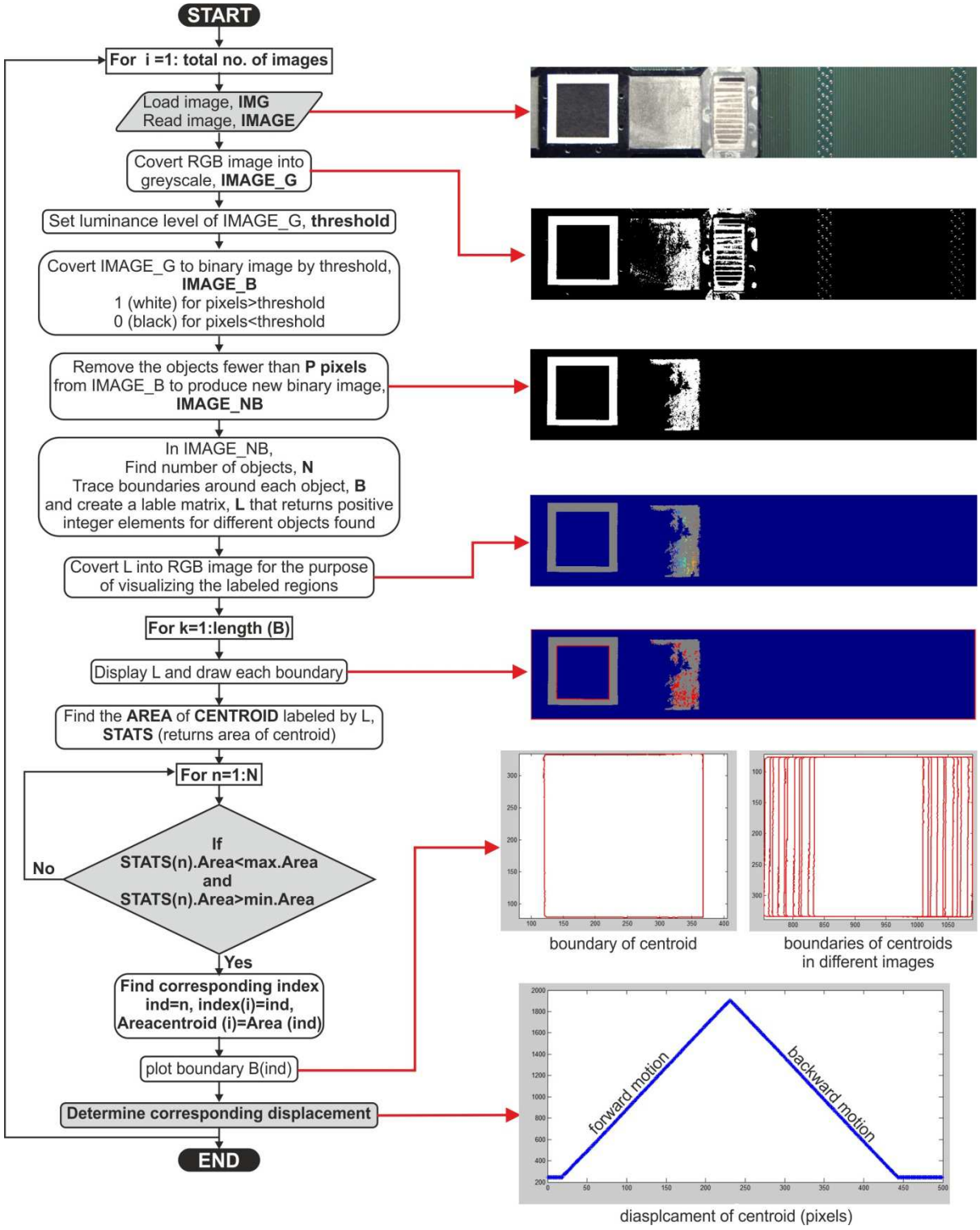

Figure 4.9 Flowchart of image processing algorithm to measure displacement of the SEC platform

Steps involved in the algorithm

Take original image.

The original image acquired from the image acquisition interface of the camera is already cropped to the desired view and motion range. This facilitates in faster image processing due to smaller size and lesser objects on the image.

Convert image to grey scale.

It is easier to find the transition from black to white or white to black to identify the desired object.

Convert the grayscale image to binary image.

A threshold value is set which gives values of 1 (white) for all pixels in the input image with greater than the threshold and 0 (black) for all other pixels.

Give the limit of pixels (P) to remove all the objects less than P pixels.

Set the value P pixels and removes all the connected objects that have fewer than P pixels, producing a new cleaner looking binary image. Hence, less number of objects are left to be processed which makes it easier to find one desired object (black square).

Trace boundaries around all the objects left in the image.

Create boundaries around all the objects in the image, find number of objects and form a label matrix that contains positive integer elements of the contagious regions. Then measure a set of properties of each labeled region in the label matrix . Positive integer elements of label matrix correspond to different regions. For example, the set of elements of L equal to 1 correspond to region 1; the set of elements of L equal to 2 corresponds to region 2; and so on. This is done to identify different objects in the image.

Convert labeled matrix (L) into RGB image and draw boundaries.

The labeled matrix L is converted into RGB image for the purpose of visualizing the different objects and boundaries around them.

Calculate area of the desired object (black square).

Area of the desired object (black square) in the image has been calculated. Due to the blurredness in the images an interval of the calculated area is specified in pixels to obtain the desired object (see Annex A for more explanation). If the pixels of the area lie in the given interval, it returns the index of the desired object.

Computes centroid of the desired object (black square) in pixels.

Coordinates of centroid of the desired object (black square) are then computed to track the position of the object.

The steps are repeated for all the images and the position of centroid in all images is then accumulated to compute the total displacement.

4.1.6 Connections to perform planar motions

In this work, long displacements of the pallet have been performed along *x*-, *y*- and *xy*- axis. For each axis, the connections between the voltage-to-current converters and the connected PCB have been established due to the limited number of available voltage-to-currents converters in the laboratory. Due to this limitation, only some cells of the SEC platform have been supplied depending on position of the pallet on the SEC PCB and desired stroke.

In order to reduce the number of voltage-to-current converters, both series and parallel connections of the cells are considered. However, series connections of the cells would make the resistance of the coils much higher. If three cells are serially connected, the equivalent resistance would be 8 ohms in the worst case. This value is very much higher than the maximal allowable load; this configuration is then not possible. Therefore, parallel connections have been done. If three cells are connected in parallel, the equivalent resistance becomes 0.6 ohms. In this configuration, if a 0.4 A is needed in each coil for motion, a current of 1.2 A should be generated by the voltage-to-current converter which gets divided equally into the three coils. Guidance function has also been introduced where a constant current is injected in order to improve the straightness error.

Connections between the cells are done in such a way so that two opposite PMAs that are used for the displacement (along *x*- or *y*- axis) are able to cross at least two transition zones which make the minimum displacement stroke of 50 mm in each axis. That means two opposite PMAs will pass over three cells. Hence, six cells are required to be active for each axis displacement. Instead of connecting six cells in parallel, connections are divided in two to make each connection for three cells. This is done to avoid too low resistance of the coils and also the range of voltage to current converter used in this work is limited to [-3A, +3A]. If more cells are connected in parallel, higher amplitude of currents are required to fulfill the nominal current requirement of each coil.

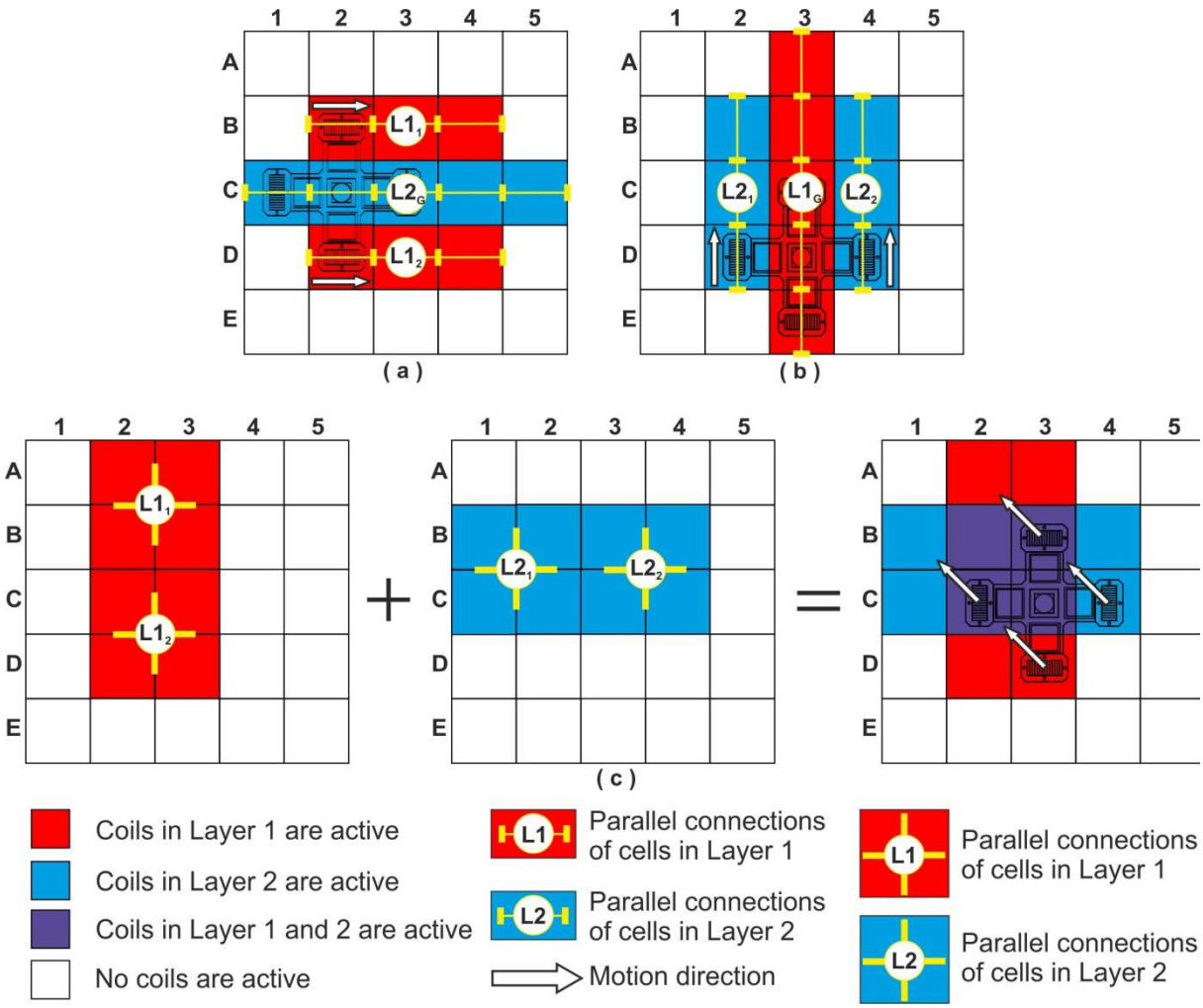

Figure 4.10 Connections for different cells for long stroke planar motions (a) connections for displacement along *x*- axis (b) connections for displacement along *y*- axis (c) connections for displacement along *xy*- axis

In Figure 4.10 (a), the connections for the translation along *x*- axis with guidance function are presented. A parallel connection, represented by $L1_1$ (in Layer 1), is done for the three cells B2, B3 and B4. Similarly, $L1_2$ represents the parallel connection between the cells D2, D3 and D4. These two connections allow long displacement of the pallet along *x*- axis. With these two pairs of three cells, long displacement strokes have been realized and the behavior of the pallet has been observed when it passes over two transition zones between the cells. During this motion along three cells, the two PMAs used for the guidance function move over five cells of the platform (C1, C2, C3, C4 and C5). $L2_G$ represents the parallel connection of these five cells in Layer 2 (*y*- axis) in order to obtain a guidance function. Similarly, Figure 4.10 (b) shows the connections in order to perform long displacements along *y*- axis with a guidance function. Two connections $L2_1$ and $L2_2$ have been done to allow the pallet displacement along *y*- axis, each connecting three cells B2, C2, D2 and B4, C4, D4, respectively. The third

parallel connection $L1_G$ is for the guidance function and connects the five motors A3, B3, C3, D3 and E3 in layer 1 (*x*- axis).

Furthermore, connections for the planar motions are shown in Figure 4.10(c). In this configuration, the activation of cells for motion along both *x*- and *y*- axis is needed. These connections are complex as trajectory of the pallet has to be analyzed in advance in order to determine the cells moving pallet would cross. This will help in deciding the connections of the corresponding cells in Layer 1 and Layer 2. During the presented planar motion, the PMA of the moving pallet would cross over the vias fabricated on the platform which is the junction of four cells. It means all the corresponding four cells would be activated to cross one junction of the cells. Therefore, to cross over one junction, the pallet would travel 30 mm. The considered configuration is for 30 mm stroke along *xy*- axis. $L1_1$ and $L1_2$, each represents the parallel connections between four cells in Layer 1: A2, A3, B2, B3 and C2, C3, D2, D3, respectively. Similarly, parallel connections between four cells in Layer 2 are represented by $L2_1$ and $L2_2$. $L2_1$ shows the connection for four cells: B1, B2, C1 and C2 and $L2_2$ show the connections for the cells B3, B4, C3 and C4.

The abovementioned connections for each axes (x-, y- and xy- axes) are realized to perform long displacements in order to characterize performance of the SEC platform in open loop control which is described in the next section.

4.1.7 Performance of the SEC platform in open loop control

Firstly, long stroke displacements along two axes i.e. *x*- and *y*- axes are realized in order to validate the ability of the actuator to realize long displacements and to pass over the transition zones located between the cells. Then, *xy* linear motion profile has been realized and discussed. Rotation has been performed to find out the maximum rotation angle possible on the platform. Further, performance characterization as straightness and position repeatability has been done. And lastly, performance comparison of coupled de-coupled motion is performed.

4.1.7.1 Linear displacements

The ability of the actuator to realize long stroke displacement along *x*-, *y*- and *xy*- axes has been tested. Firstly, the experiments have been performed in order to obtain the maximum stroke possible as per the connections shown in Figure 4.10(a) for the *x*- axis motion. Displacements along *x*- axis have been obtained using nominal current value, 0.4 A with the actuation speed of 8 mm/s. The experiments have been performed with the guidance function

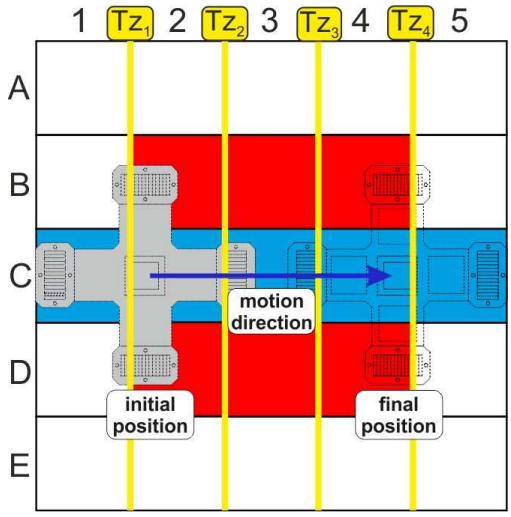

Figure 4.11Maximum motion range of pallet over SEC platform

i.e. constant currents of 0.4A are injected along *y*- axis. Single displacement cycle (i.e. forward and backward motion) has been performed. At first, 34 periods of 4Hz sinusoidal currents of 0.4 A per coil are injected in the required PEDCs of Layer 1.

In this experiment, the two opposite PMAs that displace the pallet are placed on the transition gap (Tz_1) at initial position (Figure 4.11). The PMAs cross two transition gaps, Tz_2 and Tz_3 (three cells) and the final position reaches at the transition gap, Tz_4.

Images have been captured by the camera during the functioning of the conveyor and the displacement has been measured using image processing algorithm mentioned earlier. From

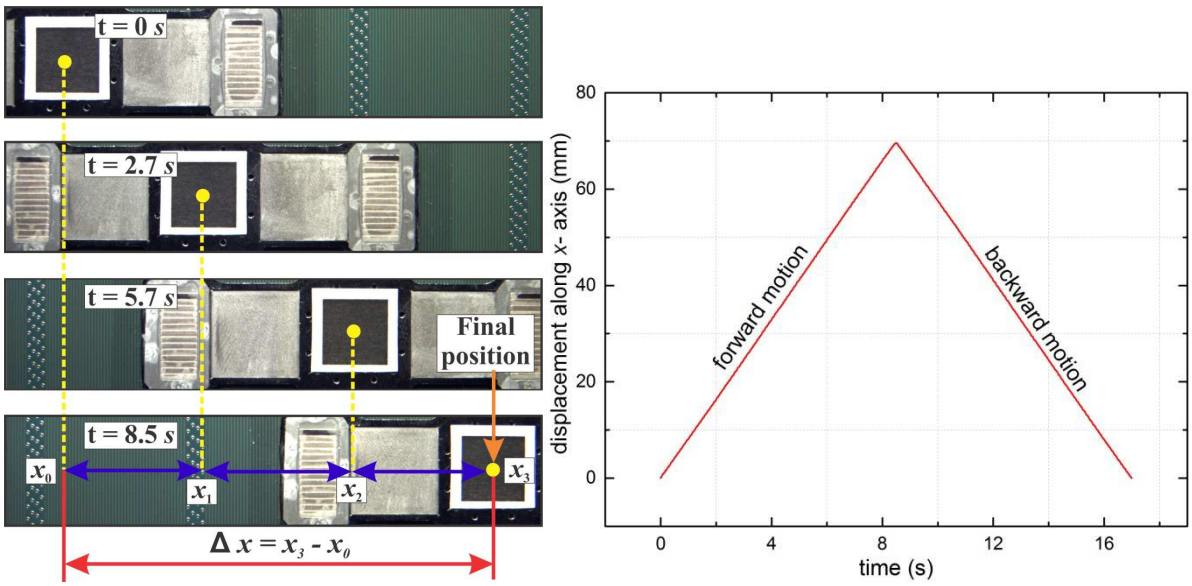

(a) **(b)**

Figure 4.12 Motion along *x*- axis (a) Images taken to compute displacement (b) displacement measured along *x*- axis

the images, the image resolution has been computed and is equal to 42 µm (1 pixel) using the same target used in the previous images for 2D actuator. Several images have been acquired for each axis with a time delay of 0.04 s between two images. The Figure 4.12 (a) represents images taken by the camera along *x*- axis motion. Different positions of the pallet are shown where x_0 is the initial position at time, t = 0 s. The pallet is placed over the transition zone Tz_1 at the initial position. At t = 2.7 s, the black square on the pallet is at the transition zone Tz_2. It reaches at transition zone Tz_3 at t = 5.7 s. The final position is at x_3 at time, t = 8.5 s. The total displacement measured, $\Delta x = x_3 - x_0$ is 69.5 mm. The displacement curve is presented in Figure 4.12 (b). This is the maximum displacement stroke possible with the aforementioned connections of the cells (Figure 4.10 (a)) for *x*- axis motion. The straightness error along *y*-axis for *x*- axis motion is found to be 14 µm which is quite low for long stroke motion.

For the performance analysis of linear displacement, 25 periods of 4 Hz are used in order to reduce the displacement stroke to 50 mm. This has been done to avoid the initial position of the moving pallet at Tz1 which might create some changes in the motion behavior. Some kind of interruptions or behavior changes can occur due to the presence of non active PEDCs under few PMs at the initial and final positions. By reducing the stroke, the initial position of the moving pallet is placed inside the cell C2 and the final position would be inside the cell C4 instead of the transition zone Tz4 (Figure 4.13). In order to observe the difference clearly, an analysis has been performed which is presented in the next sections where analysis on the straightness is presented.

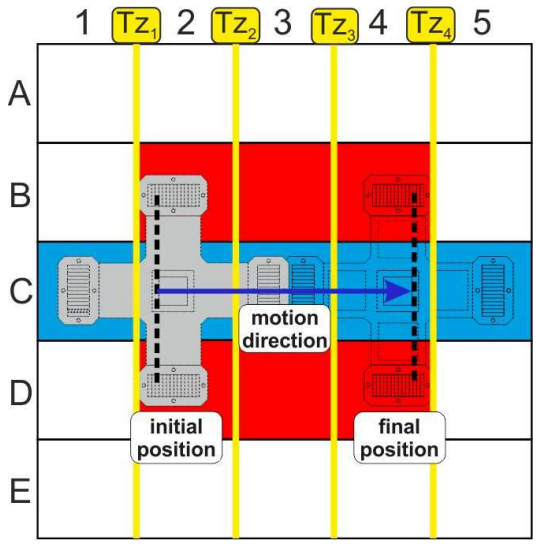

Figure 4.13 Nominal motion range of pallet over the SEC platform

For the displacement along *x*- axis, 25 periods of 2 Hz sinusoidal currents (I1, I2) with 1.2 A amplitude are supplied to the PEDCs (0.4 A per PEDC) in Layer 1 to perform forward and backward motion along *x*- axis displacement with the velocity of 8 mm/s. Two constant currents (I1, I2) of 0.4 A per PEDC are injected in Layer 2 for guidance. The sampling frequency of the injected currents is 100 Hz. Several images were taken with the high resolution camera and the pallet displacement is measured using the image processing.

Theoretically, a half period of 2 Hz sinusoidal injected signal should generate a 1 mm displacement of the pallet. In this case, 25 periods of 4 Hz are supplied; a 50 mm displacement should then be obtained. However, the measured displacement is 50.48 mm which is higher than the theoretical displacement (Figure 4.14). The difference could be due to the sliding of the pallet that occurs when the displacement direction of the pallet changes.

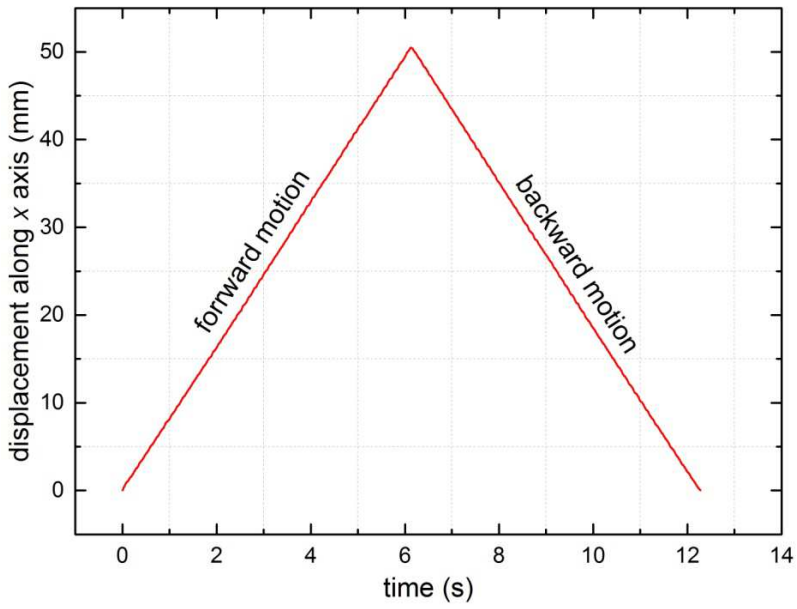

Figure 4.14 50 mm back and forth motion along x- axis

Similar curve has been obtained for forward and backward displacement performed along *y*-axis with the velocity of 8 mm/s. 0.74 A of sinusoidal current per coil is supplied to the PEDCs in Layer 2. For the guidance function, two constant currents of 0.2 A per PEDC is supplied to Layer 1. The experimental displacement is found to be 51.5 mm. The two curves for *x*- and *y*- axis motion are presented in Figure 4.15. The pallet travels almost 1 mm more along *y*- axis than along *x*- axis. Also, the time delay to travel equal motion is slightly higher along *y*- axis than along *x*- axis. And also, stiction effect can be seen during motion along *y*-axis when the direction of motion is changed (Figure 4.15 (b)). The difference between the two curves could be due to assembly errors, thickness of the coils that may interfere with the

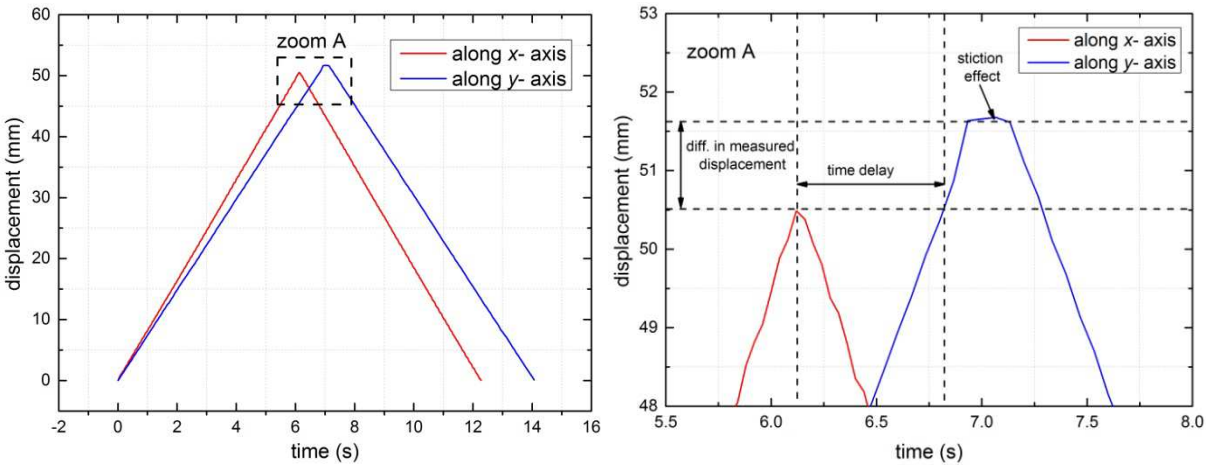

(a) (b)

Figure 4.16 Linear displacements (a) Comparison between displacement along x- axis and y- axis (b) zoom view of displacement curves

edges of glass layers during the motion along x- axis and also, the coefficient of friction have been considered to be homogenous on the whole surface in this study but it may not be the case in reality.

The abovementioned observations in the linear motion behavior along the two axes occur due to design and assembly of the pallet and the SEC platform. The edges of four thin glass layers glued underneath the pallet can interfere with the edges of conductors on the top side of the PCB when a displacement along *x*- axis is performed (not for y-axis) and hence, creates friction. However, this is not the case when the pallet travels along *y*- axis. This difference in functioning along the two axes could be due to possible errors such as assembly errors, errors in theoretical PCB dimensions (distance between the layers), coils dimensions error, non homogeneous friction etc. All these differences introduce the observed differences for the

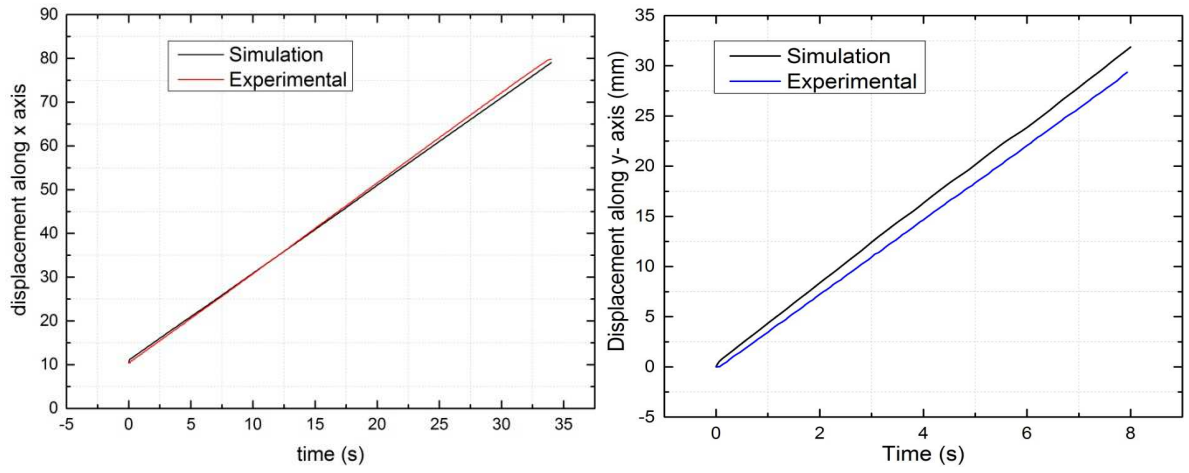

Figure 4.15 Comparison between simulation and experimental results (a) motion along *x*- axis (b) motion along *y*- axis

displacement along *x*- and *y*- axis.

Comparison between simulation and experimental displacements along *x*- and *y*- axis is shown in Figure 4.16. One transition zone the pallet would cross is considered to compare experimental and simulation results. For that, 16 and a half periods of 1 Hz (along *x*- axis) and 2 Hz (along *y*- axis) sinusoidal currents (0.4 A for *x*- axis and 0.74 A for *y*- axis) are injected to perform 33 mm theoretical displacement stroke. The displacements along *x*- axis and *y*- axis are performed with the actuation speed of 2 mm/s and 4 mm/s, respectively. Higher speed performance is presented in Layer 2 as compared to Layer 1 because of the occurrence of thermal effect in the PEDCs in Layer 2 at lower speeds.

The simulated and experimentally measured displacements of the pallet along *x*- axis are found to be 32.5 mm and 32.87 mm, respectively. Along y- axis motion, the simulated and measured displacements are 32.48 mm and 29.54 mm, respectively. The experimental results are in good correlation with the simulated results for the motion along *x*- axis (Figure 4.16 (a)). However, for *y*- axis motion, the experimental curve is drifting from the simulation curve (Figure 4.16 (b)). The reason for the difference could be the assembly errors or manufacturing errors such as the thickness of the prepregs that could be different from the theoretical value given by the PCB manufacturer that introduces a force variation compared to the theoretical configuration.

4.1.7.2 Straightness

In order to study the influence of guidance function on the motion behavior, displacements have been performed without guidance and then with guidance function. Also, the straightness error has been determined with different guidance currents that help in selecting the guidance current amplitude to minimize straightness error during motion.

For that, 25 periods of 2 Hz sinusoidal currents (I1, I2) are supplied to two PEDCs in Layer 1 connected through parallel connection $L1_1$ as shown in Figure 4.10 (a). The amplitude of the currents to move the pallet is 1.2 A which gets divided into three PEDCs that are connected in parallel. This implies each PEDC is supplied with 0.4 A of current. The sampling frequency of the injected currents is 100 Hz. Simultaneously, two constant currents (I1, I2) with different amplitudes starting from 0 A to 0.5 A are injected into each PEDC in Layer 2 connected through $L2_1$ which are acting as guidance currents along *y*- axis. This is done perform displacement stroke along *x*- axis with the velocity of 8 mm/s and straightness error is computed in function of different guidance current values.

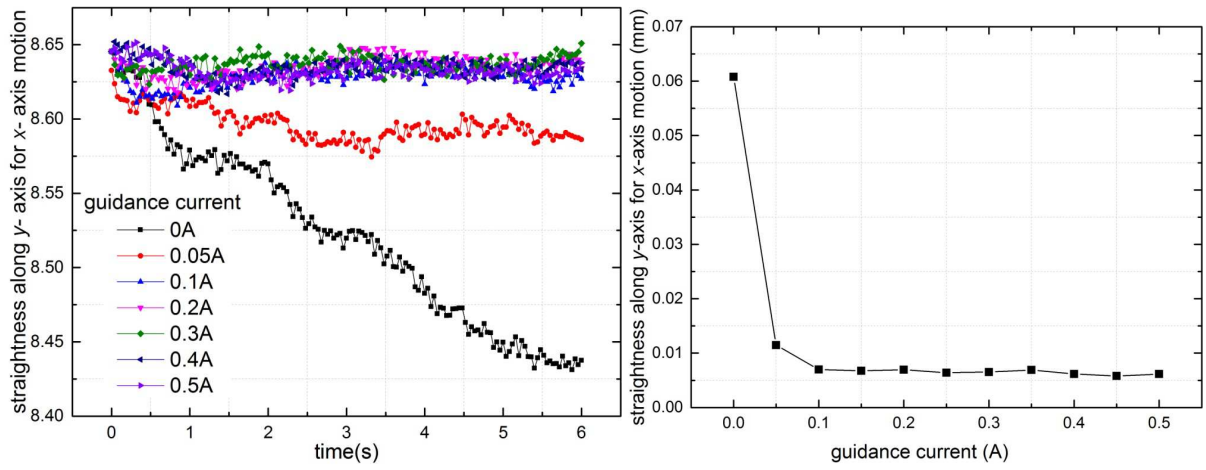

(a) **(b)**

Figure 4.17 Straightness along y- axis for x- axis motion (a) straightness curves with different guidance current amplitudes (b) straightness error with different guidance current amplitudes

In Figure 4.17 (a), *y*- axis straightness curve for *x*- axis motion with different guidance currents from 0 A to 0.5 A can be seen. When no guidance current is supplied (0 A), the drift due to the straightness error is the highest. As the guidance current is increased, the drift is getting smaller and the straightness error is decreased. When the guidance current is higher than 0.2 A, all the straightness curves are equally straight. Figure 4.17 (b) shows the computed values of straightness error at each amplitude of guidance current. At 0 A of guidance current, the straightness error is found to be 65 µm which is decreased to 10 µm at 0.05 A. It further decreased to 6 to 7 µm for higher amplitudes of current between 0.2 A to 0.5 A and then, remains almost constant.

It has been observed that in the previous results of 68 mm displacement stroke, the straightness error obtained was 14 µm with 0.4 A guidance current which is reduced to 7 µm when 50 mm stroke is performed. This happened due to the change in the initial and final position of the PMAs that are displacing the pallet. For 68 mm stroke, the PMAs were placed at the initial position which is at the transition zone Tz_1 and it reached the final position Tz_4 after travelling 68 mm travel (see Figure 4.11). Because the adjacent cells (B1 and B5, D1 and D5) to these two transition zones are not active, the force generated at these positions is low because some PMs of the PMAs are not placed on the active conductors. Therefore, the stroke is reduced to 50 mm where the PMAs are kept inside the cells which are active (B2 and D2) and finish the travel within the active cell (B4 and D4). It improves the motion behavior and also reduces straightness error to 50 % as compared to previous results.

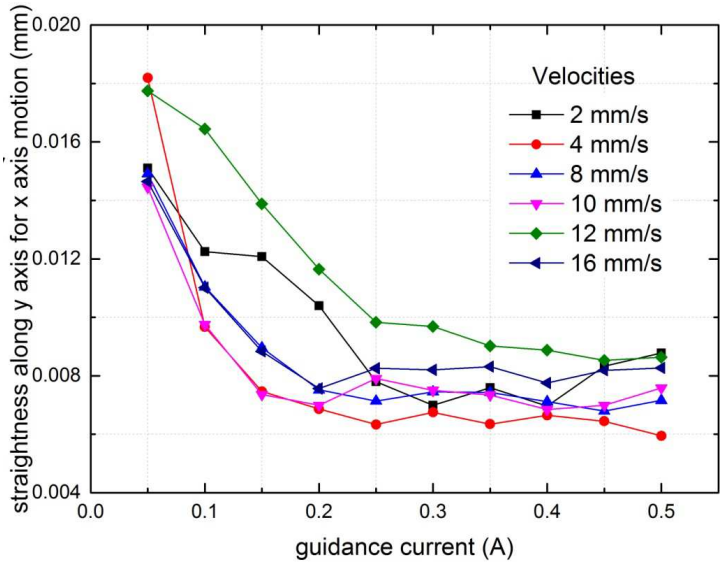

Figure 4.18 Straightness along y- axis for x- axis motion for different velocities

The influence of the motion velocity on the straightness error has also been studied for different guidance currents. The motion is realized along *x*- axis by injecting currents of amplitude 0.4 A in each coil. Figure 4.18 shows the straightness error in function of the guidance current (between 0 A and 0.5 A) for different velocities starting from 2 mm/s to 16 mm/s. With all the velocities, the straightness curve going down gradually with increasing guidance currents. It can be observed that straightness is found to be at constant value with the guidance current more than 0.3 A at each velocity. Though the computed straightness marginally varies between 6 µm to 10 µm for each velocity, it does not affect the measurement precision much.

Similar analysis is performed during motion along *y*- axis using connections of the coils in Layer 2. $L2_1$ and $L2_2$ are supplied with two sinusoidal currents (I1, I2) for the motion along *y*- axis (Figure 4.10 (b)). Simultaneously, two constant currents (I1, I2) are injected in $L1_G$ for the guidance. According to equation (3.4) given in Chapter 3 and in order to maintain equal translation forces in both the axes, two currents of 0.74 A are injected into two PEDCs for the motions along *y*- axis, 0.2 A per PEDC of guidance current in *x*- axis is used for straightness. Displacement is performed at the velocity of 8 mm/s. In this case, the straightness computed with 0 A guidance current is found to be 56 µm which is lower as compared to *x*- axis motion. Similar performances has been observed in this case where the straightness error decreases as the guidance current increases up to 0.2 A and remains almost constant for higher amplitudes. The value of straightness at 0.2 A guidance current is 16 µm which is higher as compared to the straightness computed during *x*- axis motion which is 7 µm. This shows that the

straightness along *x*- axis motion is decreasing rapidly with the increase in guidance current as compared to the straightness along *y*- axis motion.

4.1.7.3 Repeatability

The position repeatability in both the axes has been measured. In order to do that, a 35 cycle test has been performed with the same parameters as discussed in the linear displacement section. One cycle motion along *x*- axis is shown in Figure 4.19 where the pallet is moved form position A to position B and then back to position A. Each time, an image is taken at position A after completion of each cycle. Therefore, 35 images have been captured for 35 cycles. Standard deviation of 35 measurements at Position A has been taken to measure the

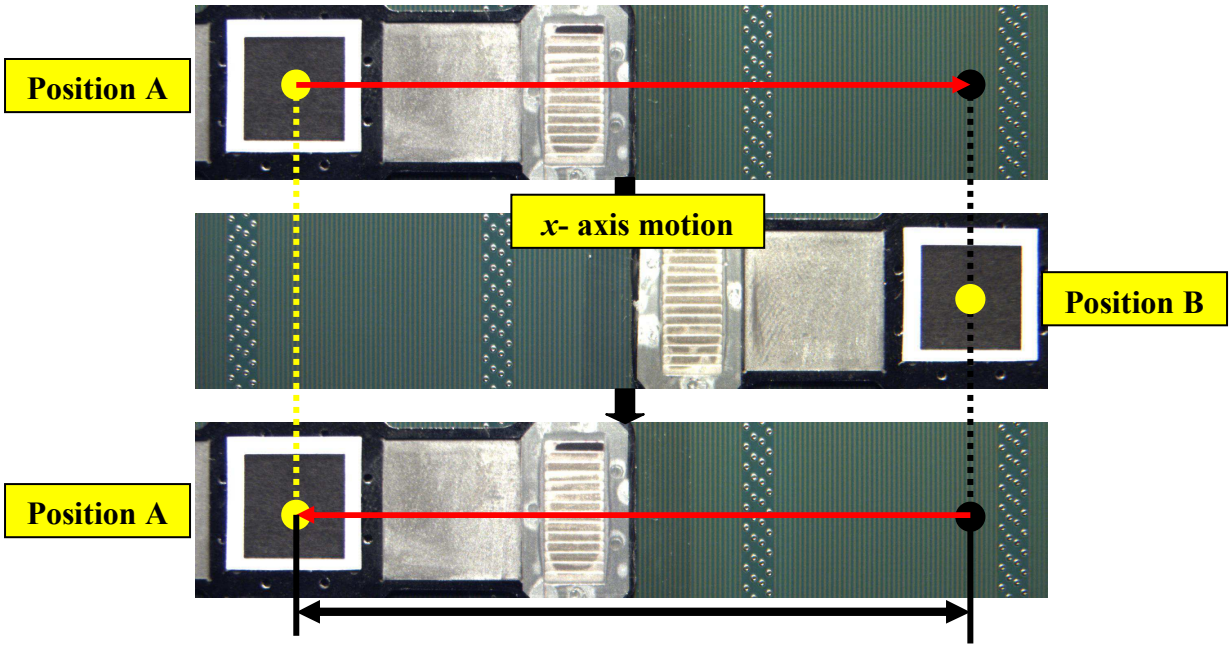

Figure 4.19 Motion demonstration to measure repeatability along *x*- axis

axial and lateral position repeatabilities for the motion along *x*- axis. Similar approach has been adapted to measure the position repeatability for the motion along *y*- axis.

In this case, a high resolution camera lens (Infinity probes) has been used fixed on the camera (PointGrey Grasshopper 3) to capture images. The image captured by the camera probe is shown in Figure 4.20(a). Each image is of size 2344 × 1972 pixels. The resolution of each pixel is 2 µm. The field of view of the camera has been focused only on a edge of the black square to reduce the limit of resolution. The images of edge corner of the black square are then only taken at each Position A. A time delay is given in the LABVIEW interface to stop the pallet at Position A before capturing an image. Then, the pallet continues for the second cycle and so on. A similar image processing algorithm that the one used for the displacement

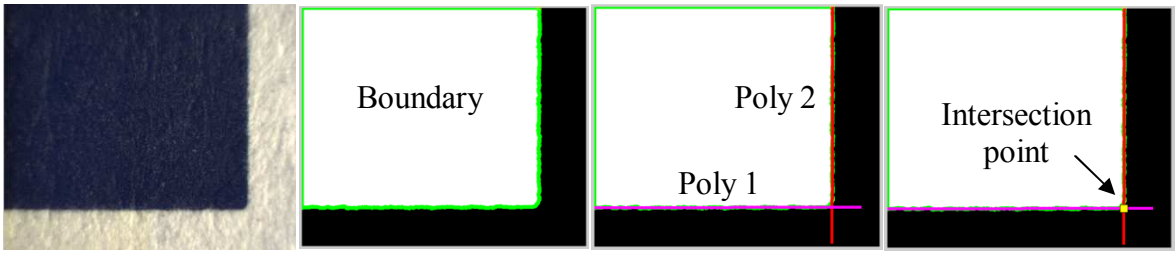

Figure 4.20 Steps to measure position repeatability (a) Original image (b) Trace boundary (c) Form polynomial equations of two sides (d) Find intersection point of two sides

measurement of 2D actuator is used to determine the intersection point of two sides of the black square of the sticker and then, the pallet position is computed.

During the experiment, 35 cycles of back and forth motions have been performed along *x*-axis and Figure 4.21 represents the axial and lateral position repeatabilities. For the mean displacement of 50.5 mm along *x*- axis, the axial and lateral position repeatability error is found to be 5.7 µm and 4.2 µm, respectively.

For y- axis motion, for the mean displacement of 51.5 mm with 20 cycles back and forth motion has been performed. Less number of cycles are performed along *y*- axis due to fast heating of PEDCs in Layer 2 of PCB. In this case, the axial position repeatability measured is 9 µm and lateral position 4.7 µm. Therefore, in both the axes, SEC platform exhibits low repeatability error in open loop which can be further reduced by introducing closed loop control.

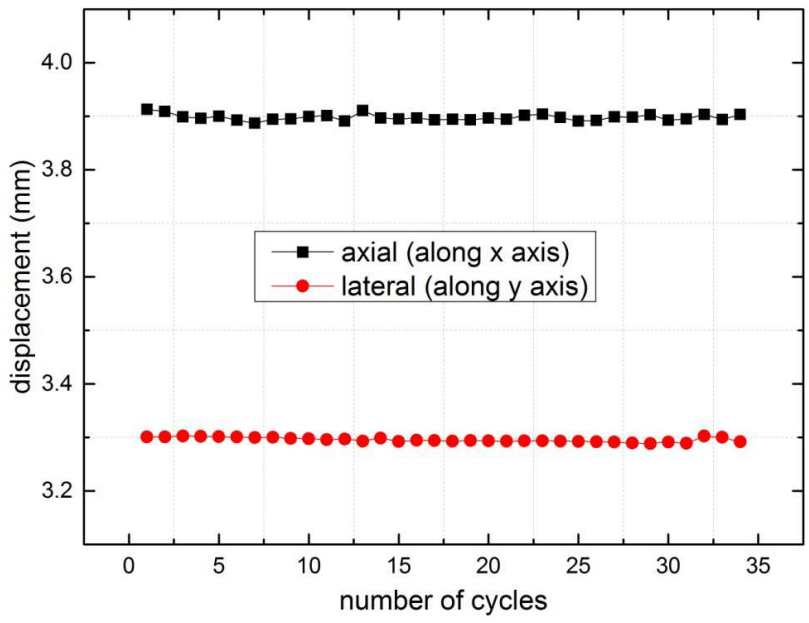

Figure 4.21 Position repeatability performed along *x*- axis

4.1.7.4 *xy*- motion profile

In this section, planar motion results are presented. Cells in layer 1 and layer 2 are connected as shown in Figure 4.10 (c) to perform planar motions. Sinusoidal currents (I1, I2) with 1.6 A amplitude are supplied to $L1_1$ and $L1_2$ each for Layer 1 (see Figure 4.10 (c)). Similarly, sinusoidal currents of amplitude 3 A are injected to $L2_1$ and $L2_2$ each in Layer 2 in order to send 0.74 A in each coil (in accordance to equation (3.4) in Chapter 3). Images have been taken during motion. The resolution of each image is 42 µm and time delay between each image is 0.05 seconds. The displacement curves (forward and backward motion) are shown in Figure 4.22 (a) for three velocity values: 4, 8 and 12 $mm.s^{-1}$. The zoom views of Position A and Position C are shown in Figure 4.22 (b) and (c), respectively. It can be observed that the trajectory is repeatable from Position A to Position C. The silicon pallet deviates in the backward motion (from Position C to Position A). This hysteresis occurs due to the appearance of torques along an axis which is caused by assembly errors. Taking into account

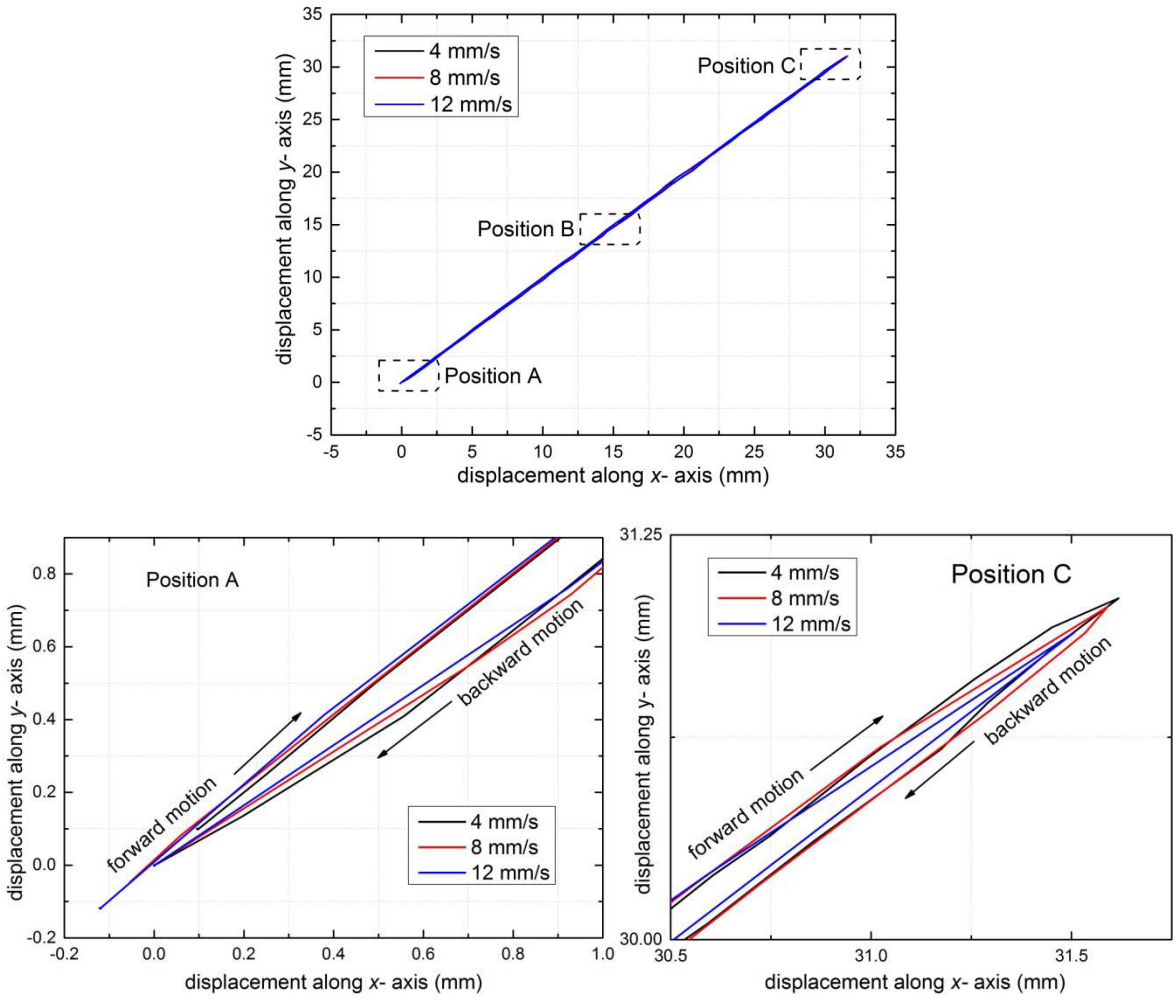

Figure 4.22 Displacements along *xy*- axis (a) Displacement curve (b) zoom view of position A (c) zoom view of position C

the drift effect during motion, the amount of hysteresis in *xy* plane is found to be 300 µm. This error can be minimized by reducing assembly errors or using a closed loop control.

Alike linear displacements, the position repeatability for *xy* motion has been computed by performing 20 cycles forward and backward motion along xy axis. Images have been taken at one position with the image resolution of 2 µm. In this configuration, the calculated repeatability error is 10 µm along xy- axis motion. It is concluded that SEC plat exhibits low repeatability along *xy*- axis in open loop. This can be further reduced by adapting feedback control in real time.

4.1.7.5 Rotation

Rotation of the pallet is performed by supplying few cells of the SEC platform. The connections for the rotations are presented in Figure 4.23. PEDCs in Layer 1 and Layer 2 are supplied in the cells B2, B4, D2 and D4 in order to perform maximum rotation possible. 0.74 A is supplied to PEDCs in Layer 2 and 0.4 A is supplied to PEDCs in Layer 1. The directions of the currents are inversed in the two opposite cells with respect to each other in order to generate forces in opposite directions which allows pallet to rotate about the center of the pallet.

The images of the pallet have been taken using a high resolution camera lens (Infinity probes)

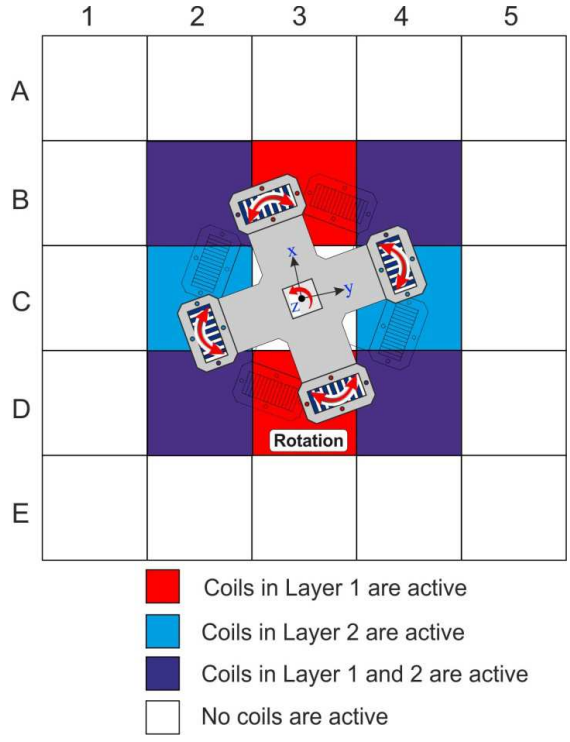

Figure 4.23 Connections to perform rotation of the pallet

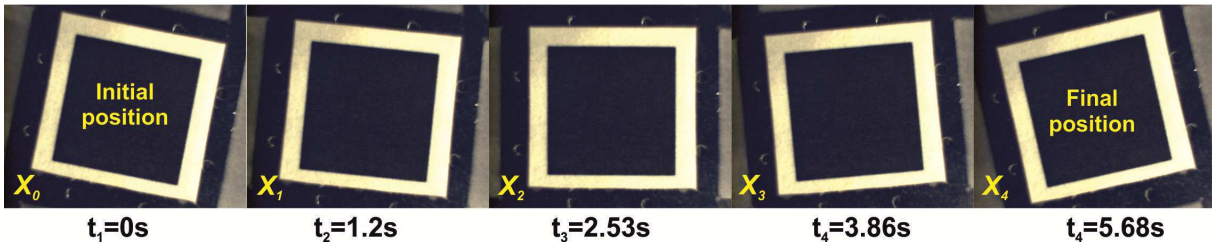

(a)

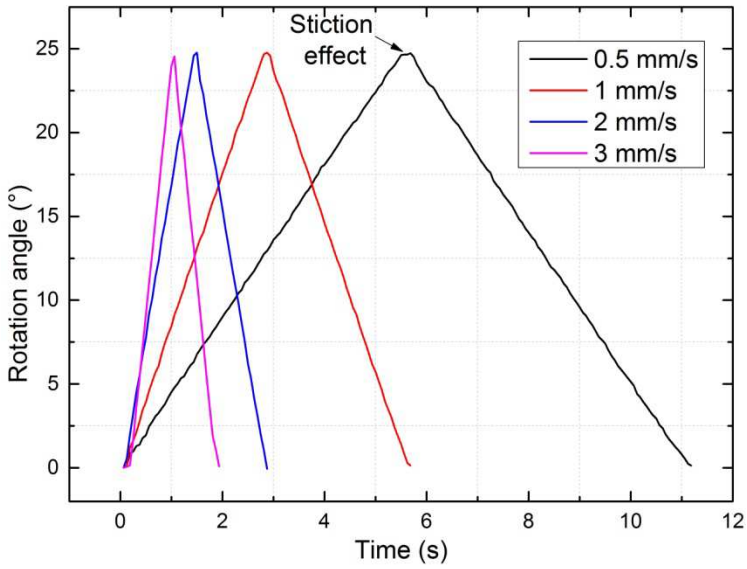

(b)

Figure 4.24 Rotation analysis (a) Images captured by the camera (c) Rotation angle at different velocities

installed on a camera (PointGrey Grasshopper 3). Several images of size 2448 × 2048 pixels are captured by the camera during motion with the time delay of 0.0625s between each image (Figure 4.24). The resolution of each pixel is measured to be 7 µm. The field of view of the camera has been focused only on the black square to reduce the limit of resolution. Using these images, an image processing algorithm has been used to measure angle of rotation of the black square. The images shown in Figure 4.24 (a) are captured with the image acquisition frequency of 16 images per second at the actuation speed of 1 mm/s at different positions during motion. x_0 is the initial position of the black square at time =0s. The final position x_5 reached at t=5.68s. The maximum measured rotation angle is 24.76°.

The rotation angles are measured on four different velocities 0.5, 1, 2 and 3 mm/s (Figure 4.24(b)). At low speed of 0.5 mm/s, stiction effect is observed that occurs when the PMAs and PEDCs are in alignment with one another. Due to this the measured angle at low velocity of 0.5 mm/s is 24.5° which is less compared to the angle measured at higher velocities. The

analysis revealed that the average maximum angle measured experimentally using three higher velocities is found to be 24.75°. The experimental range of the rotation angle is ±12.37°.

The rotation angle is limited in this case; it could be due to the geometrical limitation of the PEDCs. However, it is clearly higher than the maximum rotation angle obtained in the previous works of MPS system where the maximum rotation angle was found to be ±11° [KHAN 2014]. In order to achieve higher rotation angle or full circle rotation of 360°, redesigning and remodeling of the PEDCs would be required in future.

4.1.7.6 Coupled - decoupled motion

The application of this device is the planar conveyance in a micro-factory which is described in Chapter 2. For that, several pallets will be placed on the smart surface and will be independently controlled. However, a problematic of trajectory management will appear. For example, if a pallet has to reach a given position, different trajectories are possible and a choice has to be done considering the trajectories of the other pallets. In this section, two different trajectories of the pallet have been tested to reach a desired position (considering the same initial position) in order to compare them.

An experiment has been carried out to show the ability of the SEC platform to perform

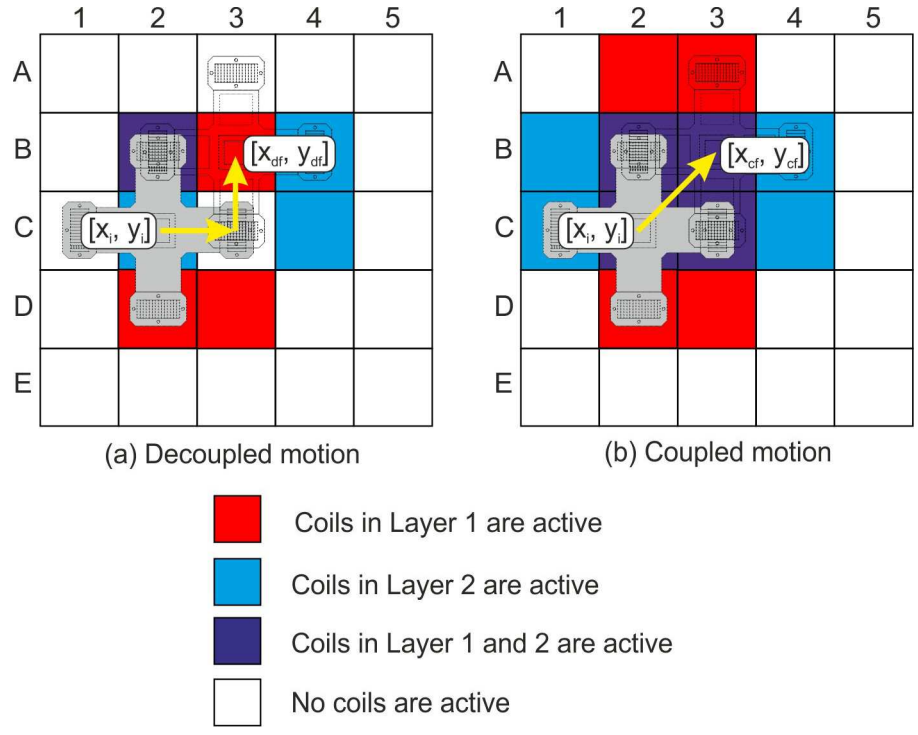

Figure 4.25 Two motion trajectories (a) de-coupled motion (b) coupled motion

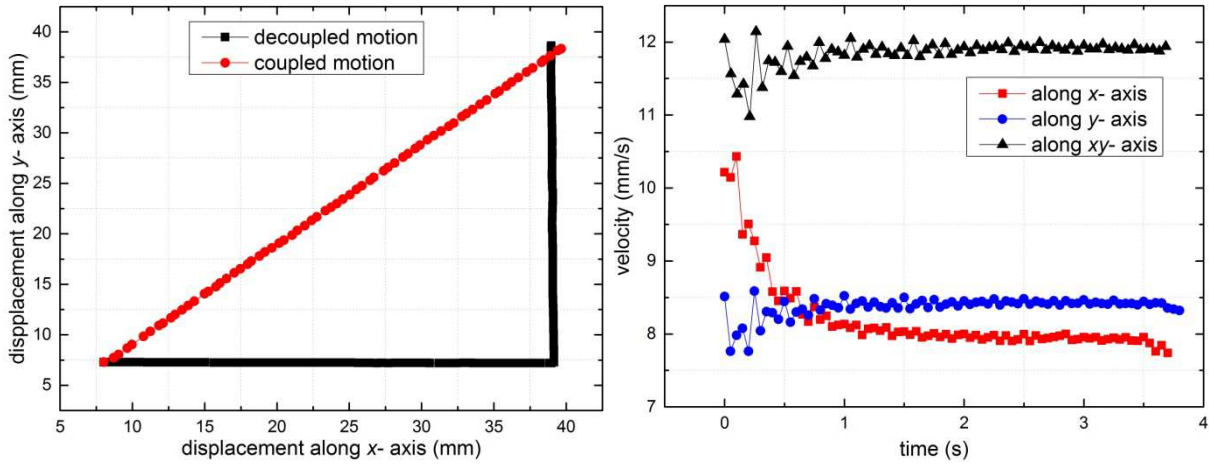

Figure 4.26 Coupled and de-coupled analysis (a) displacements (b) velocities

different trajectories to reach a desired position and also to determine the velocity in the *x*- and *y*- directions via decoupled or coupled displacement. In order to minimize the number of voltage-to-current converters, it has been decided to only cross two cells in each direction. Two types of motions are performed; decoupled and coupled motion (see Figure 4.25 (a) and (b), respectively). Same controlling parameters are used for the displacements as in the previous experiments for long displacements along *x*-, *y* and *xy*- axes. The Figure 4.25 (a) shows the two types of experimental displacements of the pallet from cell C2 to cell B3 for decoupled motion. The initial position is $[X_i, Y_i]$ = [7.30 mm ; 8.03 mm]. The final reached positions are respectively $[X_{cf} ; Y_{cf}]$ = [38.96 mm ; 38.83 mm] for the decoupled displacement and $[X_{df} ; Y_{df}]$ = [39.65 mm ; 38.33 mm] for the coupled displacement (diagonal). The travel time in the decoupled displacement and the coupled displacement are 7.20 s and 3.73 s, respectively. The difference observed for the final position is due to the fact that experiments have been carried out in open loop. Velocities in both directions are displayed in Figure 4.25 (b). For the decoupled displacement, mean velocity is 8.25 mm/s for x axis displacement and 8.42 mm/s for y axis displacement. The means velocity for the diagonal displacement is obviously $\sqrt{2}$ times higher than the decoupled velocity and is 11.76 mm/s. In the case of coupled displacements, 16 PEDCs have been supplied while only 8 PEDCs have been necessary in the case of decoupled displacement to perform the displacement from the starting point to the arrival point.

The above analysis shows that the pallet is able to reach a given position using two different strategies. With the first one (coupled), the velocity is high but it requires more PEDCs to be supplied which could lead to increase in temperature. Also, more number of voltage to current convertors are needed which will add up to the cost. With the second one (decoupled), the time needed to attain the position is higher but half number of PEDCs are required to be

supplied and so less number of voltage to current convertors are used. Then the cost will also be low. The strategy to be selected depends then on the context where it will be used.

Chapter 5: Fiber Optic Displacement Sensor

High precision is an important requirement in the SEC platform especially when precise positioning of the silicon pallet is required. In order to improve the precision of the SEC platform, a closed loop control could be implemented locally on the platform. For that, a compact and non-contact sensor can be used in order to not disturb the silicon pallet motion. A solution based on an optical sensor and a microfabricated mirror grating that has been developed at the Roberval laboratory of the Université de Technologie de Compiègne is selected [KHIA 2010b; PREL 2006]. The sensor is a Fiber Optic Displacement Sensor (FODS) which is able to measure long range with high resolution.

A closed loop control can be obtained by integrating a part of the FODS in the SEC platform. This has already been done in the previous works on MPS system for few millimeter strokes. In this chapter, at first, the principle of the FODS is presented. Experiments have been realized using micro fabricated grating and two Fiber Optic Probes (FOPs) to obtain signals. These signals are then used to measure long range displacements. In this work, a signal processing algorithm for online displacement measurement of the mobile part with high resolution has been developed. The principle of the signal processing algorithm to measure the displacement of the mobile part is then explained. Finally, experimental signals are used to test and validate the principle of signal processing algorithm. In the end, performance and robustness of the algorithm is discussed with the results obtained using experimental signals.

5.1 Design and principle of FODS

The FOP probe consists of an emission fiber, placed at the center, surrounded by several reception fibers (Figure 5.1 (a)). In classical configuration, the FOP is placed in front of a flat mirror as shown in Figure 5.1 (b). The emission fiber emits light which is reflected by the mirror and collected by the reception fibers. The light collected by the reception fibers depends on the mirror position (d). The extremities of the reception fibers are placed in front of a photodiode which converts the quantity of collected light into a voltage (V_{out}). In Figure 5.2 (a), the evolution of the output voltage is shown as a function of the mirror displacement where the direction of the displacement is aligned with the probe mechanical axis. The sensitivity curve can be divided into four zones. Zone 1 is the dead zone where the receiving fibers cannot collect light because of the space between the emission and reception fibers (Figure 5.2 (b)). Zones 2 and 4 are strongly nonlinear with variable sensitivities or poor

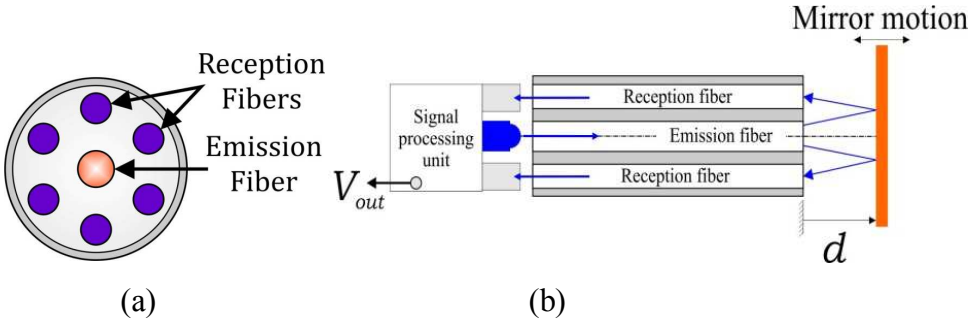

(a) (b)

Figure 5.1 FOP characterstics (a) Emission and reception fibers (b) Working of FOP

resolution. Zone (3) (Linear zone) is the most interesting zone because it has high and constant sensitivity. However, the range of this zone is very small (≅100-200 µm).

The range of the FODS system has to be increased which is required for the precise positioning of the silicon pallet on the SEC platform. For that, the change in the displacement direction of the mirror has been proposed. Instead of moving the mirror aligned with the probe mechanical axis, the motion is now done at an angle of its surface resulting in the increase in range by the $1/Sin\alpha$ ratio (see Figure 5.3) [PREL 2006]

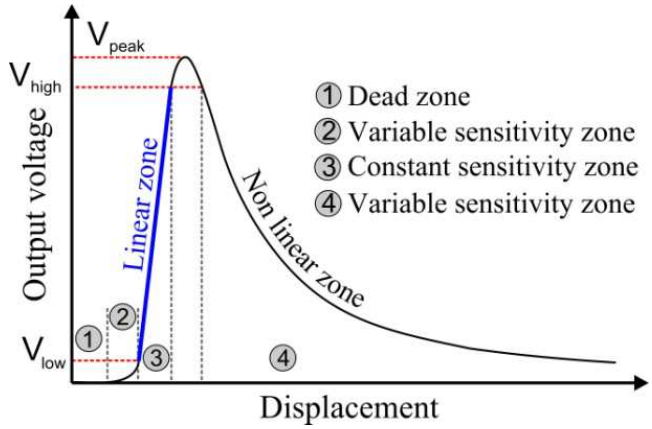

(a)

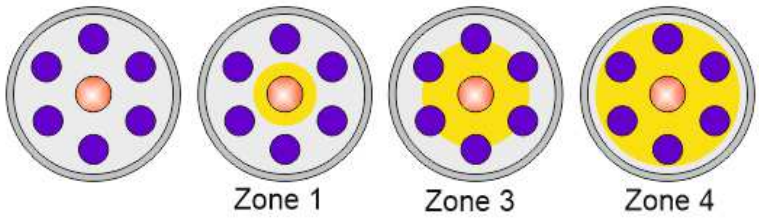

(b)

Figure 5.2 FOP output response (a) sensitivity calibration curve (b) different zones of the sensitivity curve

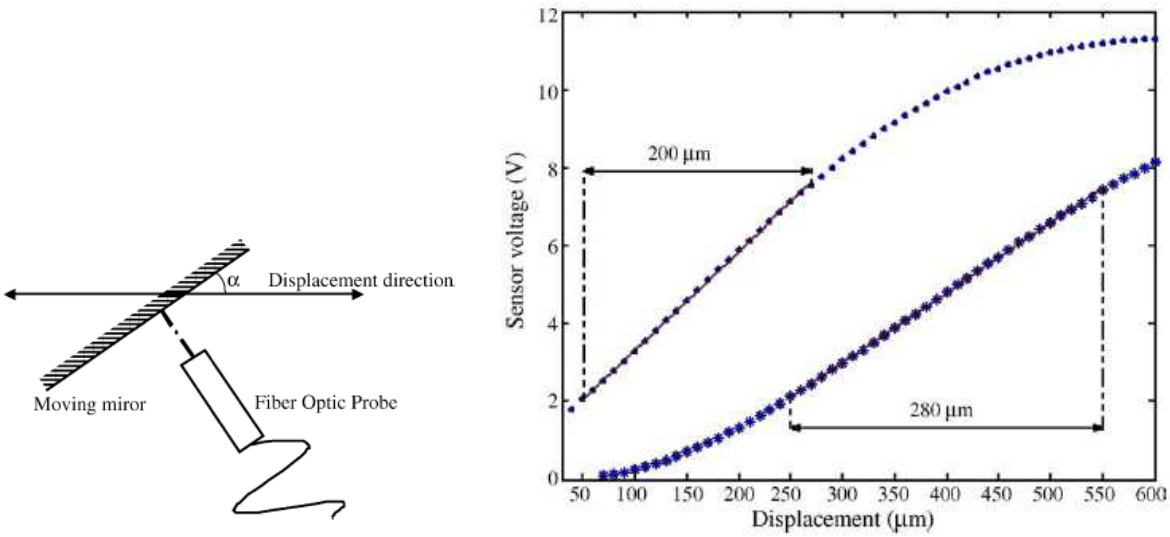

(a) (b)

Figure 5.3 (a) Tilted mirror configuration (b) Increase in sensor measurement range

In the previous works, it has been concluded that for an angle α = 45°, the measurement range can be increased to 40%. By doing this, the sensitivity of the sensor will be deteriorated with the mirror angle (α) and in turn, the limit of resolution will increase. However, increase in limit of resolution remains acceptable (few nanometers) because of the very low limit of resolution of the sensor when it is commonly used when α = 90°. The relation between the new resolution and sensitivity obtained with the mirror angle, α = 45° to the resolution and sensitivity when the sensor is commonly used at α = 90° is given in equation (5.1).

$$R_{(\alpha = 45°)} = \left(R_{(\alpha = 90°)}\right) / \sin\alpha$$
$$S_{(\alpha = 45°)} = \left(S_{(\alpha = 90°)}\right) \sin\alpha \tag{5.1}$$

Even though, the above solution increases the measurement range with low limit of resolution and high sensitivity, it cannot be used to measure displacement of several millimeters in the highest sensitivity zone (Zone 3) of the sensor.

In order to further increase the measurement range, a repeated tilted mirror configuration has

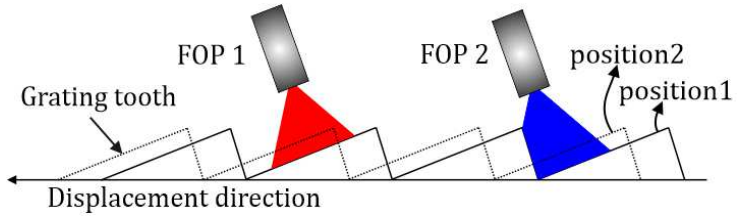

Figure 5.4 Principle of Fiber Optic Displacement Sensor (FODS)

been proposed and developed in previous works [PREL 2006] in order to increase the range of the sensor while keeping a low limit of resolution. In this case, periodical measure is obtained from each grating tooth and so, the range is increased to the length of the grating (see Figure 5.4). Each grating tooth is inclined at an angle α. The measurement range can be increased by increasing the length of the of grating which means more grating teeth can be added to increase the measurement range.

Using this principle, continuity of measure is a problematic as the measure is lost when the sensor probe illuminates two teeth simultaneously. To solve this problem, two FOPs are necessary. When one FOP is at the crossing edge of two teeth, it gives invalid measurement but the other one is placed such that it gives a valid measurement. With two FOPs, either of the two probes always gives a valid measurement. In Figure 5.4, when the grating is at position 1, FOP 1 illuminates one tooth and FOP 2 stays at the cross edge of two teeth. This means FOP 1 gives the valid measurement. Similarly, when the grating is at position 2, FOP 1 is at the cross edge and gives invalid measurement while FOP 2 illuminates one teeth and gives the valid measurement. This ensures a continuous displacement measurement without interruption. When the grating moves in front of the two FOPs, only the linear signals (Zone 3) of the two probes are taken into account and hence, the valid measurement signals coming from each probe are accumulated to compute total displacement measured by the sensor.

In previous works, geometric optimization of the mirror grating which includes, length and height of the grating steps, grating teeth angle etc. has been done in order to achieve smallest possible limit of resolution [PREL 2006]. The angle of the grating tooth has been defined by considering several parameters of FOP design including FOP diameter, numerical aperture, emission fiber diameter etc. The distance between the grating and FOP is an important parameter to consider. Indeed, the two FOPs need to be placed as near as possible to the grating to be in the linear zones of the two FOPs. However, the security distance (d_s) between the probes and the grating is important to fix in order to avoid any collision during motion. Therefore, the total distance between the grating and FOPs includes the security distance (d_s) and the distance that varies with the change in axial displacement between the FOPs and grating (d_a). The criterion to select the security distance with respect to the angle of the grating tooth is given in equation (5.2).

$$d_s > \frac{\phi}{2} \tan \alpha \tag{5.2}$$

Where ϕ represents the diameter of the probe

In the experiments, for the first version of the FOPs, OMRON (E32-D32) probes were used. Each FOP was 2 mm in diameter and had one emission fiber at the centre and four reception fibers surrounding it. In the earlier work on FODS, it has been concluded that with the minimum security distance of 30 µm, the maximum grating tooth angle, α of 3.81° can be achieved [PREL 2006]. In the experiments, the FODS measured 14.9 ± 0.3 nm of resolution over 11.8 mm range with the tilted mirror configuration. The sensor has been further optimized in order to improve the limit of resolution for which grating tooth angle, α had to be increased. However, it leads to limited distance between FOP and the grating for a fixed security distance (ds) of 30 µm.

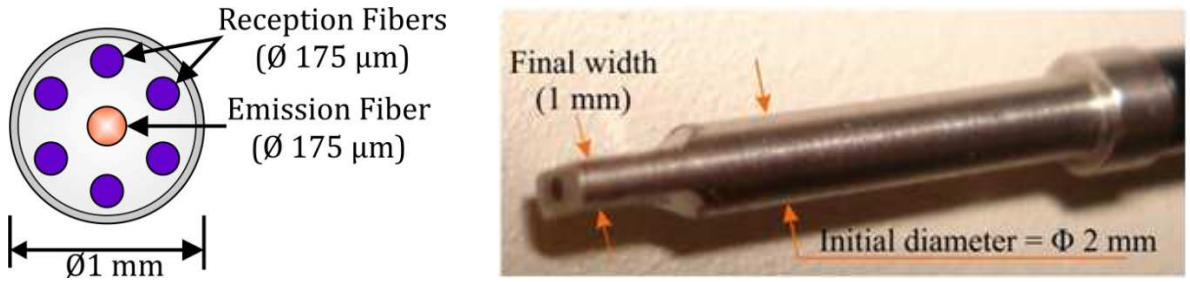

(a) (b)

Figure 5.5 (a) New FOP with six reception fibers (b) Real view of the new FOP

In order to solve this problem, another solution has been proposed where the diameter of the FOP has been reduced to 1 mm [KHIA 2007]. This is done to avoid any collision between the grating and the FOP when α is increased. Due to the difficulty in the machining of the new probe due to very small dimensions, new FOP was purchased from OMRON manufacturers. The FOP consists of one emission fiber at the center surrounded by six reception fibers. The diameter of each fiber is 175 µm (Figure 5.5 (a)) and the numerical aperture is 0.46. The machined new FOP used in the experiments is shown in Figure 5.5 (b). A new dimensionally optimized grating has also been developed in the previous work. It is micro fabricated gold coated silicon grating of 14 mm × 14 mm in dimensions with the grating tooth angle of 8.3°. The two new FOPs are placed in front of the new micro fabricated gold coated silicon grating. In this case, the limit of resolution achieved was 27.4 nm and 38.7 nm in the measured displacements of 8.67 mm and 13.03 mm, respectively.

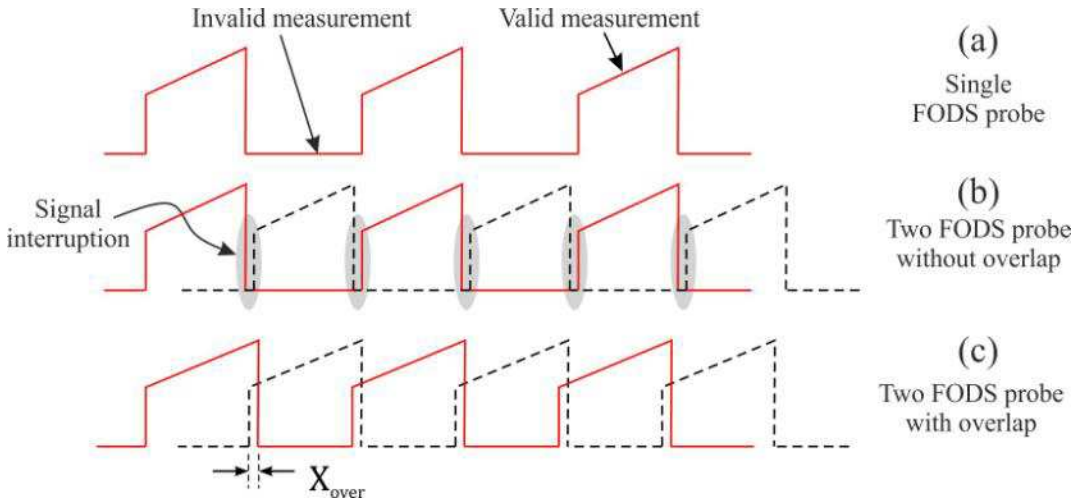

Figure 5.6 FODS signals (a) with single FOP (b) with two FOPs without overlap (c) with two FOPs with overlap

A performance assessment of the new FOP has been done in the previous works [KHAN 2014]. The range of linear zone and sensitivity of the FOP have been computed by moving away a flat mirror in front of the new FOP. The maximum sensitivity of 88 mV/µm was found for the linearized zone of 130 µm with a linearity error less than 1%.

As described earlier, two FOPs are needed to get continuous signal measurement. However, discontinuation in signals could occur with two FOPs configuration if they are not properly placed. In Figure 5.6 (a), signal with single FOP is shown that leads to discontinuation. Then two FOPs are used, signal interruption is visible which hampers the displacement measurement continuation (Figure, 5.6 (b)). It occurs due to the relative distance between the two FOPs with respect to the grating step. To overcome this problem, a signal overlap (X_{over}) is required in order to switch between the two signals to get continuous displacement measurement (Figure 5.6 (c) [PREL 2006]. The equation to select the relative distance between the two FOPs is given in equation 5.3.

$$\delta = (n + \frac{1}{2})l \tag{5.3}$$

Where δ is the distance between the two FOPs, n is an integer and l is the length of a grating tooth. This relation ensures symmetrical overlaps at each crossing edge between two teeth of the grating.

Enough overlap is required to switch between the two signals from the two FOPs. In previous works, the geometrical modeling of the new grating is also done to optimize the grating tooth

angle in order to obtain enough overlap required for switching. It has been concluded that the switching should happen only in the overlaps of the linear zones of each signal.

In order to use the FODS efficiently; a signal processing algorithm is required which is able to switch between the two signals (linear zones) of the two FOPs in order to compute the displacement of the mobile part online.

5.2 Signals obtained in previous works

In this section, the signals that have been experimentally obtained are analyzed in order to design an robust and adaptive algorithm to the shape of the signals coming from the two FODSs.

In the previous works, the experimental signals of FODS have been obtained by doing experiments where two FOPs are placed in front of the new grating of 14 mm in length [KHIA 2010a]. The grating is placed on a translation stage to get the movement in horizontal direction (lateral displacement). For the limit of resolution measurements, a piezoelectric actuator (PI 845-10) was used (Figure 5.7(a)) because it has sub-nanometer resolution in closed-loop. The signals are acquired with the frequency 100 Hz at 0.1 mm/s velocity.

The axial distance between the two probes was chosen to have an overlap between the linear zones throughout the range. The overlap reached experimentally (29 µm) confirms the geometrical model requirement [KHIA 2010b]. The fiber optic sensor measures the linear displacement in the long-range by alternating between the measurements coming from the first FOP and those coming from the second FOP (see Figure 5.7(b)). The average sensitivity reached on 8.67 mm range (in 14 steps of the grating) is 16.06 ± 0.16 mV/µm and the limit of resolution obtained is 27.4 nm.

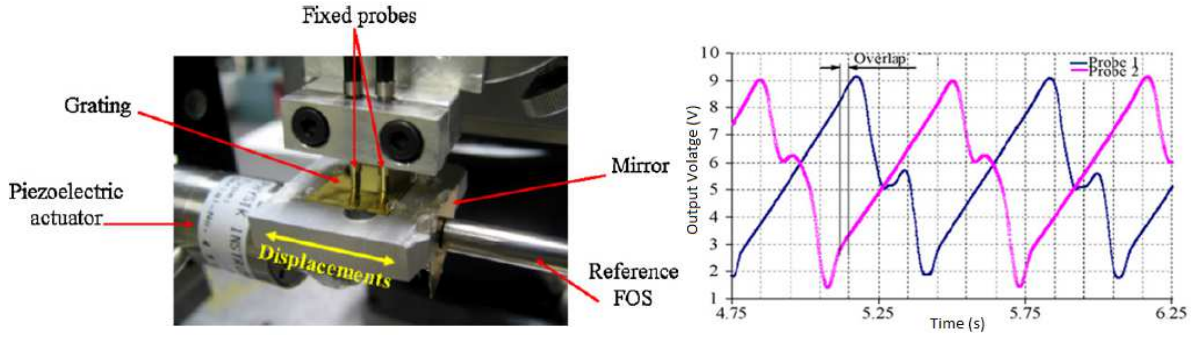

Figure 5.7 (a) Experimental set up in dynamic mode (b) Experimental signals obtained in the previous works[KHIA 2010a]

5.3 Signal processing algorithm

The problematic of the previous study is to measure continuous displacement from the two FOP signals. As mentioned earlier, the valid measurement is the linear parts of the signals which need to be filtered to measure the total displacement to achieve an online displacement measurement. For that, a precise and robust signal processing algorithm is required that allows switching between the two signals. The approach used to obtain continuous switching between the two probes at the optimal positions while keeping high resolution is described. In this work, the proposed algorithm has been developed to ensure the continuous measurement of a long-range displacement by considering various parameters including velocity, frequency and shape of the experimental signals.

5.3.1 Objective of the algorithm

The objective of the algorithm is to analyze the FODS signals and to determine the displacement of the mobile part online. Two signals are obtained from the two probes as presented in Figure 5.8 (a). The algorithm switches between the two FOPs in the overlap region to ensure measurement without interruption.

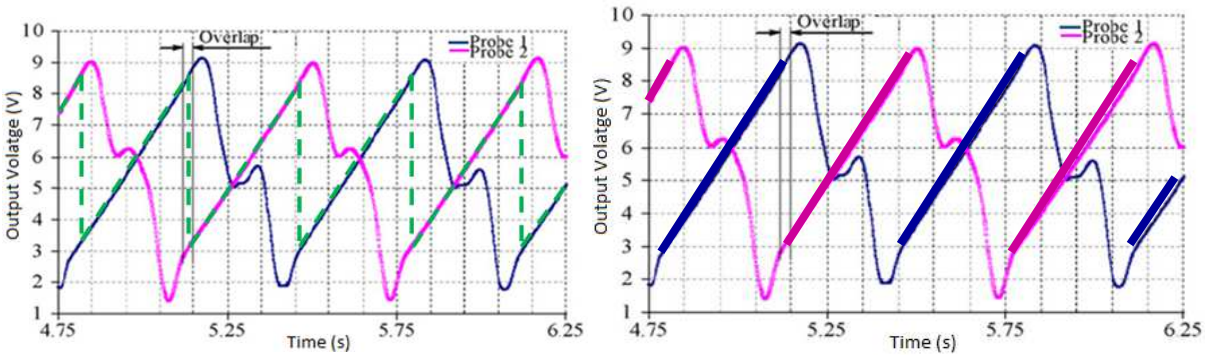

Figure 5.8 FODS signals (a) Linear parts of each FOP signal (b) Switching in overlap regions

The algorithm should ensure switching from the linear part of one signal to the linear part of the other in order to achieve millimetric range and sub-micrometric resolution (Figure 5.8 (b)).Various parameters of FOPs such as sensitivity, data acquisition frequency and measurement velocity are taken into account in order to find the optimal position relative to silicon grating at which the algorithm switches between the two signals. Finally, all the linear parts obtained from the signals are filtered to obtain the valid measurement from the two

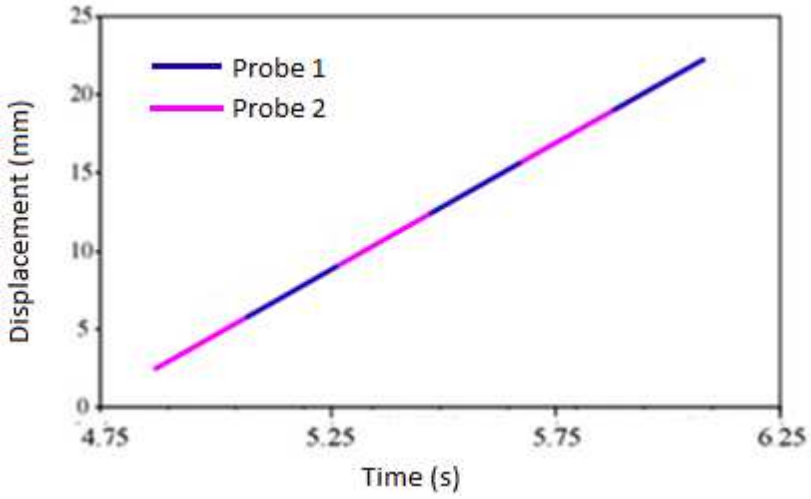

Figure 5.9 Displacement of the mobile part

FOPs. These linear parts are then accumulated to compute the total displacement of the mobile part (Figure 5.9).

5.4 Principle of the algorithm

The algorithm is based on the comparison of two sets of signals to determine the total displacement of the mobile part. The first set regroups the two reference signals. These signals are referred as FOP1_r and FOP2_r for FOP 1 and FOP 2 respectively and are obtained at constant and low velocity (V_{ref}) with high acquisition frequency (f_{ref}). The second set is composed of two measured signals called FOP1 and FOP2 for first FOP and second FOP respectively, with any higher and variable velocity (V) and lower acquisition frequency (f).

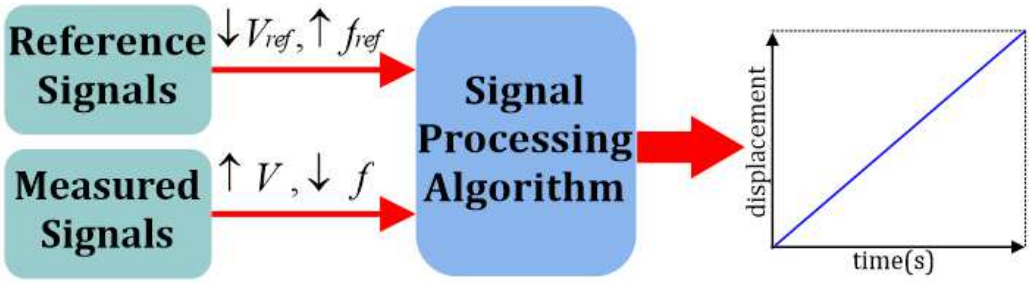

Figure 5.10 Principle of algorithm

The two sets of signals are experimentally obtained by moving the grating horizontally in front of the two FOPs (Figure 5.10).

The maximum velocity (V_{max}) and the minimum velocity (V_{min}) of the measured signals are fixed in advanced and this data represents inputs of the algorithm. The distance between two points in the measured signals is given by V/f (see equation (5.1)) where V is the actual

velocity which lies between V_{min} and V_{max}, and f is the acquisition frequency of the measured signals. Similarly, the distance between two points of the reference signals is V_{ref}/f_{ref}. Equation (5.2) describes the necessary condition to use the algorithm. This equation ensures that the distance between two points of the reference signals (V_{ref}/f_{ref}) is smaller than the minimum distance between the two points in the measured signals (V_{min}/f). The smaller the (V_{ref}/F_{ref}), the better is the resolution of the measurement. However, the calculation time is also important to consider.

$$V_{min}/f \leq V/f \leq V_{max}/f \qquad (5.1)$$

$$(V_{ref}/f_{ref}) \leq (V_{min}/f) \qquad (5.2)$$

5.5 Steps involved in the algorithm

The algorithm is divided into two steps: pre-processing step and processing step. The pre-processing step determines the linear zones of the reference signals and the voltage values for optimal switching in the overlap regions of the two signals. Then, the processing step determines the displacement of the mobile part by comparing the actual measured voltage values [FOP1, FOP2] with the reference signals voltage values [FOP1_r, FOP2_r]. The two steps are described in this section.

5.5.1 Pre-processing: Determining the linear parts of reference signals

The main objective of the preprocessing step is to determine the linear parts for the two reference signals in order to prevent switching between two probes in non linear zone and to obtain uniform displacement measurement. In addition, the presence of noise in the signals disturbs the uniformity of the displacement while moving from one tooth to the other. The noise may indeed lead to multiple switching in the overlap of two linear parts. To limit the noise effect, two parameters are taken into consideration in order to determine the linear parts of the reference signals: voltage thresholds and slope values. Voltage thresholds are defined at the proximities of the maximum and minimum voltage values and are referred as maxima (V_{Sup}) and minima (V_{Inf}), respectively of the reference signals (Figure 5.11). The algorithm switches from one signal to the next one if the voltage is higher or lower than the voltage threshold depending on the direction of movement of the grating. The algorithm checks if the voltage value of the signals FOP1_r or FOP2_r is higher than V_{sup}, that means the grating is

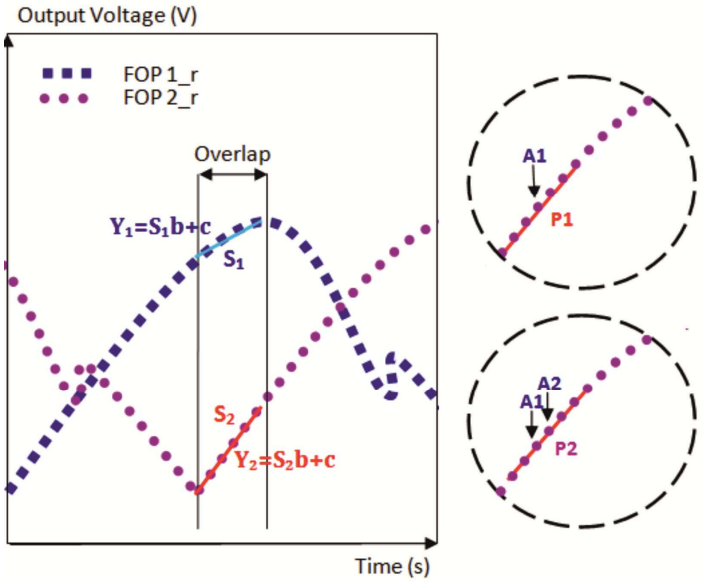

Figure 5.11 Slope comparison

moving in the forward direction, then it switches from one FOP to the other. Similarly, if the voltage value of FOP1_r or FOP2_r is lower than V_{inf} which means the grating is moving in the backward direction, the algorithm switches from one FOP to the other. However, when switching occurs in either of the motion direction, multiple switching can take place due to the noise in the signals. When the grating is moving forward and algorithm checks the voltage threshold V_{sup} to switch from one signal to the other but after switching, if FOP1_r or FOP2_r is less than V_{inf}, the algorithm will again switch to the previous signal. And this can continue until it reaches the right voltage value to switch.

The voltage threshold can be defined separately for the two probes in order to consider possible variations in V_{sup} and V_{inf} of the two signals due to small misalignment of FOPs or fabrication errors in the grating teeth height and length. These thresholds are also defined according to the range of overlap region to ensure that the switching occurs inside the overlap.

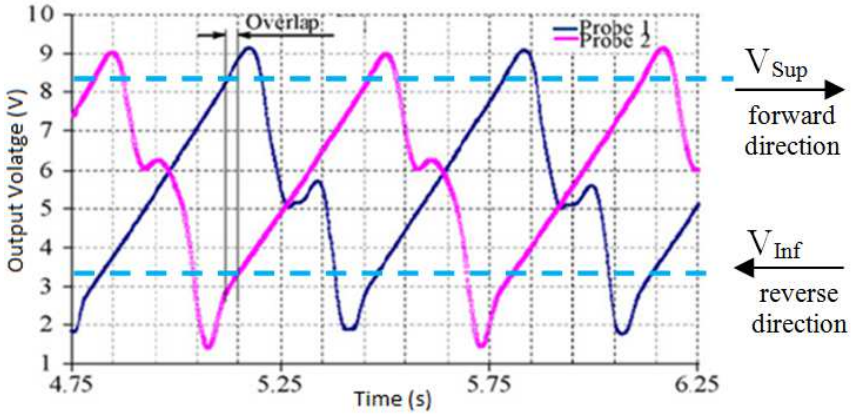

Figure 5.12 Voltage thresholds

The second considered parameter is the slopes of the two reference signals. This is implemented by doing linear fit in order to limit the noise on the signals. In this algorithm, a linear fit of every point in the reference signals is carried out by linearizing the points around it. The slopes obtained for FOP1_r and FOP2_r are then compared to determine the regions where slope values are identical while considering a tolerance. These regions correspond to the overlap regions. The slope tolerance is defined because of variations in slope values which could occur due to small misalignment of FOPs or fabrication errors in the grating teeth height, length etc. This is explained through an example shown in Figure 5.12. If A1 corresponds to the considered point, P1 represents the corresponding linear fit. Similarly, if A2 is the considered point, P2 represents the linear fit and so on. Y1, Y2 are the first degree polynomial equations and S1, S2 corresponds to the slope values for FOP1_r and FOP2_r respectively. The algorithm compares these two values and determines the overlap regions when S1 and S2 are almost identical. There can be a slight difference in the values of the slopes as observed in Figure 5.12. It can occur not only due to mechanical constraints (that include alignment of FOPs, fabrication errors etc.) but also to characteristics of the emission and reception components (i.e. photodiode and LED).

In order to minimize their effects on switching, the algorithm switches from one signal to the other within the slope tolerance defined in the algorithm. Firstly, the voltage thresholds and slope tolerances have been optimized based on the signal values and then the number of points which are considered for the linear fits around the considered point has been chosen. Several configurations by applying linear fits starting from 3 to 15 points have been considered. The tests have been compared in order to improve the results. Finally, seven points have been considered for the linear fits around the considered point.

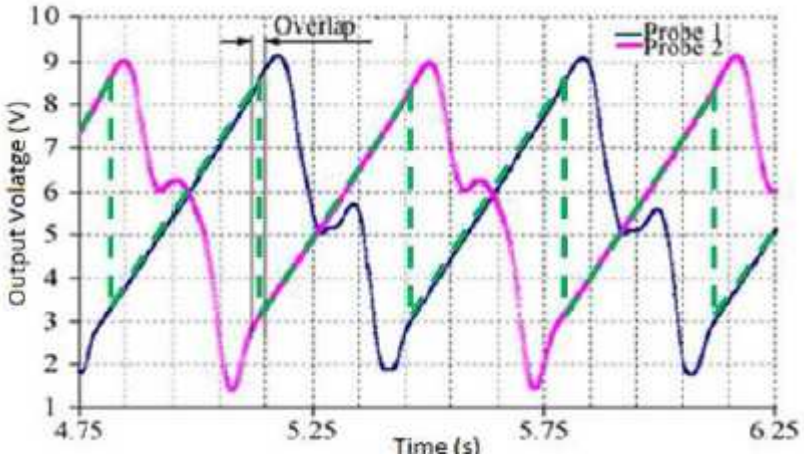

Figure 5.13 Continuous switching between the two signals

Hence, the algorithm switches between the two signals if and only if the signal value in linear zone satisfies the conditions of the voltage threshold and the two slopes of FOP1_r and FOP2_r are within the tolerance simultaneously. A representation of a continuous switching between the two probes can be seen in Figure 5.13.

Flowchart for pre-processing step

The abovementioned parameters and the steps taken in the algorithm to alternate between the two signals of FOPs in the pre-processing of the reference signals are presented in the flowchart given in Figure 5.14. The flowchart presents the steps taken in both motion directions (forward and reverse) of the grating.

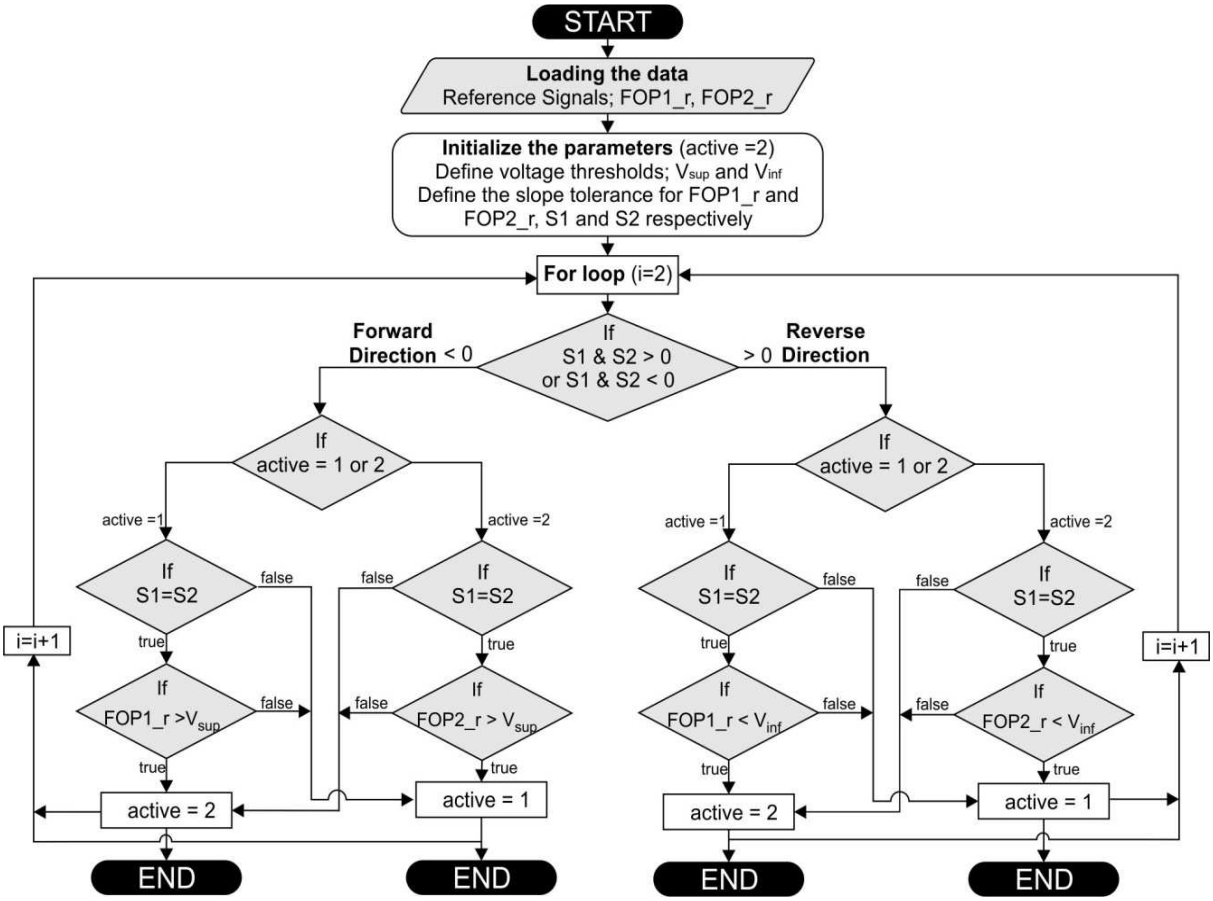

active=1; when FOP1_r is in the linear zone

active=2; when FOP2_r is in the linear zone

V_{sup} : superior voltage threshold at the maxima

V_{inf} : inferior voltage threshold at the minima

S1 : slope tolerance of FOP1_r

S2 : slope tolerance of FOP2-r

i : number of points in the reference signals

Figure 5.14 Flowchart for pre-processing step of the algorithm

5.5.2 **Processing: Determining the displacement**

The second step of the algorithm is the measurement of the mobile part displacement. In this step, the displacement sensor is used and at each step time, the measured voltages [FOP1, FOP2] corresponding to the actual position are acquired. To determine the corresponding position, an interval around the index of the previous point, which corresponds to the previous position in the reference signals, is created. An example is shown in Table I where the index of the previous position in the reference signals [FOP1_r, FOP2_r] is 6 and an interval, called Search Zone (SZ), is fixed around this index. The SZ corresponds to the maximum reachable distance (considering the maximum velocity and acquisition frequency) around every

TABLE I: PROCESS TO DETERMINE DISPLACEMENT

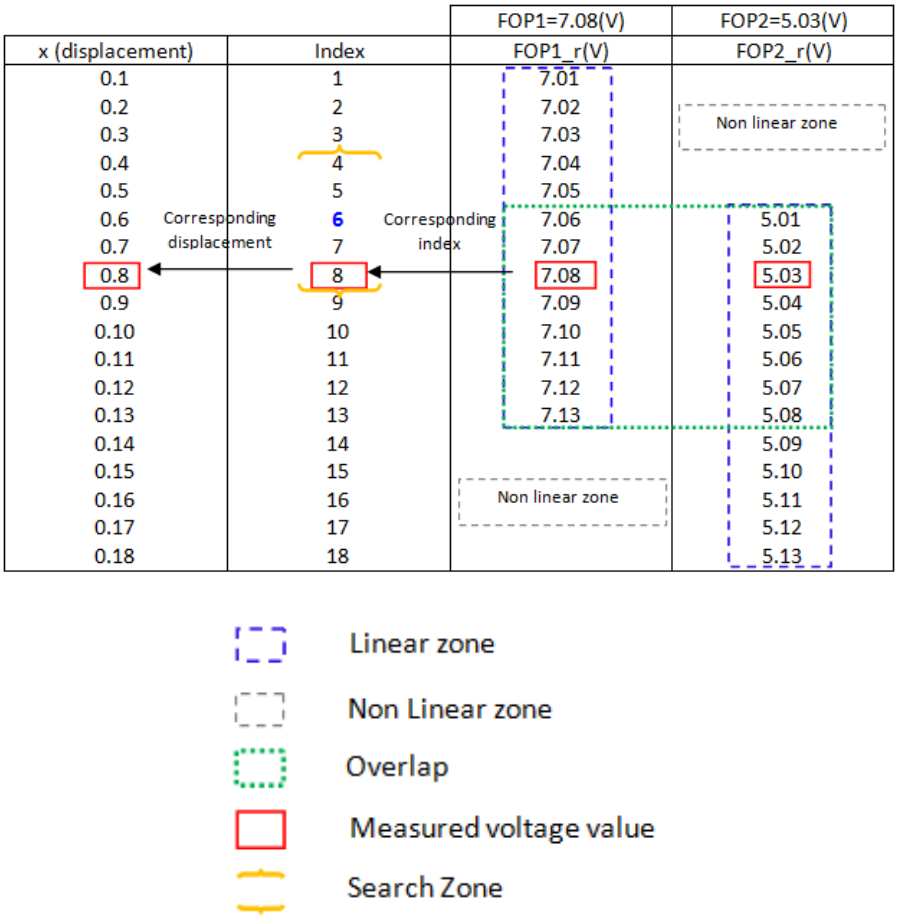

previous point. The maximum number of points around every previous point in the SZ is calculated by (5.3) and is given by N_{ref}. The expression of the SZ is given in (5.4). For the calculation of the SZ, it is considered that the maximum speed (V_{max}) of the measured signal is known in advance. The SZ in the reference signals has been defined around every previous point depending on the frequency (f_{ref}) and speed (V_{ref}) of the reference signals. If the maximum velocity (V_{max}) is chosen to be high and the acquisition frequency of the measured signals (f) is low, the SZ will be large. A large SZ ensures more number of points in the reference signals as compared to the measured signals which results in higher resolution of the measurement system.

$$N_{ref} = (V_{max}/f) * (f_{ref}/V_{ref}) \quad (5.3)$$

$$SZ = [\text{previous position index} - N_{ref},\ \text{previous position index} + N_{ref}] \quad (5.4)$$

In order to determine the displacement, following steps are needed:

1. Definition of the SZ in the reference signals in function of V_{max}, f, V_{ref}, f_{ref}.
2. Search of a voltage couple [FOP1, FOP2] from the measured signals in the reference signals [FOP1_r, FOP2_r]. If the same couple is found in the SZ, the algorithm returns

TABLE II: PROCESS TO DETERMINE DISPLACEMENT

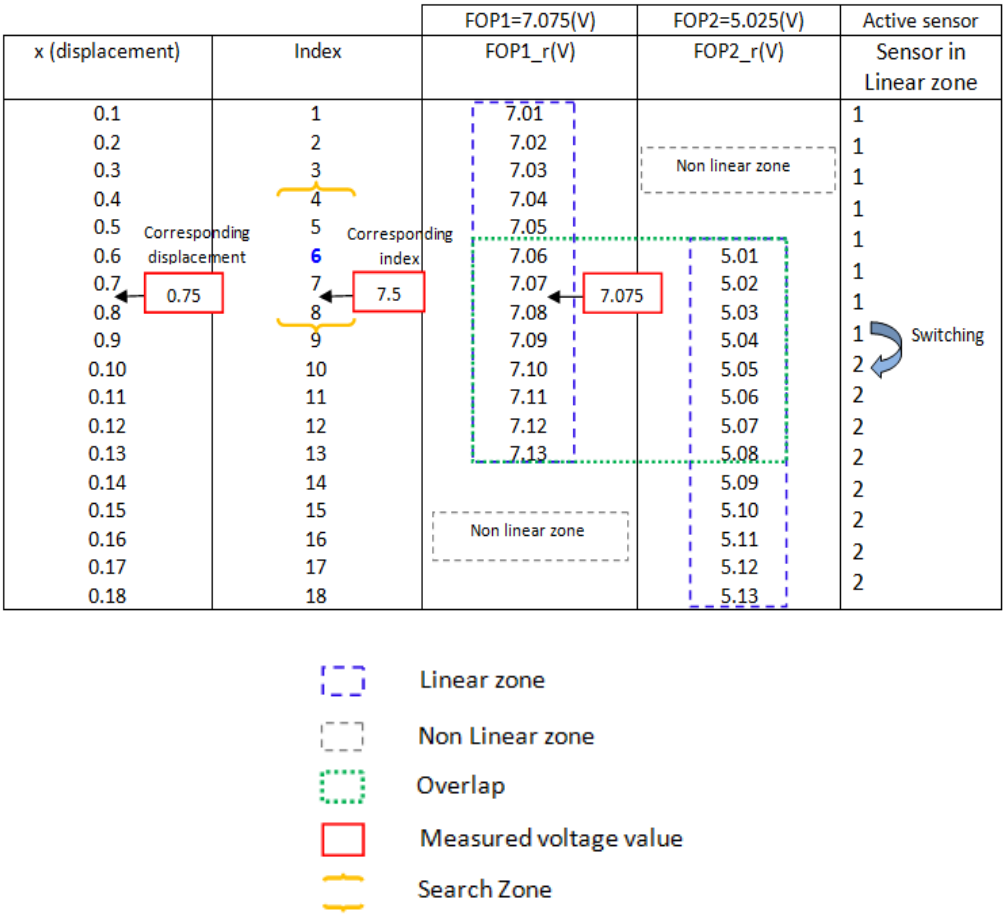

the corresponding index. This is explained with the help of an example illustrated in Table I. The previous position index is 6 around which SZ is created. After defining the SZ, a couple of measured values [7.08 V, 5.03 V] are found in [FOP1_r, FOP2_r]. The algorithm returns the corresponding index which is 8 and corresponding displacement 0.8 mm. If no couple is found in the SZ, linear interpolation is carried out for the sensor in the linear zone (Table II).

An example is shown in Table II where neither of the two values from the measured couple [7.075 V, 5.025 V] exists in the reference values. Since FOP1_r is active in the SZ, the algorithm determines the values immediately before and after the measured value of FOP1 (7.075 V) which are 7.07 V and 7.08 V. Thereafter, 7.075 V is interpolated between the above two values and the corresponding new index is obtained as 7.5 and 0.75 mm is the new displacement value. Similarly, when the FOP2_r is active in the SZ, the FOP2 voltage value will be interpolated in FOP2_r and the corresponding displacement will be determined.

Flowchart for processing step

A brief view of the processing step of the signals is demonstrated in a flowchart presented in Figure 5.15. It presents the steps involved in order to determine the total displacement of the mobile part.

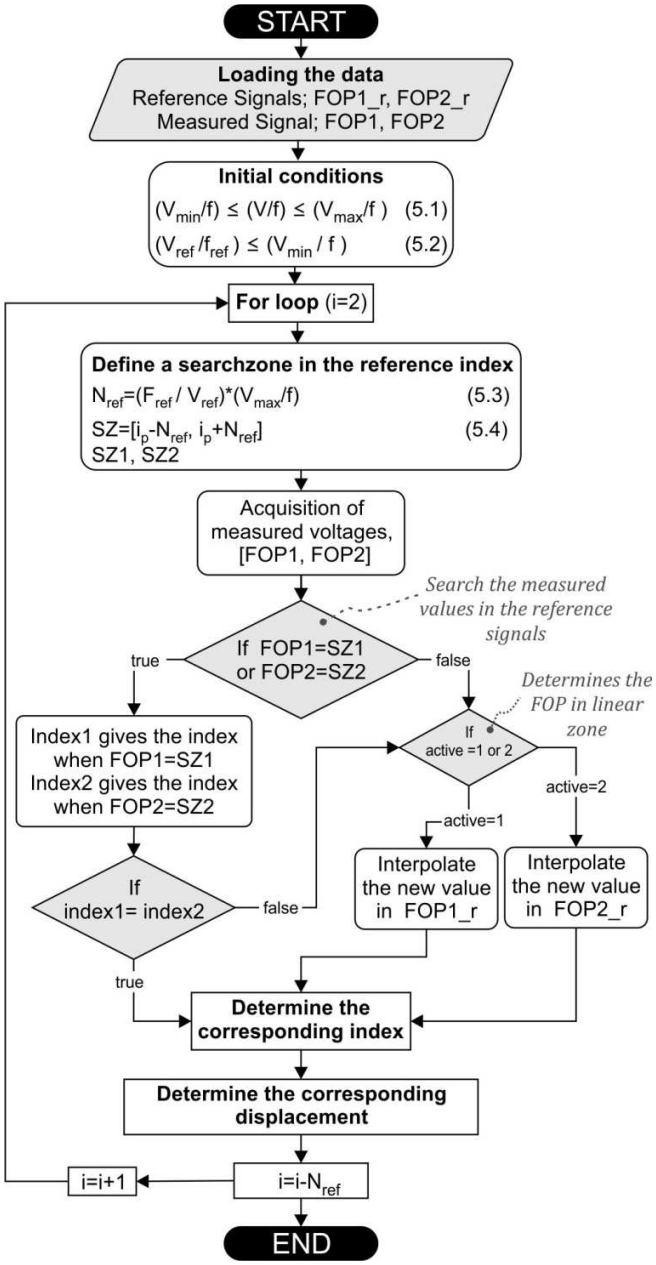

V_{ref} : Velocity of the reference signals

f_{ref} : data acqusition frequency of the reference signals

V_{min} : minimum velocity of the measured signals

V_{max} : maximum velocity of the measured signals

V : actual velocity of the measured signals

f : data acquisition frequency of the measured signals

SZ1 : searchzone of FOP1_r

SZ2 : searchzone of FOP2_r

ip : previous position index

N_{ref} : maximum number of points in the searchzone

N : number of points in the reference signals

Figure 5.15 Flowchart for processing step of the algorithm

5.6 Experimentation

In this section, the aforementioned algorithm has been implemented into MATLAB and tested offline by using real signals obtained from the experiments. Firstly, calibration of the two FODSs has been carried out. The FOPs have been placed perpendicular to the surface grating tooth (Figure 5.16). Then, the linear sensitivities of the two FODSs have been experimentally measured by moving away the FOPs axially with respect to the grating. The sensitivities of both the FOPs are found to be approximately 67 mV/µm.

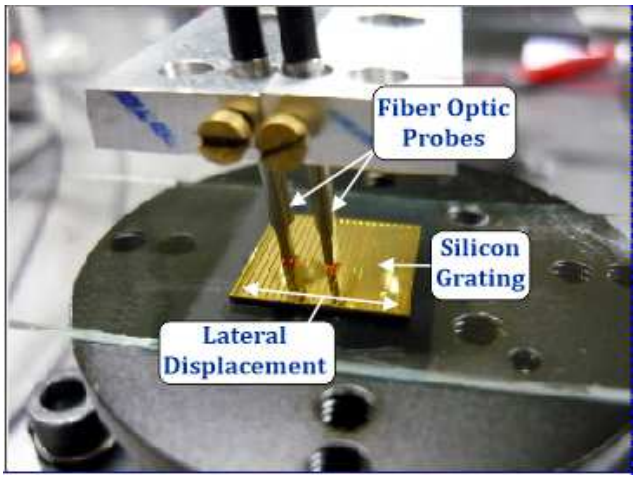

Figure 5.16 Experimental set up

Furthermore, the grating has been horizontally moved with a linear motorized stage in order to obtain signals from the two FOPs. Two experiments have been performed separately; one to obtain reference signals and other is to obtain measured signals. So, the two sets of signals are not identical. For both the experiments, a constant displacement velocity of 0.3 mm/s for the grating and a data acquisition frequency of 300 Hz have been used. In Figure 5.17 (a), presents a set of reference signals; FOP1_r and FOP2_r obtained from the two probes. An

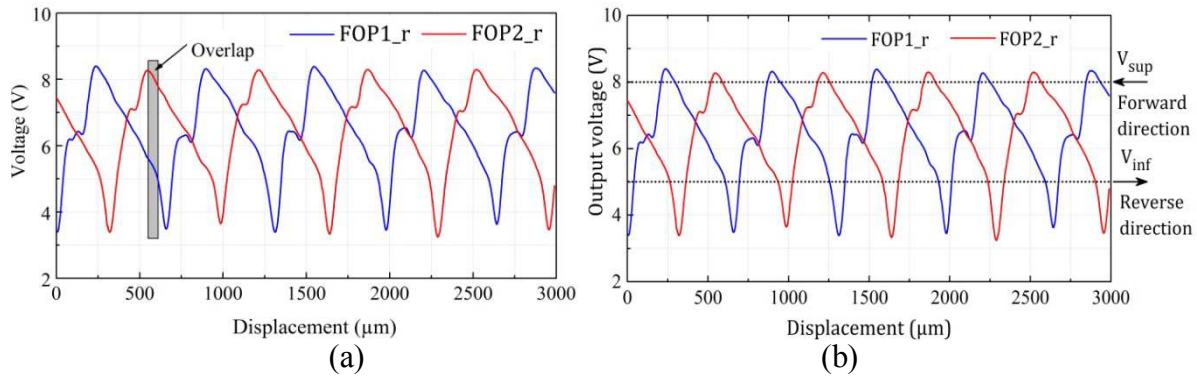

Figure 5.17 Experimental signals obtained from two FOPs (a) overlap in linear zones (b) voltage threshold at the proximity of maxima and minima

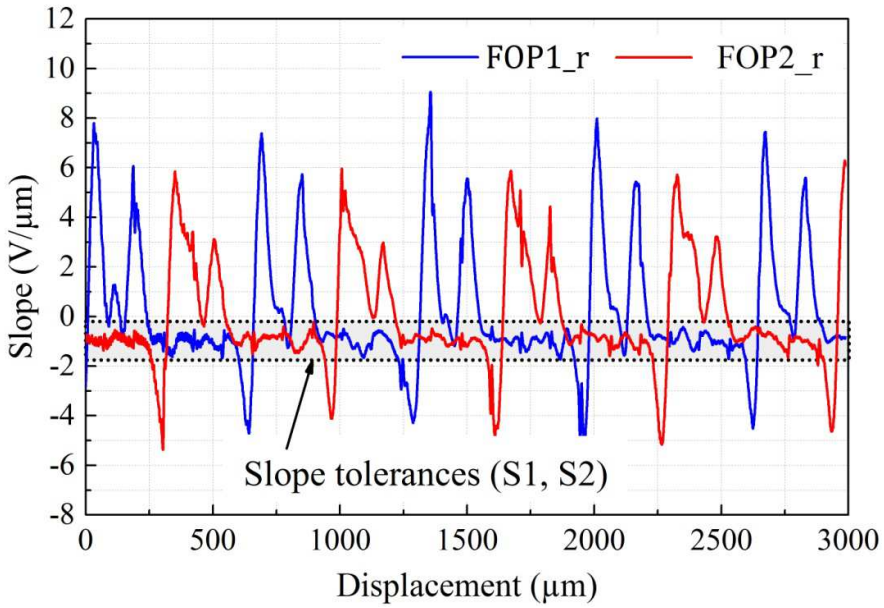

Figure 5.18 Slope tolerance

overlap between the linear parts of the two signals is clearly visible in the signals. As mentioned earlier, the overlap is fixed at the sizing of the grating by taking into account the geometrical and optical parameters of the FOP. The relative positioning between the FOPs and the grating and also, between the two FOPs is crucial to obtain enough overlap. The overlap is generated in order to ensure the measurement continuity.

For the pre-processing of the reference signals where the linear parts of the reference signals are determined, voltage thresholds are defined at the maxima (V_{sup} = 8.2 V) and minima (V_{inf} = 3.8 V) of the reference signals as represented in Figure 5.17 (b). These values have been defined considering the overlap region, because only in this region, the switch between the

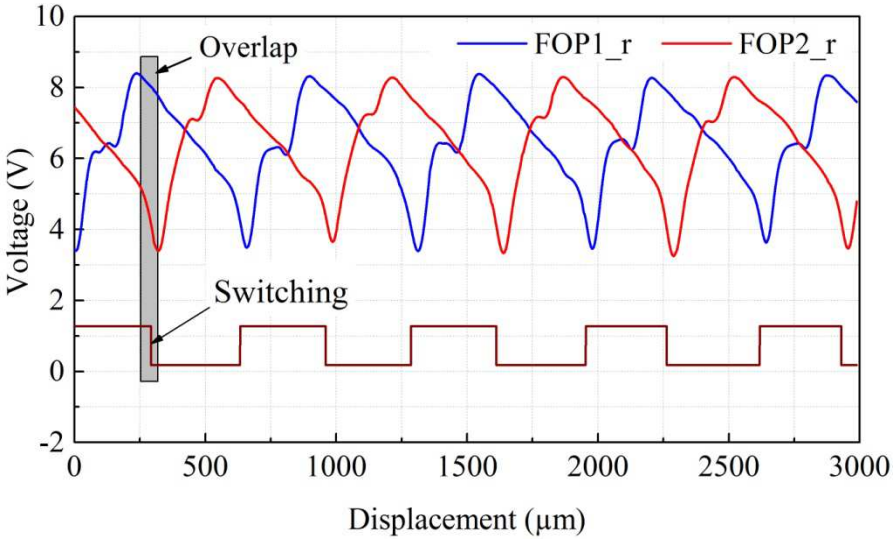

Figure 5.19 Switching between the two signals in the overlap region

signals should occur. During the use of the algorithm, if the grating moves in the forward direction, the switch between the two probes occurs if FOP1_r or FOP2_r is higher than V_{sup}. Inversely, for a motion in the reverse direction, if FOP1_r or FOP2_r is lower than V_{inf}, switching from one probe to the other takes place.

To obtain the slope values, linear fits are applied to each reference point while considering six points before the actual point (seven points in total). The slope values are then determined and compared. In Figure 5.18, the slope value is represented in function of the grating displacement for the two probes. It has been observed that the slope values are similar for both the signals in the overlap region. However, in order to avoid the effect of the slope variation on switching, a slope tolerance has been defined as -0.5 V/µm to -1.5 V/µm for the reverse direction and +0.5 V/µm to +1.5 V/µm for the forward direction. The tolerance is set for both the signals FOP1_R and FOP2_r within which the switching will takes place. The switching between the two probes in their respective linear parts have been defined using the algorithm and are finally presented in Figure 5.19.

After filtering the linear parts of the two signals, the displacement has been computed using the algorithm. The measured signals are compared with the linear reference signals. Depending on the switching between the FOPs, each point of the measured signal is compared to the points of the active FOP reference signals. Interpolation of the measured signals is done in the linear parts of the reference signals (depending on the active FOP). Like this, all the linear parts are accumulated to compute the total displacement travelled by the mobile part.

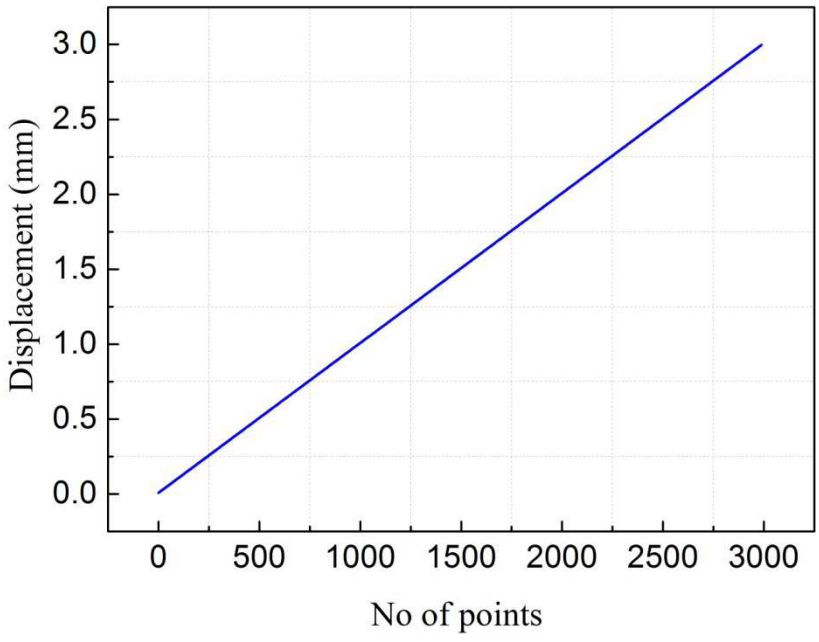

Figure 5.20 Total measured displacement

Figure 5.20 presents the total displacement of 3 mm has been measured using the signal processing algorithm. There is no limitation for the measurement range. It depends on the length of the grating and the calibration should be long enough to measure long displacements. As mentioned earlier, the limit of resolution achieved was 27.4 nm and 38.7 nm in the measured displacements of 8.67 mm and 13.03 mm, respectively.

Therefore, the algorithm presented in this work is able to measure displacement of the mobile part offline while keeping high resolution.

5.7 Conclusion

In this chapter, a signal processing algorithm suitable for determining the displacement of the mobile part of FODS has been presented. This algorithm uses voltage signals from a long range FODS composed of two FOPs to measure the displacement keeping a high resolution and measurement continuity. By specifying voltage thresholds and slope tolerance in the overlap region, the algorithm is able to switch between the two signals obtained from two FOPs in order to obtain measurement without interruption. Finally, the total displacement by using interpolation method is computed.

The feasibility of the algorithm has been proved thanks to an offline test with experimental signals. The proposed signal processing technique has been developed considering the noise on the signals thanks to the voltage thresholds and slope tolerances which make it robust to noise effects.

As perspective, the algorithm will be tested online with different types of experimental signals. The performances of the algorithm will be tested with variable speed experimental signals. Moreover, its robustness will also be tested with signals with different noise levels in order to determine the limits of use and the performance degradation. The developed FODS will be integrated in the SEC platform for precise position measurement of the pallet on the SEC platform. The developed algorithm will then be used to measure the pallet displacement online in order to control it with a closed loop control keeping the high resolution and measurement continuity. As perspectives, the algorithm will be tested online in continuation of this work in future.

Conclusions and perspectives

This section draws, at first, a review of the work carried out during the thesis and then gives an idea on the several possible perspectives as well as possible applications of the device but also on the improvements to be done on the design or performances of the SEC platform in the future research works.

I. Work done during thesis

A state of art on micro and desktop factories has given insight on current trends in the micro and desktop manufacturing. It makes it possible to identify different categories involved in this context that include miniaturized machine tools, production systems, robotics and assembly units and modular micro factory platforms. In a microfactory, the conveyance system is an important requirement which is able to transport micro objects from one place to the other within the microfactory floor. For that, a state of art of conveyance systems has been realized that helped in deducing different actuation technologies that are involved in micro conveyance applications. The realization and the study of this state of art made it possible to imbibe the existing work and the encountered problematic in order to develop an electromagnetic conveyor platform based on the laboratory experience in this field. Its originality in relation to the existing devices lies in the design based on matrix coil architecture where each coil can be controlled independently. With this design, the guidance function is obtained without adding extra elements (using PEDCs orthogonal to the PEDCs supplied for motion).

The matrix design ensures low energy consumption by locally activating few cells of the matrix in the neighborhood of the moving pallet and its ability to manage and control several moving pallets simultaneously. During the designing of the SEC platform, an analytical electromagnetic modeling has been realized to compute the electromagnetic forces exerted on the PMAs and the displacement of the movable pallet in function of the control signals. To validate the concept of SEC platform, an experimental prototype of 5 × 5 matrix square design of dimensions 130 mm × 130 mm has been developed using a four layer PCB. Each cell of the matrix is 25 mm × 25 mm in dimensions. The transition zone has been the crucial parameter in designing the SEC platform. Considering several PEDCs design constraints and PCB manufacturing constraints, six conductors have been removed from the transition zone which makes a transition gap of 3.5 mm between each cell of the matrix. The prototype PCB has been manufactured and experimentally tested.

Numerous experimental tests have been carried out in order to qualify the performance of the conveyor system. The detail performance analysis of the 2D actuator and of the SEC platform is described further.

1. 2D actuator

Firstly, one elementary cell of the platform has been experimentally tested and validated for the planar motions. For that, a 2D actuator has been realized by developing a mover composed of three PMAs. The design of the mover has been adapted to the coil design which is able to perform planar motions. 0The mover displacements have been computed by using an image processing algorithm from images taken by a camera placed above the actuator. A motion stroke of 1.8 mm along x-axis and 1.65 mm along y-axis has been measured. During this experimental test, a 0.6 A current value has been used for both displacement axes. The difference in the measured displacement along both axes is due to difference of generated forces between the two axes. Planar motion along *xy*- axis has also been performed and the displacement measured is 2.47 mm in the forward motion and 2.44 mm in the backward motion

2. SEC platform

Secondly, experimental tests of the whole conveyor surface have been completed and its ability to perform long stroke motions along *x*-, *y*- and *xy*- axes and rotation along z-axis has been validated.

i. Linear displacements

The displacement of the mobile pallet has been successfully computed by developing a new image processing algorithm adapted to the pallet design. Motions along *x*- axis has been performed with a nominal current of 0.4 A (found in simulations) and with a guidance current of 0.4 A along *y*- axis. The same test has then been realized along y-axis. However to generate equal forces along both axes, a nominal current value of 0.74 A has been used with a guidance current of 0.2 A along the *x*- axis. In the experiment, by taking into account that the PMAs are always above the activated PEDC, the nominal displacement strokes are performed along the two axes. Along *x*-axis a nominal motion stroke of 50.48 mm has been measured with a straightness error of 7 µm. Similarly, along *y*- axis, the nominal displacement stroke is measured to be 51.5 mm with a straightness error of 16 µm.

ii. Straightness

A study has been done to characterize the influence of the guidance current on the straightness error. Decrease in straightness error is observed with the increase in guidance currents. For *x*-axis motion, the straightness is indeed decreased from 65 µm to 7 µm for guidance currents between 0 A to 0.2 A. Similarly for *y*- axis motion, a decrease in straightness error is observed from 56 µm to 14 µm with guidance current between 0 A to 0.2 A. Higher guidance current values above 0.2 A till 0.5 A have been tested and the straightness error has remained constant along the two axes. The influence of the motion velocity in function of the guidance currents between 0 A and 0.5 A for different velocities starting from 2 mm/s to 16 mm/s have also been studies. With all the velocities, the straightness is decreasing gradually with increasing guidance currents. It has been observed that straightness error is found to be at almost constant value (7 µm along *x*- axis and 14 µm along *y*- axis) with the guidance current more than 0.3 A at each velocity.

iii. Repeatability

The repeatability errors have been measured for 20 cycles back and forth motion. Two repeatability errors have been measured: the axial (along the displacement axis) and the lateral (orthogonal to the displacement axis). For the mean displacement of 50.5 mm along *x*- axis, the axial and lateral position repeatability error is found to be 5.7 µm and 4.2 µm, respectively. For *y*- axis motion, for the mean displacement of 51.5 mm, the measured axial position repeatability is 9 µm and measured lateral position 4.7 µm.. Therefore, in both the axes, SEC platform exhibits low repeatability error in open loop which can be further reduced by introducing closed loop control.

iv. xy- motion

Planar motions along *xy*- axis have been successfully achieved in open loop. The measured displacement is 31.5 mm along *x*- axis and 31 mm along *y*- axis. Taking into account the drift effect during motion, the amount of hysteresis in *xy* plane is found to be 300 µm. This error can be minimized by reducing assembly errors or using a closed loop control.

In this configuration, the calculated repeatability error is 10 µm along *xy*- axis motion. It is concluded that SEC plat exhibits low repeatability along *xy*- axis in open loop. This can be further reduced by adapting feedback control in real time.

v. Rotation

Rotation tests have also been carried out to measure the maximum rotation angle that can be achieved with the SEC platform prototype. The maximum rotation angle measured experimentally is found to be ±12.37°. The rotation angle is limited due to the geometrical limitation of the PEDCs. In order to achieve higher rotation angle or full circle rotation of 360°, redesigning and remodeling of the PEDCs would be required in future.

It is clear from the abovementioned results that the SEC platform is able to perform long displacements without interruptions. The pallet is easily crossing the transition zone of 3.5 mm and there is no huge influence of removing 6 conductors under the PMA has been observed in the above results obtained in open loop control. Experimental tests have shown the possibility of wide area of planar displacements.

In the last chapter, a signal processing algorithm suitable for determining the displacement of the mobile part of FODS has been presented. This algorithm uses voltage signals from a long range FODS composed of two FOPs to measure the displacement keeping a high resolution and measurement continuity. By specifying voltage thresholds and slope tolerance in the overlap region, the algorithm is able to switch between the two signals obtained from two FOPs in order to obtain measurement without interruption. Finally, the total displacement by using interpolation method is computed.

The feasibility of the algorithm has been proved thanks to an offline test with experimental signals. The proposed signal processing technique has been developed considering the noise on the signals thanks to the voltage thresholds and slope tolerances which make it robust to noise effects.

II. Perspectives

Several perspectives of the presented work are described in this section. They concern the prototypes already studied but also new developments or improvements to the design or assembly of the SEC platform. Also, there is a room for improvement in performances such as high precision, better motion etc. of the SEC platform.

1. Design improvements in the existing prototype

The design of the SEC platform described in this work can be further improved. Firstly, the distance between Layer 1 and Layer 2 is crucial to achieve motion. Customized PCBs can be fabricated where the distance between Layer 1 and Layer 2 can be further reduced in order to

achieve higher electromagnetic forces. And also by using even thinner glass layer for insulation than the one used in this work which is 130 µm in thickness so that the distance between the PMAs and the PEDCs can be reduced. Hence, higher electromagnetic forces could be generated.

The next design parameter to where the improvement is possible is the transition zone. The transition zone between the two cells of the matrix design of the SEC platform can be further reduced by improving the coil design. It will lead to higher generation of forces and hence, much smoother motion can be achieved when travelling from one cell to the other.

It has been experimentally observed that the rotation stroke of the moving pallet is limited on the SEC platform. Full rotation of the pallet has been tried in this work but was not successfully obtained. Further study is required in order to design a PEDC able to generate a full rotation of the pallet. For example, third layer of PCB can be used to design PEDCs that will ensure circular motion of silicon pallet. The first two layers would remain for translation along *x*- and *y*- axis and the circular coils in third layer would help in generating force when the pallet comes at an angle and could not be moved by the first two layers.

An example is shown in Figure C.1 with the representation of PEDCs in Layer to perform circular motion. The normal rotation principle is followed in Step 1 using Layer 1 and Layer 2. When the maximum possible angle is reached, the PEDCs in Layer 3 are activated that helps to further rotate the pallet which is the Step 2. And then once the pallet reaches at certain angle from where further rotation can be achieved by the first two layers, the pallet

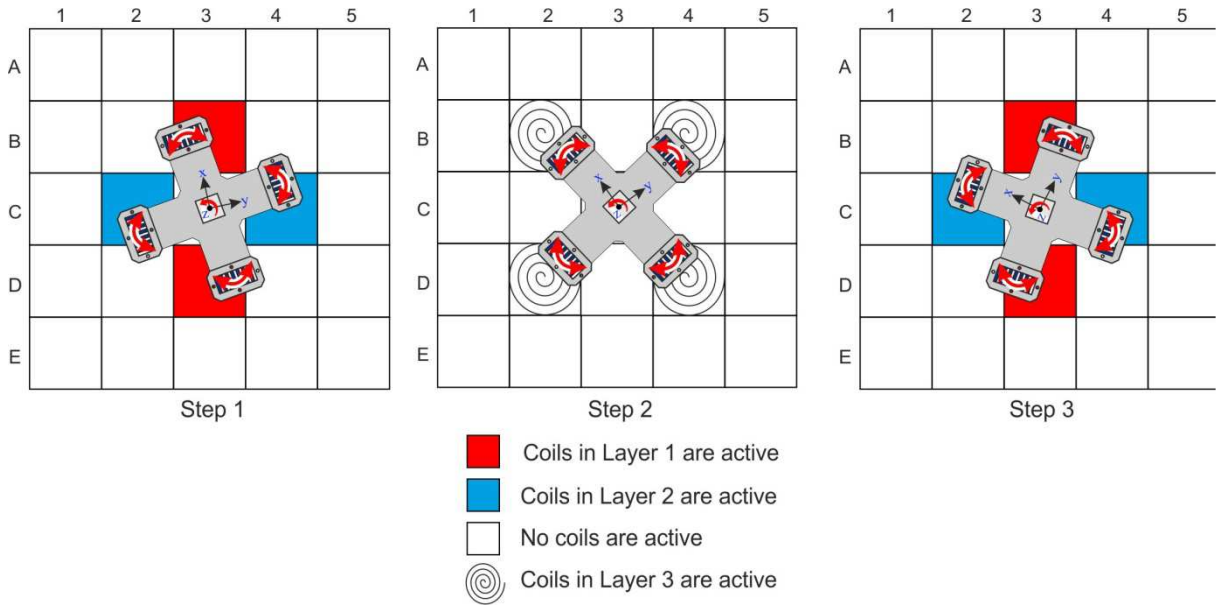

Figure C. 1 Working principle of SEC platform with PEDCs in Layer 3

rotates further (Step 3). By doing this, a 360° rotation of the pallet can be possibly achieved.

In future works, the surface area of the conveyor platform will be increased in order to achieve even longer motions so that several pallets can be accommodated in the SEC platform. One way is to add more cells to the matrix design. Another possible way is a modular based design which can be achieved by assembling small matrix modules. This assembly of elementary modules can potentially make it possible to do several types of displacements by using only few modules for a particular direction and motion range required for the displacement.

2. Performances improvements

In this work, the performance behavior of the SEC platform has been tested in open loop control. In order to obtain precise positioning of the SEC platform, the fiber optic displacement sensor presented in Chapter 5 could be integrated into the SEC platform in order to develop a closed loop control based on the proposed algorithm.

In future, a method could be developed to reduce the power consumption of the SEC platform. This will be done by creating a control algorithm, and a dedicated control circuit, where each cell of the matrix would be controlled and managed independently only when necessary. So, thanks to the control circuit, the algorithm will switch ‘on’ and ‘off’ the cells, depending on the position of the pallet, and the time at which the pallet is in the transition zone. During motion of the pallet, when the pallet crosses over one cell to the next, the previous cell would go ‘off’ and the next cell would go ‘on’ automatically. An example is presented in Figure C.2 when cells B2 and D2 are ‘on’, the pallet moves forward and reaches the transition zone. At this time, the cells B3 and D3 would go ‘on’. Once the pallet reaches the cells B3 and D3, the previous cells B2 and D2 which are not in use now would go ‘off’. By doing this, the energy consumption and then the joule heating will be reduced.

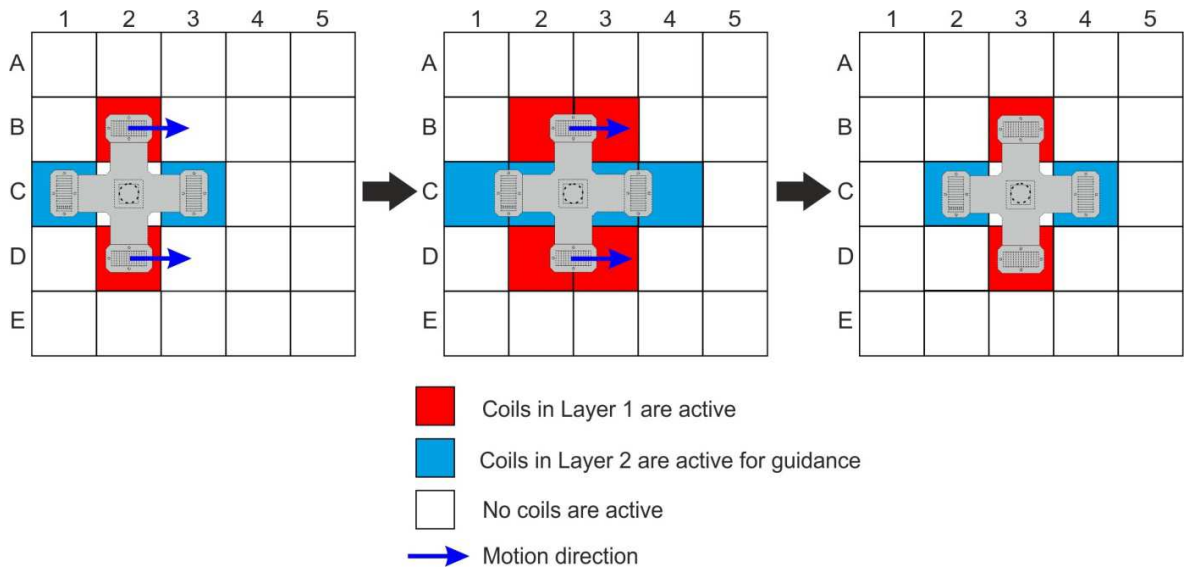

Figure C.2 Switching 'on' and 'off' of the matrix cells

As mentioned before, enlargement of coils would be done to increase the motion range. It gives a possibility to control and manage several moving pallets at the same time.

Furthermore, a dedicated control system should also being developed to minimize energy consumption, manages potential failures of elementary cells and avoids collision between the moving pallets [AROR 2014]. The control system will be used to simulate the global platform behavior and manage the communication with it. Then, the control and monitoring system will be integrated experimentally to validate the control model of the platform. This control module would consider several pallets and take into account of the trajectory of each one. It will also consider the priority and potential damaged cells in order to control each elementary cell of the surface to ensure the conveyance tasks of each pallet and to optimize them.

A framework to model and simulate the SEC control is being developed [DANG 2016]. In this model, the choice of the desired trajectory depends on the objective: fast displacement or minimal energy consumption. The ability to generate refined path trajectories and to avoid collision is respectively has been demonstrated by using path-planning algorithms and interpolation methods and by simulation using simple rule for priority definition. More complexity in managing pallets and on improving the strategy of trajectories determination will be focused in future when the area of the SEC platform will be enlarged. On the technological point of view, a larger SEC platform will be designed and manufactured to be able to test multi-pallet strategies.

Annex A

List of publications

- The Anh Tuan Dang , Magali Bosch-Mauchand, **Neha Arora**, Christine Prelle, Joanna Daaboul "Electromagnetic modular Smart Surface architecture and control in a microfactory context, "Computers in Industry, 2016.

Abstract- This paper presents an electromagnetic conveyance system called electromagnetic modular Smart Surface (emSS) permitting to move pallets on a planar surface in a microfactory context. The proposed surface concept allows flexibility in reconfiguring the system layout along with product routing. The possibilities of accurate positioning of the moving pallet and controlling multiple pallets on the surface make the emSS suitable for reconfigurable and flexible manufacturing systems. However, the emSS control needs to be robust and scalable to adapt the changes in manufacturing systems. A framework is therefore defined to monitor and control the emSS by simulation or in-line. It allows to define product routing on the emSS by satisfying numerous requirements such as reduction in energy consumption, collision avoidance, etc., and to minimize the human interventions by changing product routing when emSS component failures occur. A first experiment realized on an emSS prototype, allowed to compare two paths strategies regarding cost function linked to energy consumption and velocities. Two other studies exploit the emSS modeling in terms of pallet path generation and simulation of collision avoidance.

- **N. Arora**, M.U. Khan, C. Prelle "A planar electromagnetic actuator based on two layer coil assembly for micro applications," AIM 2014, June 8-14, Besançon, France, pp. 174-179.

Abstract- In this paper, the concept of a two layer coil based electromagnetic actuator for planar motions is presented. The actuator is composed of two pairs of fixed overlapped 2D electric drive coils and a mobile part consists of permanent magnets arrays which perform motions in xy plane due to the generation of Lorentz force. A multi-layer printed circuit board is used for the two layers of drive coils. An electromagnetic model of the actuator has been developed in order to compute the electromagnetic force exerted on the magnets arrays. A prototype of the device has been manufactured and tested. The mobile part displacement

along the two displacement axes have been shown and determined using image processing method.

- **N. Arora**, T. A. T. Dang, L. Petit, M. Bosch-Mauchand, J. Daaboul, C. Prelle "Contribution to microfactory technologies: a flexible conveyor and its dedicated control system," IWMF 2014, October 5-8, 2014, Honalulu, HI.

Abstract- In this paper, a flexible conveyor system for microfactory applications is presented. The proposed conveyor allows the automated transportation of micro objects to the desired location within a microfactory. The conveyor system is based on electromagnetic actuation principle. It consists of a fixed coils platform and a moving pallet which regroups several permanent magnets. The fixed conveyor platform is composed of mesh of 2D coils based on matrix arrangement where each cell of the matrix can be independently controlled to form a flexible conveying path for the moving pallet. The matrix design ensures low energy consumption, flexibility, reconfigurability and robustness of the system. Furthermore, a dedicated control system is being developed. It ensures minimum energy consumption, manages potential failures of elementary cells and avoids collision between the moving pallets. The control system is used to simulate the global platform behavior and manage the communication with it.

- **N. Arora**, L. Petit, M.U. Khan, F. Lamarque, C. Prelle "Signal Processing of a high resolution and long-range displacement sensor, " IEEE Sensors 2012, October 28-31, Taipei, Taiwan, pp. 491-494.

Abstract- This paper describes an algorithm which analyses the signals provided by a miniature fiber optic displacement sensor and determines the displacement of the mobile part in line. The measurement system is based on two Fiber Optic Probes (FOPs) placed in front of a micro fabricated gold coated silicon grating. Two signals are obtained from the probes and the algorithm ensures a switching between the two signals in order to achieve millimetric range with nanometric resolution without interruption. The algorithm takes into account various parameters of the FOPs such as sensitivity, data acquisition frequency and measurement velocity in order to find the optimal position relative to silicon grating at which the algorithm switches the two probes. The algorithm provides a robust approach in order to work even with the presence of noise in the FOPs signals.

- **N. Arora**, L. Petit, M.U. Khan, F. Lamarque, C. Prelle "Algorithm for signal processing of long-range displacement sensor," REM-MECHATRONICS 2012, November 21-23, Paris, France, pp. 397-402.

Abstract- An algorithm for signal processing of long-range fiber optic displacement sensor is described in this paper. The algorithm analyses two signals provided by a measurement system which contains two Fiber Optic Probes (FOPs) placed in front of micro fabricated gold coated silicon grating and determines the displacement of the mobile part online. The algorithm provides a scheme of switching between the two signals from the two probes in their respective high sensitivity zone, without interrupting the displacement measurement. An approach is adapted in order to achieve millimetric range with nanometric resolution which also prevents the noise effects on the measurement making the algorithm reliable.

Annex B

Constraints in image processing

Fringe effect

While doing simulations to calculate the displacement of the pallet with the developed MATLAB algorithm, change in area of the desired object (the black square) in each image has been observed which hampers the precise displacement measurement. The change in area occurs because of the presence blurredness due to the formation of fringes. The fringes in the images are clearly seen in Figure B.1. The fringe effect could occur due to high sensitivity of the camera to the light in the room. It changes resolution of the images during motion and hence, change in area of the object occurs. Due to the above mentioned issues, it is difficult to identify the desired object. In order to treat this problem, an area interval of the desired object has been specified in the algorithm in order identify the desired object.

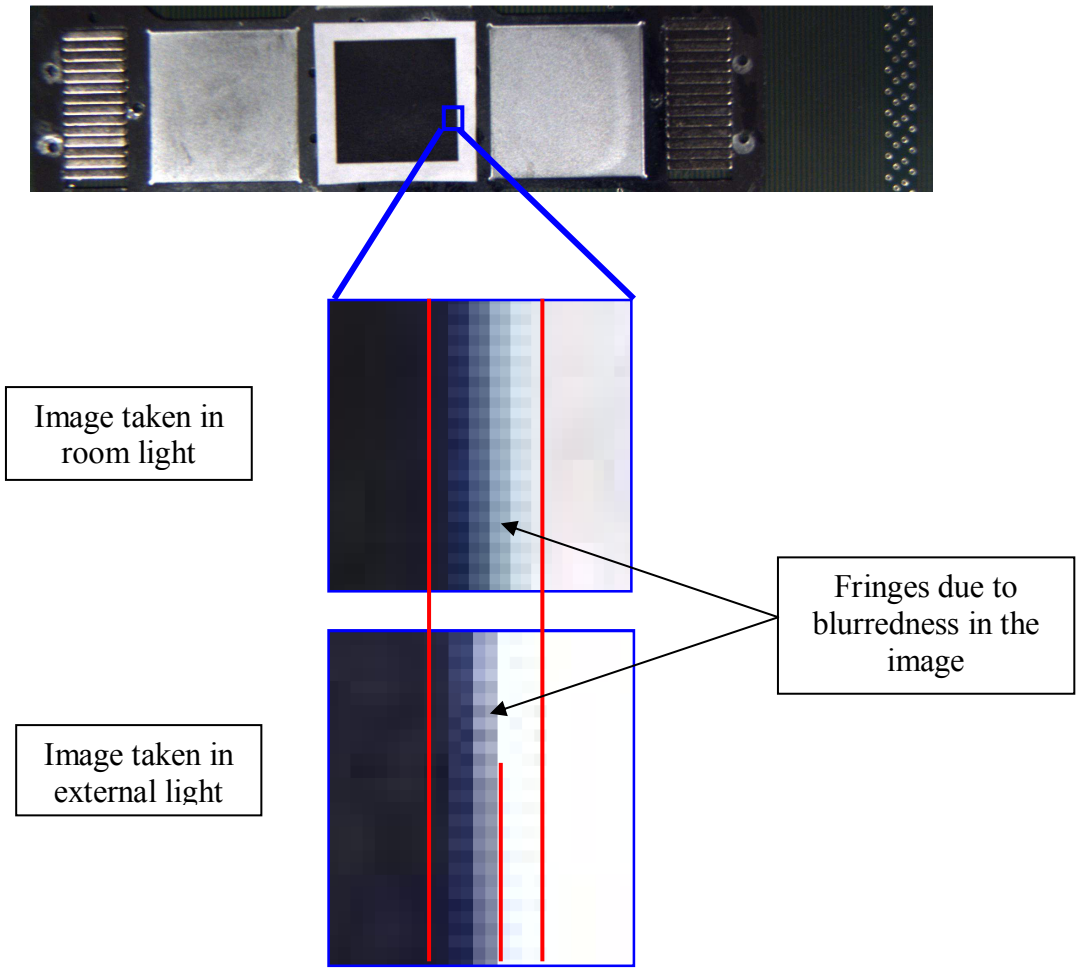

Figure B. 1 Fringe effect in the images captured by the camera

After few tests with different images taken in different light conditions, it has been observed that if external light is used, the blurredness in the image can be slightly reduced which can lead to more precise measurement as compared to the images taken in room light. Therefore, all the images were then taken using external light in this work.

Changes in image resolution

In order to study the effect of the external light and camera lens on the images, concentric rectangles have been drawn on a piece of paper with equal distance between each of them (Figure B.2). The drawing is kept under the camera (PointGrey Grasshopper 3) and an image of size 1024 × 768 pixels has been taken. The image resolution is computed by dividing the real length of the smallest rectangle in middle to the difference in pixels along *x*- axis. Two sides of the rectangle are have been measured; $x2_1$-$x1_1$ and $x3_1$-$x4_1$ to find the resolution along *x*- axis. Similarly, the resolution along *y*- axis is computed by dividing real vertical length of the rectangle with the difference in pixels along *y*-axis. Two vertical sides of the rectangle are measured ($y2_1$-$y3_1$) and ($y4_1$-$y1_1$) and hence, resolution is computed. In both the axes, the image resolution is found to be 42 µm. From the image, the four coordinates of all the rectangles have been measured in pixels manually, starting from coordinates of the smallest rectangle in the middle [$x1_1$, $y1_1$], [$x2_1$, $y2_1$], [$x3_1$, $y3_1$] and [$x4_1$, $y4_1$] to the coordinates of the largest rectangle going bigger towards exterior; [$x1_n$, $y1_n$], [$x2_n$, $y2_n$], [$x3_n$, $y3_n$] and [$x4_n$, $y4_n$].

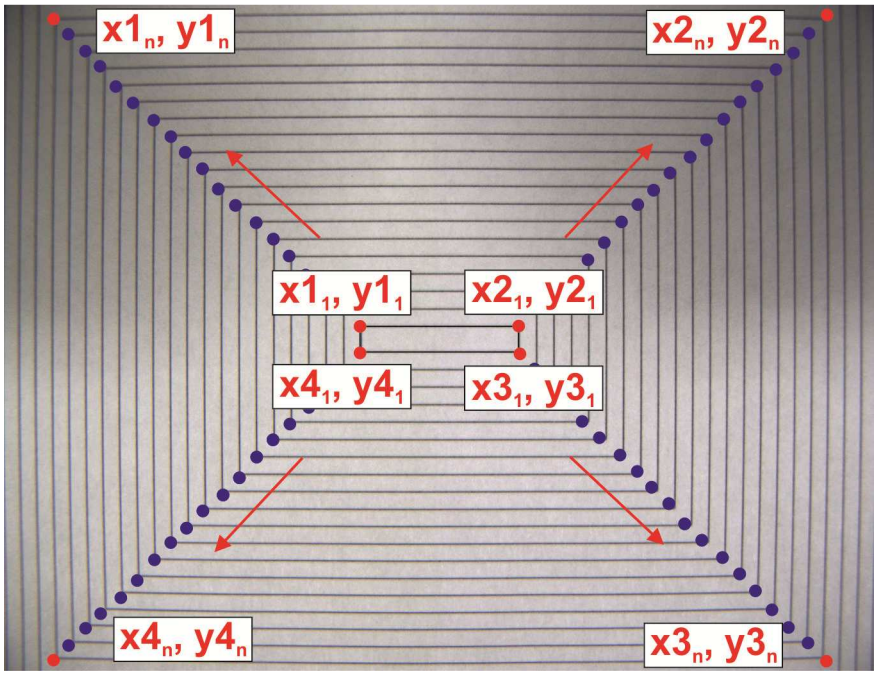

Figure B. 2 Concentric rectangles image to analyse the change in resolution of the image

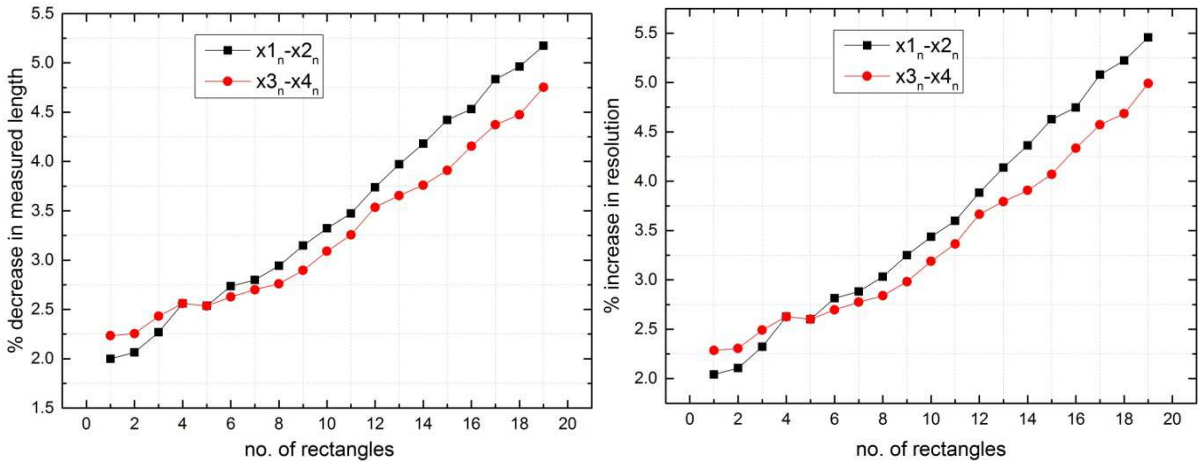

(a) **(b)**

Figure B. 3 Effect of camera lens (a) % decrease in measured length of rectangles (b) % increase in image resolution

Using these coordinates, the lengths of four sides of all the rectangles have been measured and compared with the theoretical lengths of each rectangle.

The analysis shows that the measured lengths are smaller than the real length of the rectangles. The larger the rectangle is, the higher the % decrease in the measured length is (Figure B.3 (a)). It means that the more it moves towards the extreme corner of the image, the more is the error in measurement is. Starting with 2% decrease in measured lengths for the smallest rectangle in the middle, it goes approximately to 5% for the largest rectangle in both x and y axis. This is due to concave effect that appears on the image due to the camera lens.

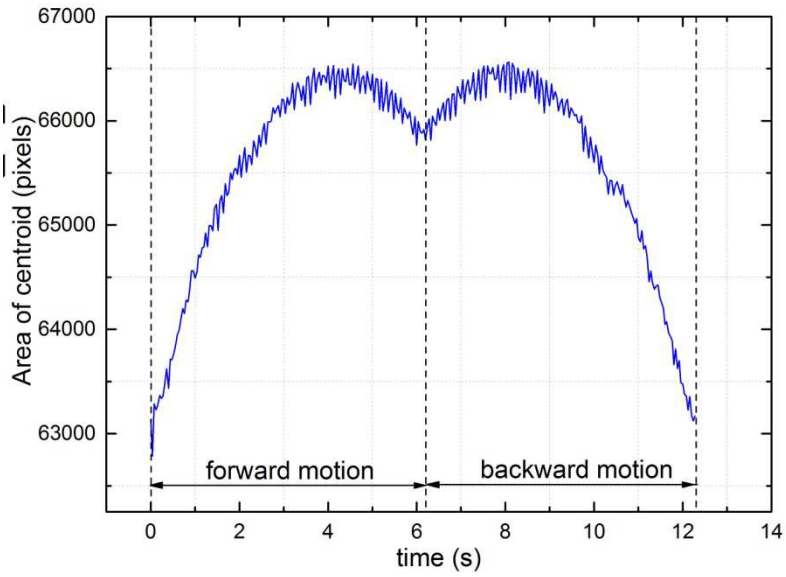

Figure B. 4 Change in computed area of the black square during forward and backward motion along *x*-axis

This distorts the resolution of the image slightly and makes it higher at the corner of the image. Figure B.3 (b) shows % increase in the resolution of the image while moving from the smallest rectangle to the largest. The resolution error increases from 2% to 5-5.5% from middle to the extreme corners along x and y axis. The actual image resolution is 42 µm which increases to almost 45 µm at the corners of the image in both the axis which makes it 7% higher than the middle of the image. Though the error is not so high, it makes it difficult to optimize the upper and lower limits of area interval of the black square in the image processing algorithm. Therefore, it hampers precise displacement measurements. The change in area of the black square can be clearly seen in Figure B.4 measured for a displacement along *x*- axis. Thus, it is important to optimize area interval. Area of black square has been calculated for 50 mm forward and backward motion.

In future, better images with less blurredness can be taken using better lighting and using camera more adaptable to different lightings. Camera that does not create concave effect on the images will be considered. By doing this, less variation in image resolution can be achieved to obtain higher precision. It will make it easier to treat images faster and more precisely.

Bibliography

[ANIM 2005] Animul I.Literature Survey Report on Microfactory.

[AROR 2014] **N. Arora**, T. A. T. Dang, L. Petit, M. Bosch-Mauchand, J. Daaboul, C. Prelle "Contribution to microfactory technologies: a flexible conveyor and its dedicated control system," IWMF 2014, October 5-8, 2014, Honalulu, HI.

[ATAK 2013] Ataka M., and Fujita H., Conference Locatior, IEEE 26th International Conference on Micro Electro Mechanical Systems (MEMS),2013

[BENC 2006] Bencheikh N.? Conception et réalisation d'un conveyeur électromagnégtique planaire miniature, Advanced Mechanics, Thèse 2006, Université de Technologie de Compiègne, France.

[BOEI 2009] Boeij J. D. E., and Lomonova E.,Experimental Verification of Look-Up Table Based Real-Time Commutation of 6-DOF Planar Actuators. Journal of System Design and Dynamics 3(4):563-571,2009.

[BOSC 2014] Bosch-Mauchand M., Prelle C., Daaboul J., Dang T. A. T., and Labato S. B., Conference Locatior, Proceedings of Joint Conference on Mechanical, Design Engineering & Advanced Manufacturing, Toulouse, France,2014

[CAPP 2014] Cappelleri D., Efthymiou D., Goswami A., Vitoroulis N., and Zavlanos M.,Towards Mobile Microrobot Swarms for Additive Micromanufacturing. International Journal of Advanced Robotic Systems:1,2014.

[CHAP 2004] Chapuis Y. A., Fukuta Y., Mita Y., and Fujita H.,Autonomous decentralized systems based on distributed controlled mems actuator for micro conveyance application. J-Stage 56(1):109-115,2004.

[CLEV 2008] Clévy C., Hubert A., and Chaillet N.,Flexible Micro-Assembly System Equiped with an Automated Tool Changer. Journal of Micro-Nano Mechatronics,2008.

[DANG 2016] Dang T. A. T., Bosch-Mauchand M., Arora N., Prelle C., and Daaboul J.,Electromagnetic modular Smart Surface architecture and control in a microfactory context. Computers in Industry 81:152-170,2016.

[DAS 2012] Das A. N., Murthy R., Popa D. O., and Stephanou H. E.,A Multiscale Assembly and Packaging System for Manufacturing of Complex Micro-Nano Devices. IEEE Trransactions on Automation Science and Engineering 9:160-170,2012.

[DELE 2010] Delettre A., Laurent G. J., and Fort-Piat N. L., Conference Locatior, IEEE/RSJ International Conference on Intelligent Robots and Systems, Taipei, Taiwan,2010

[DESC 2004] Descourvières E., Gendreau D., Lutz P., and Kiefer F., Conference Locatior, 4th International Workshop on MicroFactories, IWMF, Shanghai, China,2004

[DITT 2006] Dittrich P., and Radeck D., Conference Locatior, IEEE International Conference on Electro/information Technology, pp. 81-86,2006

[EBEF 2000] Ebefers T., Mattsson J. U., Kalvesten E., and Stemme G.,A robust micro conveyornrealized by arrayed polymide joint actuators. Journal of Micromechanics and Microengineering 10(3):337-349,2000.

[FOUR 2004] Fourment S., Arguel P., Noullet J. L., Lozes F., Bonnefont S., Sarrabayrouse G., Jourlin Y., Jay J., and Parriaux O.,A silicon integrated opto-electro-mechanical displacement sensor. Sensors and Actuators A: Physical 110(1-3):294-300,2004.

[FURL 2001] Furlani E. P. Permanenet Magnet and Electromechanical Devices. Pp. 110-111, 211-216: Academic Press.

[GAUG 2004] Gaugel T., Bengel M., and Malthan D.,Building a mini-assembly system from a technology construction kit. Assembly Automation 24(1):43-48,2004.

[GAUG 2002] Gaugel T., Dobler H., Rohrmoser B., Klenk J., GNeugebauer J., and Schäfer W., Conference Locatior, Proceedings Second International Workshop on Microfactories pp. 35-37,2002

[GOWD 1999] Gowdy J., and Butler Z. J., An integrated interface tool for the architecture for agile assembly. *In* IEEE International Conference on Robotics and Automation. Pp. 3097-3102,1999.

[HIEM 2014A] Hiemstra D. B. The design of moving magnet actuators for large-range flexure based nanopositioning, Mechanical Engineering, University of Michigan.

[HIEM 2014b] Hiemstra D. B., Parmar G., and Awtar S.,Performance Tradeoffs Posed by Moving Magnet Actuators in Flexure-Based Nanopositioning. IEEE/ASME Transactions on Mechatronics 19(1),2014b.

[HOAN 2007] Hoang H. V., and Jeon J. W., Signal Compensation and Extraction of High Resolution Position for Sinusoidal Magnetic Encoders. *In* International Conference on Control, Automation and Systems. Pp. 1368-1373. Seoul, Korea, 2007.

[HOAN 2011] Hoang H. V., and Jeon J. W.,An efficient approach to correct the signals and generate high resolution quadrature pulses for magnetic encoders. IEEE Transactions on Industrial Electronics 58(8),2011.

[HONE 2006a] Honegger A. E., Langstaff G. Q., Phillip A. G., VanRavenswaay T. D., Kapoor S. G., and DeVor R. E.,Development of an automated microfactory: Part 1 - Microfactory architecture and sub-systems development. Transactions of the North American Manufacturing Research Institute of SME. 34:333-340,2006a.

[HONE 2006b] Honegger A. E. P., Langstaff, G. Q., Phillip, A. G., Vanravenswaay, T. D., Kapoor, S. G., Gauthier, G. W., Devor, R. E.,Development of an automated microfactory: Part 2 - Experimentation and analysis. Transactions of the North American Manufacturing Research Institute of SME 2006 - Papers Presented at NAMRC 34. 34:341-348,2006b.

[HOSO 2015] Hosobata T., Yamamoto A., and Higuchi T.,Transparent Synchronous Electrostatic Actuator for Long-Stroke Planar Motion. IEEE/ASME Transactions on Mechatronics 20(4),2015.

[HUYA 2015] Huyan P.Réseau d'actionneurs électromagnétiques numériques : caractérisation d'une application de type convoyage et conception optimisée PhD., Advanced Mechanics, Université de Technologie de Compiègne, France.

[VERE 2005] I.Verettas, Clavel R., and A.Codourey, "Pocket Factory": Concept of miniaturized modular cleanroo. *In* In 1st Topical Meeting of Desktop MEMS and Nanofactories (TMMF2005). Tsukuba, Japan2005.

[JARV 2010] Järvenpää E., Heikkilä R., and Tuokko R., Conference Locatior, The 7th International Workshop on Microfactories, Daejeon, Korea,2010

[KARP 2008] Karpelson M., Wei G. Y., and Wood R. J.,A Review of Actuation and Power Electronics Options for Flapping-Wing Robotic Insects.2008.

[KHAN 2012] Muneeb Ullah khan, Nabil Bencheikh, Chritine prelle, Frédéric Lamarque, Tobias Beutel and Stephanus Büttgenbach, "A long stroke Electromagnetic XY positioning stage for micro applications, IEEE Transaction on Mechatronics, vol. 17, issue: 4, pp.866-897, 2012

[KHAN 2014] Khan M. U. 2014 Contribution to the design and fabrication of an integrated micro-positioning system Thesis, Mechanical Engineering, Université de Technologie de Compiègne, France.

[KHIA 2007] Khiat A. Capteurs à fibres optiques por la mesure à haute résolution de déplacements linéaires et angulaires sur une grande étendue. Application aux sytèmes mécaniques de dimensions réduites. Thesis, Mechanical department Université de Technologie de Compiègne, France.

[KHIA 2010a] Khiat A., Lamarque F., Prelle C., Bencheikh N., and Dupont E.,High-resolution fibre-optic sensor for angular displacement measurements. Measurement Science and Technology 21(2):025306,2010a.

[KHIA 2010b] Khiat A., Lamarque F., Prelle C., Pouille P., Leester-Schädel M., and Büttgenbach S.,Two-dimension fiber optic sensor for high-resolution and long-range linear measurements. Sensors and Actuators A: Physical 158(1):43-50,2010b.

[KUMA 2012] Kumagai M., and Hollis R. L., Conference Locatior, IEEE International Conference on Robotics and Automation, RiverCentre, Saint Paul, Minnesota, USA,2012

[LEI 2010] Lei J., Luo X., Chen X., and Yan T.,Modeling and analysis of a 3-DOF Lorentz-force-driven planar motion stage for nanopositioning. Mechatronics 20(5):553-565,2010.

[LU 2012] Lu X., and Usman I.-u.-r.,6D direct-drive technology for planar motion stages. CIRP Annals - Manufacturing Technology 61(1):359-362,2012.

[LU 1998] Lu Z., and Yoneyama T.,Micro cutting in the micro lathe turning system. International Journal of Machine Tools & Manufacture 39:1171-1183,1998.

[MAEK 2001] Maekawa H., and Komoriya K., Conference Locatior, Proceedings of IEEE International Conference on Robotics 8 Automation Seoul, Korea, pp. 1444-1451,2001

[MISH 2011] Mishima N., and Ashida K., Conference Locatior, Proceedings of the 2011 IEEE International Coference on Mechatronics and Automation, Beijing, China, pp. 773-777,2011

[NGUY 2012] Nguyen V. H., and Kim W.-j.,Novel Electromagnetic Design for a Precision Planar Positioner Moving Over a Superimposed Concentrated-Field Magnet Matrix. IEEE Transactions on Energy Conversion 27(1):52-62,2012.

[NGUY 2013] Nguyen V. H., and Kim W.-j.,Design and Control of a Compact Lightweight Planar Positioner Moving Over a Concentrated-Field Magnet Matrix. IEEE/ASME TRANSACTIONS ON MECHATRONICS 18(3):1090-1099,2013.

[OKAZ 2004] Okazaki Y., Mishima N., and Ashida K.,Microfactory—Concept, History, and Developments. Journal of Manufacturing Science and Engineering 126(4):837,2004.

[PAN 2011] Pan J. F., and Cheung N. C.,An adaptive controller for the novel planar switched reluctance motor. IET Electric Power Applications 5(9):677,2011.

[PARK 2007] Park J. K., Lee N. K., Lee D. W., and Song J. Y., Development of Microfactory Systems for the Next Generation. *In* 3rd International Workshop on Microfactory Technology. Pp. 5-12, 2007.

[PERR 2011] Perret L., Chassagne L., Topçu S., Ruaux P., Cagneau B., and Alayli Y.,Fiber optics sensor for sub-nanometric displacement and wide bandwidth systems. Sensors and Actuators A: Physical 165(2):189-193,2011.

[PHIN 2012] Phinney L. M., Baker M. S., and Serrano J. R. Thermal Microactuators, Microelectromechanical Systems and Devices. D.N.I. (Ed.), ed. Pp. 415-435: InTech, Available from: http://www.intechopen.com/books/microelectromechanical-systems-and-devices/thermalmicroactuators.

[PIRA 2013] Piranda B., Laurent G. J., Bourgeois J., Clévy C., Möbes S., and Fort-Piat N. L.,A new concept of planar self-reconfigurable modular robot for conveying microparts. Mechatronics 23(7):906-915,2013.

[PREL 2006] Prelle C., Lamarque F., and Revel P.,Reflective optical sensor for long-range and high-resolution displacements. Sensors and Actuators A: Physical 127(1):139-146,2006.

[QIN 2006] Qin Y.,Micro-forming and miniature manufacturing systems — development needs and perspectives. Journal of Materials Processing Technology 177(1-3):8-18,2006.

[REYN 2002] Reyne G.,Electromagnetic actuation for MOEMS, examples, advantages and drawbacks of MAGMAS. Journal of Magnetism and Magnetic Materials:242-245,2002.

[RO 2008] Ro S.-K., Jang S.-K., Kim B.-S., and Park J.-K., Conference Locatior, International Conference on Smart Manufacturing Application, KINTEX, Gyeonggi-do, Korea, pp. 186-189,2008

[SETC 2004] Setchi R. M., and Lagos N., Conference Locatior, 2nd IEEE International Conference on Industrial Informatics, 2004. INDIN '04. 2004,2004

[SHAY 2008] Shay B., Hubbard T., and Kujath M.,Linear frictional micro-conveyors. Sensors and Actuators A: Physical 148(1):290-298,2008.

[SHIN 2011] Shin D., and Kim B.,A laser interferometer encoder with two micromachined gratings generating phase-shifted quadrature. Journal of Micromechanics and Microengineering 21(8):085036,2011.

[SILT 2011] Siltala N., Prusi T., Vuola A., Heikkil R., and Tuokko R., Conference Locatior, IEEE International Symposium on Assembly and Manufacturing (ISAM), 2011,2011

[TAN 2005] Tan K. K., and Tang K.-Z.,Adaptive Online Correction and Interpolation of Quadrature Encoder Signals Using Radial Basis Functions. IEEE Transactions on Control Systems Technology 13(3),2005.

[TONG 2013] Tong H., Li Y., Zhang L., and Li B.,Mechanism design and process control of micro EDM for drilling spray holes of diesel injector nozzles. Precision Engineering 37(1):213-221,2013.

[TUOK 2012] Tuokko R., Heikkilä R., Järvenpää E., Nurmi A., Prusi T., Siltala N., and Vuola A., Conference Locatior. Tampere University of Technology, Department of Production Engineering, Tampere,2012

[UUSI 2004] Uusitalo J. J., Viinikainen H., and Heikkilä R.,Mini assembly cell for the assembly of mini-sized planetary gearheads. Assembly Automation 24(1):94-101,2004.

[WANG 2016] Wang C., Xu L.-l., Zhu J., Yuan Z.-w., Yu Y.-j., and Asundi A. K.,A novel integrated fiber-optic interferometer model and its application in micro-displacement measurement. Optics and Lasers in Engineering 86:125-131,2016.

[WATA 2007] Watanabe Y., Gao W., and Kiyono S.,A double pass surface encoder for measurement of planar motion. International Journal of Surface Science and Engineering (IJSURFSE) 1(1),2007.

[XIE 2011] Xie H., and Régnier S.,Development of a Flexible Robotic System for Multiscale Applications of Micro/Nanoscale Manipulation and Assembly. IEEE/ASME TRANSACTIONS ON MECHATRONICS 16:266-276,2011.

[YAHI 2012] Yahiaoui R., Zeggari R., Malapert J., and Manceau J.-F.,A MEMS-based pneumatic micro-conveyor for planar micromanipulation. Mechatronics 22(5):515-521,2012.

[YE 2015] Ye G., Liu H., Fan S., Li X., Yu H., Lei B., Shi Y., Yin L., and Lu B.,Precise and robust position estimation for optical incremental encoders using a linearization technique. Sensors and Actuators A: Physical 232:30-38,2015.

[SHI 2017] Z. Shi, B. Bélier, E. Martincic, L. Petit J. M., E. Lefeuvre, J. Terrien, C. Prelle, and Lamarque F.,Development of a 2D array of micromachined electromagnetic digital actuators for micro- conveyance applications. Microsystem Technologies In press,2017.

[ZEGG 2010] Zeggari R., Yahiaoui R., Malapert J., and Manceau J.-F.,Design and fabrication of a new two-dimensional pneumatic micro-conveyor. Sensors and Actuators A: Physical 164(1-2):125-130,2010.

[ZHAK 2014] Zhakypov Z., Uzunovic T., Nergiz A. O., Baran E. A., Golubovic E., and Sabanovic A., Conference Locatior, IEEE 23rd International Symposium on Industrial Electronics (ISIE), 2014,2014